Sub-femtosecond Precision Timing Distribution, Synchronization and Coherent Synthesis of Ultrafast Lasers

by

Jonathan A. Cox

B.S., Electrical Engineering and Computer Science
Massachusetts Institute of Technology, 2006

M.Eng., Electrical Engineering and Computer Science
Massachusetts Institute of Technology, 2007

SUBMITTED TO THE DEPARTMENT OF ELECTRICAL ENGINEERING AND COMPUTER SCIENCE
IN PARTIAL FULFILLMENT FOR THE DEGREE OF

DOCTOR OF PHILOSOPHY IN ELECTRICAL ENGINEERING AND COMPUTER SCIENCE
AT THE
MASSACHUSETTS INSTITUTE OF TECHNOLOGY

FEBRUARY 2012

Signature of Author: _____
Department of Electrical Engineering and Computer Science
October 1, 2011

Certified by: _____
Franz X. Kärtner
Adjunct Professor of Electrical Engineering
Thesis Supervisor

Accepted by: _____
Leslie A. Kolodziejski
Chairman, Department Committee on Graduate Students

[THIS PAGE INTENTIONALLY LEFT BLANK]

Sub-femtosecond Precision Timing Distribution, Synchronization and Coherent Synthesis of Ultrafast Lasers

by

Jonathan A. Cox

Submitted to the Department of Electrical Engineering and Computer Science
on October 1, 2011 in Partial Fulfillment of the Requirements for the
Degree of Doctor of Philosophy in Electrical Engineering and Computer Science

ABSTRACT

In this thesis, we present a complete set of techniques for sub-femtosecond measurement, control and distribution of ultrafast optical pulse trains, with respect to pulse timing and phase.

First, analytical analysis of the balanced optical cross-correlator (BOC) for attosecond precision pulse timing measurement is presented for both short and long crystal devices. It is found that the sensitivity of the long crystal BOC is independent of pulse duration, to first order. In addition, analytical noise models predict 13 as rms resolution, within a 1 MHz bandwidth, for optical pulses consistent with a practical fiber optic timing link. This analysis aids the widespread adoption of the BOC technique for other wavelengths and implementations.

Secondly, long term timing distribution of a 200 MHz ultrafast optical pulse train over 340 m of single mode optical fiber is demonstrated, using the BOC. In this way, the group delay of the fiber link is directly stabilized with unprecedented precision and long-term stability. In addition, by distributing the entire optical pulse train, all optical and RF harmonics are provided at the remote location for direct synchronization of remote ultrafast lasers and microwave electronics. Over 168 hours of continuous, unaided operation, a drift of 5 fs rms is achieved, with less than 1.5 fs rms drift at timescales up to 10,000 seconds. Additional analysis of factors effecting performance, such as polarization mode dispersion and fiber nonlinearity is studied through experiment and simulations. It is found that nonlinear-origin drifts can be avoided for pulse energies below 40 pJ. A chirped pulse method could be implemented to distribute pulses of higher energy.

Thirdly, the first quantum-resolution timing jitter measurement of ultrafast laser timing jitter for passively mode-locked lasers up to the Nyquist frequency is presented. The total jitter from for a 79.4 MHz stretched pulse erbium fiber laser is found to be 2.6 fs rms [10 kHz, 39.7 MHz]. It is found that the timing jitter power spectral density scales with frequency according to that expected for a white noise source, in agreement with theory. However, unexpected spurious jitter at high frequencies can occur for some mode-locked

states, adding up to 5.5 fs rms jitter. Similar measurements of a 200 MHz erbium fiber soliton laser reveal the decay time of center frequency fluctuations to be 17 ns, with a predicted excess noise of approximately ten. These measurements suggest that timing jitter can be decreased through improved amplifier design.

Finally, the synchronization of a 8 fs fiber supercontinuum at 1200 nm to a 7 fs Ti:Sapphire laser pulse train at 800 nm is achieved for both pulse timing and phase with attosecond precision. This achievement is enabled by the development of a novel scheme for stabilization of the carrier envelope offset of the entire optical bandwidth of an octave spanning supercontinuum, without introducing excess timing jitter. In particular, by implementing an acousto-optic frequency shifting (AOFS) feedback system within a fiber supercontinuum source, carrier envelope phase locking, to the Ti:Sapphire laser, is demonstrated to within 200 mrad rms [100 Hz, 5 MHz]. Previous techniques lack the high-speed, orthogonal control of CEP and pulse timing and broad optical bandwidth for synthesizing few-cycle optical pulses. Furthermore, timing synchronization of 280 as rms is achieved through combined piezoelectric and electro-optic feedback on the fiber supercontinuum, as measured with the BOC.

This work enables the synthesis of a frequency comb spanning 650 to 1400 nm, resulting in a 3.5 fs transform limited pulse duration—assuming ideal spectral phase compression. To date, the spectrum has been successfully compressed to 4.7 fs, as measured with two-dimensional spectral shearing interferometry (2DSI). Moreover, by stabilizing a fiber supercontinuum source to a low-noise Ti:Sapphire laser, the ultra-high stability of the Ti:Sapphire laser is fully transferred to the octave spanning supercontinuum.

Thesis Supervisor: Franz X. Kärtner
Title: Adjunct Professor of Electrical Engineering and Computer Science

[THIS PAGE INTENTIONALLY LEFT BLANK]

Acknowledgements

I wish to acknowledge the years of generous mentorship by Prof. Kärtner. I came to the Optics and Quantum Electronics group as a junior in college at MIT under the supervision of Prof. Kärtner and Dr. David Kielpinski to work on mode-locked laser cooling of trapped Ytterbium ions. Through this experience, I gained a great love and appreciation for ultrafast optics. I came to believe that ultrafast optics is unrivaled for mathematical depth and beauty, experimental challenge and scientific interest. Prof. Kärtner has been an inexhaustible source of ideas, and has urged me to pursue the most challenging endeavors. Most importantly, however, Prof. Kärtner maintains a modesty and accessibility which encourages student learning and involvement.

I also thank my thesis committee, Prof. Erich Ippen and Prof. Leslie Kolodziejski, for their guidance during my doctoral research and thesis writing.

In addition, I wish to thank the years of generous support provided by numerous MIT faculty and staff. Coming to MIT as an undergraduate, staying for my Master of Engineering and then continuing on through my PhD, I always appreciated the support and encouragement provided. From the student financial services to the most senior professors, the MIT community interacts with a level of trust, encouragement and courtesy which is perhaps unknown anywhere else.

In particular, I wish to extend my immense gratitude to Dr. Jungwon Kim. Without his exceptional scholarship and selfless nature, this thesis would not be possible. Dr. Kim laid the foundation for sub-femtosecond timing distribution and synchronization. Furthermore, from my undergraduate years as a UROP student through today, he has dedicated many hours toward my research.

Many do not recognize the impact of the cultural and environmental differences between inland Southern California and the Northeast. For this reason, I also thank Cara Farrell from New Mexico and Jonathan Morse from Nebraska for their years of support, especially in light of the significant stresses at MIT. In fact, MIT has also provided significant support, beginning before I was a freshman, under the Project Interphase program.

Of course, financial support is also essential for success, especially in optics. In addition to numerous undergraduate scholarships, I thank the Lemelson Foundation and the Ford Foundation for their generous support during my PhD.

I also owe my parents, Albert and Suzanne Cox, a debt of gratitude (and perhaps an actual debt) for supporting me through nearly 10 years of studies across the continent. In particular, my mother devoted hours of time toward science fairs, even when the school did not offer a program.

Finally, I wish to thank my late grandfather, Arthur Raff, for inspiring my interest in science and engineering at a very young age. As a geophysicist at the Scripps Institute in La Jolla, California, he introduced me to the world of technical and scientific thought. I will always remember vividly how every time I visited, I would wait eagerly for a new box of scientific treasures uncovered from the depths of his voluminous basement. Many of these treasures were found thousands of feet below the surface of the ocean!

Contents

Table of Figures

1 Introduction

Control of ultrafast laser pulse timing and phase has been recognized as a powerful tool for frequency metrology, spectroscopy, subatomic physics, astrophysics and optical clocks, to name a few applications [1]. In particular, ultrafast lasers have a unique property which endows them with tremendous utility: the frequency comb. While an ultra-stable, continuous-wave laser can radiate a single optical frequency with tremendous precision, referencing an optical frequency to a more accessible microwave standard is extremely challenging, expensive and results in a bulky apparatus. Such optical frequency chains occupied entire buildings, and typically employed successive stages which "step up" the signal from a cesium clock to the desired optical frequency. Only government funded laboratories typically had sufficient resources to build and maintain such systems [2].

Today, an ultrafast laser radiating femtosecond optical pulses at precise intervals can replace an entire frequency chain [3]. This is possible because there is a precise relationship between the pulsing rate, typically 1 ns or longer, and the optical emission of the laser. Such a pulsed laser emits a frequency comb that consists of a set of narrowband optical signals spaced precisely by the repetition rate of the pulses. The frequency shift, or offset, of the entire frequency comb can also be measured and controlled at microwave frequencies. Because the entire frequency comb of the ultrafast laser can be referenced to microwave frequencies determined by the pulsing rate, the ultrafast laser performs the operation of an entire frequency chain. In other words, a relationship between the microwave and optical frequency regimes is established by a powerful optical frequency synthesizer—the ultrafast laser.

Ultrafast lasers do not serve only as a convenient replacement for the frequency chain. Instead, the intrinsically low noise characteristics of such lasers render the ultrafast laser as an ideal means for generating and transmitting low-noise microwave signals. As a frequency chain, an ultrafast laser is bi-directional. Optical frequencies may be referenced to stable microwave sources, while the optical resonator itself may be referenced back to microwave frequencies. In this way, the low-noise properties of optical resonators can be exploited to generate extremely low-noise microwave signals [4].

As a result, there is immense interest in exploiting the low-noise properties of ultrafast optical pulse trains. For instance, synchronization of large facilities at the sub-femtosecond level, such as X-ray free electron lasers (X-FELs), can be accomplished by distributing pulse trains over timing stabilized optical fiber. Moreover, as low-noise signal sources, microwave signal generation and photonic analog-to-digital conversion (ADC) has been pursued to overcome the fundamental limitations of microwave oscillators. Finally, having developed techniques for the measurement and control of ultrafast laser pulse timing and carrier phase noise, we may turn our attention toward the coherent synthesis of independent ultrafast lasers. In this way, still shorter or higher power ultrafast pulse trains can be synthesized from conventional laser sources.

1.1 Scope of Thesis

In this thesis, we present a complete set of techniques for sub-femtosecond measurement, control and distribution of ultrafast optical pulse trains, with respect to pulse timing and phase.

First, analytical analysis of the balanced optical cross-correlator (BOC) for attosecond precision pulse timing measurement is presented for both short and long crystal devices. It is found that the sensitivity of the long crystal BOC is independent of pulse duration, to first order. In addition, analytical noise models predict 13 as rms resolution, within a 1 MHz

bandwidth, for optical pulses consistent with a practical fiber optic timing link. This analysis aids the widespread adoption of the BOC technique for other wavelengths and implementations.

Secondly, long term timing distribution of a 200 MHz ultrafast optical pulse train over 340 m of single mode optical fiber is demonstrated, using the BOC. In this way, the group delay of the fiber link is directly stabilized with unprecedented precision and long-term stability. In addition, by distributing the entire optical pulse train, all optical and RF harmonics are provided at the remote location for direct synchronization of remote ultrafast lasers and microwave electronics. Over 168 hours of continuous, unaided operation, a drift of 5 fs rms is achieved, with less than 1.5 fs rms drift at timescales up to 10,000 seconds. Additional analysis of factors effecting performance, such as polarization mode dispersion and fiber nonlinearity is studied through experiment and simulations. It is found that nonlinear-origin drifts can be avoided for pulse energies below 40 pJ. A chirped pulse method could be implemented to distribute pulses of higher energy.

Thirdly, the first quantum-resolution timing jitter measurement of passively mode-locked, ultrafast laser timing jitter up to the Nyquist frequency is presented. The total jitter from for an 79.4 MHz stretched pulse erbium fiber laser is found to be 2.6 fs rms [10 kHz, 39.7 MHz]. It is found that the timing jitter power spectral density scales with frequency according to that expected for a white noise source, in agreement with theory. However, unexpected spurious jitter at high frequencies can occur for some mode-locked states, adding up to 5.5 fs rms jitter. Similar measurements of a 200 MHz erbium fiber soliton laser reveal the decay time of center frequency fluctuations to be 17 ns, with a predicted excess noise of approximately ten. These measurements suggest that timing jitter can be decreased through improved amplifier design.

Finally, the synchronization of a 8 fs fiber supercontinuum at 1200 nm to a 7 fs Ti:Sapphire laser at 800 nm is achieved for both pulse timing and phase with attosecond precision. This achievement is enabled by the development of a novel scheme for

stabilization of the carrier envelope offset of the entire optical bandwidth of an octave spanning supercontinuum, without introducing excess timing jitter. In particular, by implementing an acousto-optic frequency shifting (AOFS) feedback system within a fiber supercontinuum source, carrier envelope phase locking, to the Ti:Sapphire laser, is demonstrated to within 200 mrad rms [100 Hz, 5 MHz]. Previous techniques lack the high-speed, orthogonal control of CEP and pulse timing and broad optical bandwidth for synthesizing few-cycle optical pulses. Furthermore, timing synchronization of 280 as rms is achieved through combined piezoelectric and electro-optic feedback on the fiber supercontinuum, as measured with the BOC.

This work enables the synthesis of a frequency comb spanning 650 to 1400 nm, resulting in a 3.5 fs transform limited pulse duration—assuming ideal spectral phase compression. To date, the spectrum has been successfully compressed to 4.7 fs, as measured with two-dimensional spectral shearing interferometry (2DSI). Moreover, by stabilizing a fiber supercontinuum source to a low-noise Ti:Sapphire laser, the ultra-high stability of the Ti:Sapphire laser is fully transferred to the octave spanning supercontinuum.

1.2 Low-noise Microwave Signal Generation and Sampling

Ultrafast lasers are enabling higher speed, higher resolution analog-to-digital conversion (ADC) with photonic ADCs. By replacing the microwave sampling clock in an electrical ADC with an optical oscillator pulsing at gigahertz rates, the aperture timing jitter can be reduced. Such a reduction in timing jitter eliminates a key bottleneck preventing high-resolution ADC at frequencies beyond 10 GHz [5–7]. The scaling of ADC resolution, expressed in effective number of bits (ENOB) versus sampling clock timing jitter is described by FIG. 1. Existing technology based on microwave sampling clocks cannot progress much beyond the picosecond timing jitter regime. However, the low jitter property of ultrafast lasers can be directly exploited by sampling a microwave signal in the optical domain with

an ultrafast pulse train. For instance, the amplitude of an optical pulse train can be directly modulated by an applied microwave signal with a Mach-Zehnder interferometer, as in FIG. 2.

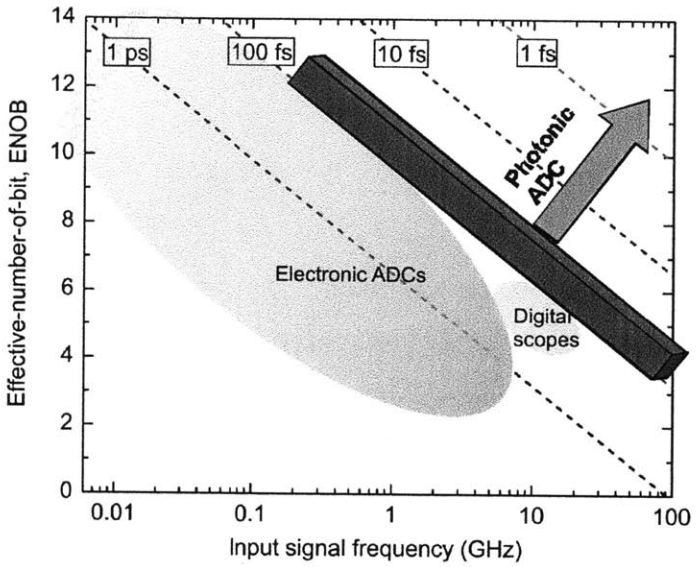

FIG. 1. Scaling of the resolution of an analog-to-digital converter (ADC) with the timing jitter of the sampling clock. The effective number of bits (ENOB) can be limited by the so-called aperture jitter of the sampling clock. For high resolution beyond 10 GHz, photonic ADCs are necessary [6], [7].

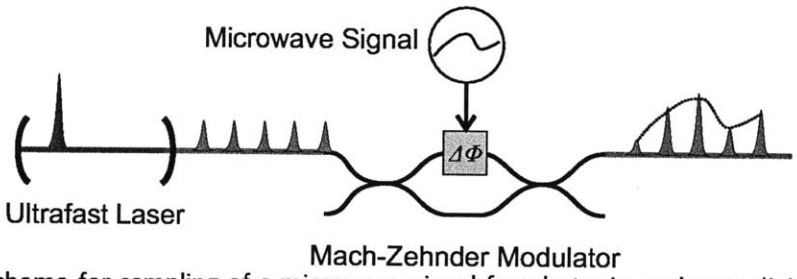

FIG. 2. Basic scheme for sampling of a microwave signal for photonic analog-to-digital conversion. Sampling is performed in the optical domain at precise intervals gated by ultrafast pulses passing through a phase shifter within a Mach-Zehnder modulator. The Mach-Zehnder encodes the amplitude of the microwave signal in the pulse train. The pulse train can later be demultiplexed (not shown) for sampling with low-speed electronic ADCs.

However, the low-noise properties of ultrafast lasers have not been well characterized. With such low noise, there exists no better reference to compare the ultrafast laser to. Instead, new techniques for measuring timing jitter with attosecond precision have been necessary. Careful measurement of the complete timing jitter spectrum is needed to advance the theoretical understanding of these lasers, which are complex, non-linear systems, for which no accurate analytical model often exists [8]. Having developed a method for measuring the complete timing jitter spectrum of ultrafast lasers, their performance can be engineered and improved for integrated photonic ADCs and microwave signal generation.

To advance understanding of ultrafast laser timing jitter, first quantum-resolution timing jitter measurement of an ultrafast laser pulse train up to the Nyquist frequency is presented. The total jitter from for a 79.4 MHz stretched pulse erbium fiber laser is found to be 2.6 fs rms [10 kHz, 39.7 MHz]. It is found that the timing jitter power spectral density scales with frequency according to that expected for a white noise source, in agreement with theory. However, unexpected spurious jitter at high frequencies can occur for some mode-locked states, adding up to 5.5 fs rms jitter. Similar measurements of a 200 MHz erbium fiber soliton laser reveal the decay time of center frequency fluctuations to be 17 ns, with a predicted excess noise of approximately ten. These measurements suggest that timing jitter can be decreased through improved amplifier design.

1.3 Timing Synchronization for X-Ray Free Electron Lasers

With such versatility and low-noise, ultrafast pulse trains can also be used to synchronize the timing of microwave and optical devices separated by hundreds of meters. For instance, X-ray free electron lasers (X-FEL) radiating femtosecond X-ray pulses require femtosecond synchronization of many lasers and microwave devices across distances up to 3000 m. Femtosecond optical pulse trains can be distributed over timing stabilized optical fiber links

to each point in the X-FEL to provide femtosecond precision synchronization [9]. This scheme, as described by FIG. 3, is especially convenient because the femtosecond pulses radiating from the end of the stabilized fiber links may be directly used for microwave signal generation or for synchronizing remote femtosecond lasers. In contrast, interferometric or single-frequency stabilization stabilizes only the phase delay, not the group delay of the fiber, and does not provide the entire frequency comb at the link output. Since information is transmitted at the group velocity, interferometric stabilization of the phase velocity does not guarantee femtosecond precision transfer of microwave frequency timing information.

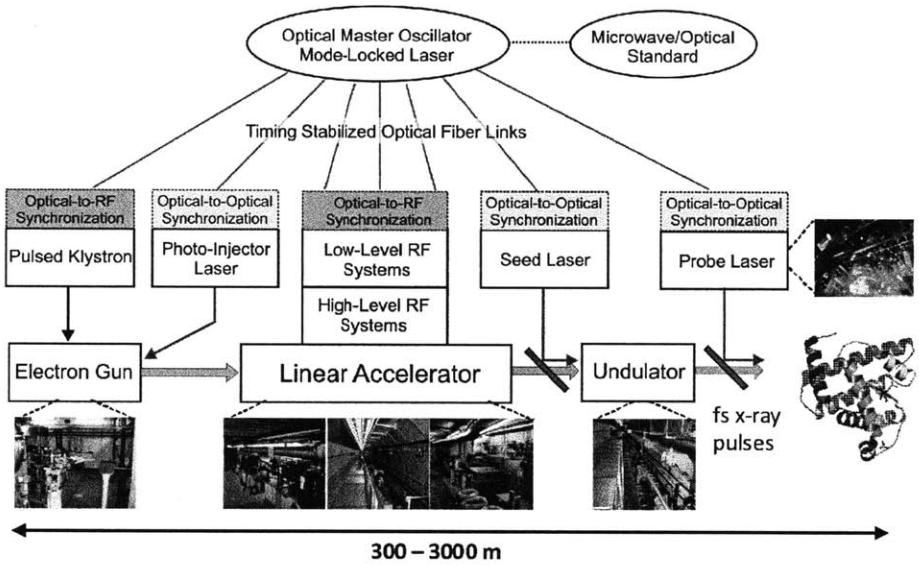

FIG. 3. Diagram of prototypical X-ray free electron laser and timing synchronization system. The optical master oscillator (an ultrafast laser) is tightly synchronized to the microwave standard to provide precise, long-term timing for the facility. The low timing jitter optical pulse trains are distributed over timing stabilized fiber links to synchronize laser and microwave devices over 300 to 3000 m. At the end of the X-FEL, scientific users will conduct timing sensitive pump-probe experiments with radiated X-ray pulses. *J. Kim, FEL 2004* [10].

Moreover, timing distribution with ultrafast optical pulse trains can achieve femtosecond precision, in contrast to existing microwave techniques, because the femtosecond pulse naturally enables sub-femtosecond resolution timing measurement. In

contrast, a 10 GHz microwave carrier with a 100 ps period is limited to the picoseconds regime [9], [10].

Active timing stabilization of the optical fiber is necessary for synchronizing remote points in space to better than picosecond precision because of the influence of acoustic noise, thermal variations and mechanical stress on the fiber links. The basic scheme of ultrafast timing distribution is shown in FIG. 4. The major source of slow timing drift in the optical fiber is thermal variation of the index of refraction at the 10^{-5} K^{-1} level [11].

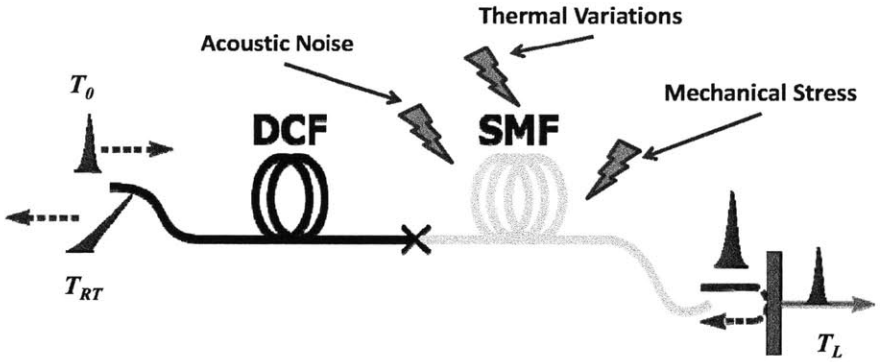

FIG. 4. A basic description of timing stabilized fiber links based on ultrafast pulse trains. A pulse entering the link at time T_0 travels through the single mode fiber (SMF) and dispersion compensating fiber (DCF), and is partially transmitted through an end mirror at time T_L. Due to the action of acoustic noise, thermal variations and mechanical stress, the time of flight of the pulse T_L, is unknown to better than 100 ps precision, for a kilometer length link. By measuring the round trip time T_{RT} relative to T_0, the time of flight, T_L, can be stabilized ($2 \cdot T_L \approx T_{RT}$.)

In this thesis, we present detailed experimental, analytical and numerical studies of ultrafast pulse timing distribution and transfer over optical fiber. Attosecond resolution timing measurement is at the heart of the system, which is accomplished with the balanced optical cross-correlator. This work aims toward both sub-femtosecond synchronization at short time scales, as well as femtosecond precision drift at time scales reaching an entire week.

First, analytical analysis of the balanced optical cross-correlator (BOC) for attosecond precision pulse timing measurement is presented for both short and long crystal devices. It is found that the sensitivity of the long crystal BOC is independent of pulse duration, to first order. In addition, analytical noise models predict 13 as rms resolution, within a 1 MHz bandwidth, for optical pulses consistent with a practical fiber optic timing link. This analysis aids the widespread adoption of the BOC technique for other wavelengths and implementations.

Secondly, long term timing distribution of a 200 MHz ultrafast optical pulse train over 340 m of single mode optical fiber is demonstrated, using the BOC. In this way, the group delay of the fiber link is directly stabilized with unprecedented precision and long-term stability. In addition, by distributing the entire optical pulse train, all optical and RF harmonics are provided at the remote location for direct synchronization of remote ultrafast lasers and microwave electronics. Over 168 hours of continuous, unaided operation, a drift of 5 fs rms is achieved, with less than 1.5 fs rms drift at timescales up to 10,000 seconds. Additional analysis of factors effecting performance, such as polarization mode dispersion and fiber nonlinearity is studied through experiment and simulations. It is found that nonlinear-origin drifts can be avoided for pulse energies below 40 pJ. A chirped pulse method could be implemented to distribute pulses of higher energy.

1.4 Coherent Pulse Combining and Single-Cycle Synthesis

The single-cycle pulse has been actively pursued in the quest for ever faster ultrafast lasers [12], [13]. With a single-cycle source, the universe of phase sensitive non-linear optics can be explored [14]. For example, the study of quantum tunneling effects or coherent Rabbi flopping in quantum wells can be probed [15], [16]. Additionally, intense, single-cycle sources can enhance the generation of individual attosecond X-ray pulses through high harmonic generation [17].

Single-cycle pulses are so fast, that the pulse envelope contains only a single period of an electromagnetic wave at optically frequencies—about 3.3 fs at 1000 nm. Since there is no known near-infrared ultrafast laser with sufficient gain bandwidth to emit such a short pulse, novel approaches toward generating single cycle pulses must be considered. One especially promising technique is non-linear spectral broadening. By broadening the spectrum from a single laser, temporally compressing the broadband output and then recombining, a single cycle pulse may be synthesized [12], [18].

However, non-linear spectral broadening can impose limitations on the pulse energy and repetition rate. Furthermore it has been challenging to synthesize a continuous spectrum from non-linear techniques without a large spectral gap in between short-and long-wavelength components [12], [19].

Therefore, a method for coherent beam combining of independent <10 fs lasers is developed to progress toward the single-cycle regime. Synchronization of independent <10 fs lasers, however, is made extremely challenging by the requirement that sub-cycle (attosecond) precision sychronization be achieved in both pulse timing and carrier envelope phase (CEP). This two degree of freedom requirement, on both pulse phase and timing, is described by FIG. 5 in the time domain. The carrier envelope phase, as well as the timing offset of the carrier envelope, must be simultaneous locked to zero offset between pulses with sub-cycle precision.

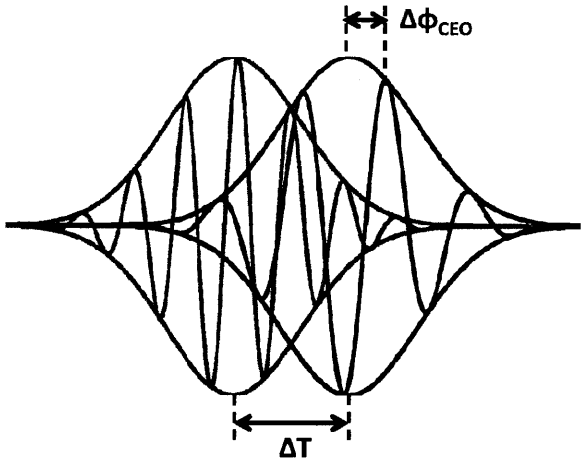

FIG. 5. The principle underlying coherent beam combining of ultrafast laser pulses. By controlling the carrier envelope phase and pulse envelope timing with attosecond precision, the pulses (with different center wavelengths) can be constructively interfered to synthesize a pulse shorter than either pulse alone.

Existing methods for femtosecond laser beam combining and CEP control have lacked the required control loop bandwidth, orthogonal control between phase and timing, or optical bandwidth to be successful for synthesizing few-cycle pulses from independent lasers [3], [5], [20–24]. For instance, the most common method for CEP control, pump power modulation, induces a timing shift of 0.1 fs/nJ per roundtrip [25]. Since the piezo actuator used for timing stabilization can only respond at a 10 kHz rate, there are easily 4000 roundtrips before the timing loop can begin to respond. For a 1% pulse energy change in a 100 mW, 80 MHz Ti:Sapphire laser, we expect a timing shift of 5 fs. In practice, the piezo loop has only sufficient loop gain to significantly suppress timing fluctuations below 1 kHz, which would lead to a timing shift of up to 50 fs due to a 1% pulse energy change. Therefore, pump power modulation is not a suitable choice for simultaneous stabilization of CEP and pulse timing with sub-cycle precision. Mechanical methods for stabilizing CEP are impractical for sub-cycle CEP control due to the extremely limited bandwidth of such techniques, usually below 1 kHz [23].

An additional concern for the synchronization of a fiber supercontinuum to a Ti:Sapphire laser with sub-cycle precision is the greater noise of fiber sources, as compared to Ti:Sapphire lasers. To achieve sub-cycle CEP locking to the Ti:Sapphire the loop bandwidth of the fiber CEP stabilization must be much greater. Due to the upper state lifetime of Ti:Sapphire and the mode-locking dynamics, pump-power modulation of Ti:Sapphire CEP is limited to 70—80 kHz [26], [27]. For erbium fiber lasers with millisecond upper state lifetime, CEP stabilization bandwidth is even more limited [28]. Moreover, the large beam diameter of the Ti:Sapphire pump beam makes stabilization beyond 80 kHz with an acousto-optic modulator impractical. In effect, the stabilization bandwidth is limited by the delay of the AOM, which is caused by the propagation delay of the acoustic wave across the pump beam. In any event, it is desirable to stabilize the fiber laser CEP to the Ti:Sapphire CEP since the Ti:Sapphire serves as a low-noise, free-running reference for which to lock the noisier fiber laser to.

In the spirit of scientific pursuit, solutions to the challenges facing ultrafast pulse combining have provided answers for other problems. For instance, the push toward gigahertz repetition rate fiber or integrated frequency combs requires a method for stabilizing the carrier envelope phase of a very broad optical bandwidth. Mechanical actuators for adjusting the carrier envelope phase are not feasible for compact sources [23]. Also, optical CEP techniques based on laser pump power modulation can fail to provide significant phase shifting in compact fiber sources. Fortunately, a non-mechanical, potentially integrable, high-speed method for carrier envelope phase shifting is demonstrated. An acouto-optic frequency shifter (AOFS) in feedback configuration placed outside the laser cavity can correct for fluctuations of the carrier phase without disturbing the laser oscillator, as shown in FIG. 6. As the AOFS is placed outside the oscillator, but before amplification and supercontinuum generation, octave spanning, CEP stable supercontinuum with diffraction limited output can be realized. Previous work has relied on a drift prone, feed-forward loop for CEP stabilization that also stabilized only a narrow slice of supercontinuum which is diffracted by the AOFS.

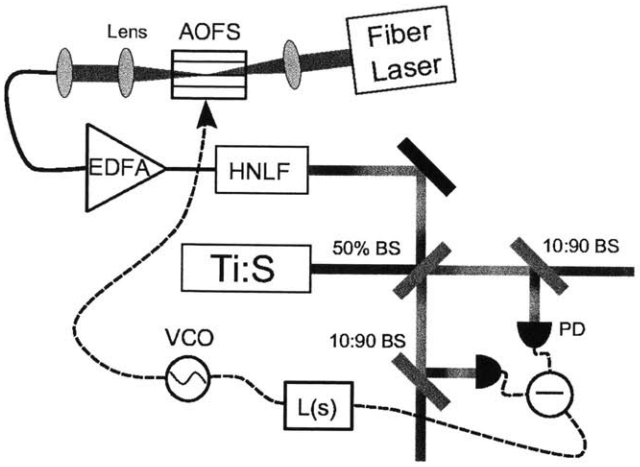

FIG. 6. Method for stabilization of carrier envelope phase of a fiber laser supercontinuum to a Ti:Sapphire reference laser with octave spanning, diffraction limited output. Shifting of the CEP is provided by the feedback signal to an acouto-optic frequency shifter (AOFS). Since shifting is performed before amplifier and supercontinuum generation, optical bandwidth and beam quality are not sacrificed. Out of loop drifts are additionally eliminated by the feedback architecture.

In a similar way, attosecond synchronization of independent lasers can inform ultrafast timing distribution. For next generation X-FELs, attosecond long-term timing synchronization is needed. This will require an exceptionally low-noise, reliable, self-starting waveguide-based ultrafast laser for long-term timing distribution. Since it is difficult to engineer sub-femtosecond noise in a robust waveguide laser, the optical master oscillator can be tightly synchronized to the X-FEL's microwave standard, with techniques borrowed from coherent pulse combining. First, course timing synchronization at the femtosecond level is achieved through cavity length modulation with a piezoelectric actuator. Then, a high-speed electro-optic phase shifter placed outside the laser cavity can virtually eliminate remaining timing fluctuations. This two-stage scheme was developed for timing synchronization of the fiber supercontinuum to the Ti:Sapphire laser for coherent pulse combining.

Prior work on the successful synchronization of independent lasers has been performed for slightly detuned Ti:Sapphire lasers with 30 fs pulses, and without long-term stability beyond a few seconds [23]. For long-term stable, few-cycle pulse generation, attosecond precision synchronization with good long-term stability is required for use in applications.

In this thesis, the synchronization of a 8 fs fiber supercontinuum at 1200 nm to a 7 fs Ti:Sapphire laser at 800 nm is achieved for both pulse timing and phase with attosecond precision. This achievement is enabled by the development of a novel scheme for stabilization of the carrier envelope offset of the entire optical bandwidth of an octave spanning supercontinuum, without introducing excess timing jitter. In particular, by implementing an acousto-optic frequency shifting (AOFS) feedback system within a fiber supercontinuum source, carrier envelope phase locking, to the Ti:Sapphire laser, is demonstrated to within 200 mrad rms [100 Hz, 5 MHz]. Previous techniques lack the high-speed, orthogonal control of CEP and pulse timing and broad optical bandwidth for synthesizing few-cycle optical pulses. Furthermore, timing synchronization of 280 as rms is achieved through combined piezoelectric and electro-optic feedback on the fiber supercontinuum, as measured with the balanced optical cross-correlator (BOC).

This work enables the synthesis of a frequency comb spanning 650 to 1400 nm, resulting in a 3.5 fs transform limited pulse duration—assuming ideal spectral phase compression. To date, the spectrum has been successfully compressed to 4.7 fs, as measured with two-dimensional spectral shearing interferometry (2DSI). Moreover, by stabilizing a fiber supercontinuum source to a low-noise Ti:Sapphire laser, the ultra-high stability of the Ti:Sapphire laser is fully transferred to the octave spanning supercontinuum.

2 Balanced, Optical, Cross-correlation for Attosecond Precision Timing Jitter Measurement

Attosecond precision timing measurement between ultrafast optical pulse envelopes has emerged as a critical need for sub-femtosecond control and measurement of ultrafast pulse timing. Balanced optical cross-correlation (BOC) provides a means of achieving attosecond resolution measurement of relative timing between ultrafast pulses by directly measuring the offset between pulse envelopes. With this technique, amplitude and temperature invariant control of pulse timing can be achieved for femtosecond synchronization of X-ray free electron lasers (X-FELs) through timing stabilized optical fiber links. Additionally, with such precision, one can explore the coherent synchronization of independent ultrafast lasers for few-cycle pulse generation [9], [13].

With the ability to measure laser timing jitter with attosecond precision, progress toward engineering lower jitter lasers can be accelerated. Prior techniques have demonstrated insufficient timing resolution to fully characterize the jitter of ultrafast lasers [29]. Interferometric techniques fail to distinguish between carrier phase fluctuations and pulse envelope timing fluctuations.

To this end, a compact, analytical model for the design and performance of both "thin" and "long" crystal BOCs is developed. The model is designed to be applicable to both existing, bulk cross-correlator technology, as well as for integrated BOCs that are being

actively pursued [30]. In this way, these models may serve as a means for understanding the principles of BOC, as well as the limitations and tradeoffs.

2.1 Methods for Characterizing Timing Jitter

Sub-femtosecond precision timing distribution and coherent synthesis of ultrafast lasers require attosecond resolution, temperature and amplitude noise invariant timing jitter detection of ultrafast optical pulse trains. The ideal timing detection technique would be insensitive to amplitude fluctuations in the optical pulse train, achieve attosecond resolution and directly measure the timing of the pulse envelope—not the optical carrier phase.

Several methods have been developed for laser synchronization and jitter measurement, spanning both electronic and optical domains. One of the most widely used methods is direct photodetection using electronic mixers [31]. With this technique, the optical signal is detected on a slow photodetector through modal beating, producing a comb of harmonics at multiples of the repetition rate. Since the phase of the electrical signal is related to the pulse timing, the timing jitter can be extracted by mixing a single electrical harmonic with a reference signal using a standard microwave mixer. Although relatively inexpensive and straightforward, this basic technique fails to deliver the sub-femtosecond resolution required [32], [33]. Moreover, the cables and mixer are exceptionally sensitive to thermal variations, experiencing many tens of femtoseconds of drift, even when temperature stabilized.

Beyond direct photodetection, there are a host of optical phase detection techniques. For instance, one can interfere two pulses to extract a timing measurement, knowing the wavelength of the carrier wave [34]. However, this technique does not directly measure the pulse envelope timing, but rather the phase of the carrier wave. As such, it is tenuous to draw conclusions regarding the timing jitter using an interferometric method [9],

[29], [32], [35], [36]. The interferometric method also has the disadvantage that the capture range is extremely small, as it is only half an optical cycle. At a center wavelength of 1000 nm in vacuum, half a cycle is only 1.7 fs. Most fibers lasers have significantly greater jitter beyond the synchronization bandwidth than the full capture range of this method [29].

Beyond interferometry, which measures optical phase, optical frequencies can be used to transfer the stability of one frequency comb to another [37]. In fact, by phase locking only a pair of optical harmonics of the frequency comb of one laser to that of another, the entire comb of one ultrafast laser can be fully transferred—including both repetition rate and carrier envelope phase. Alternatively, one can phase lock one laser's frequency comb line to a remote laser, and then lock the f_{CEO} to zero using the self-referencing technique. This allows one to transfer all the information of the frequency comb from one laser to another with only a single optical frequency, since it is assumed the carrier envelope phase (CEP) slip is zero for both lasers. In fact, this technique can have exceptional sensitivity since the optical phase locking is done directly at optical frequencies. However, as with interferometric techniques, the locking range is limited to within an optical cycle. Moreover, extraction of the timing jitter from the optical phase is, again, tenuous, unless we assume that the CEP does not vary. Even the best CEP stabilization schemes still result in non-negligible optical phase noise. Furthermore, stabilization of the CEP is non-trivial and adds significant complexity.

However, we concentrate our study of timing jitter measurement on pulse envelope optical cross-correlation, since this technique provides a direct measurement of envelope timing. By generating an optical signal which is proportional to the temporal overlap of two optical pulses, we may directly observe the pulse timing in the optical domain, with great sensitivity. Because the cross-correlation is performed between femtosecond pulses, the technique provides sub-femtosecond precision with a capture range much greater than for interferometric or optical frequency techniques.

2.1.1 Direct Photodetection of Optical Pulse Trains

One of the most versatile and straight forward methods for timing jitter measurement of ultrafast, optical, pulse-trains is direct photodetection with microwave electronics. The technique involves detection of the optical pulse train on semiconductor photodetector with a typical electrical bandwidth of several gigahertz. For the greatest sensitivity, the bandwidth of the photodetector should exceed the pulse repetition rate by several times. After conversion from the optical to electronic domain, a single harmonic of the electrical pulse train is extracted via a narrow microwave cavity filter, and amplified. Since the phase and frequency of the chosen harmonic is related to the optical pulse repletion rate, the harmonic can be compared to other microwave signal sources with a phase detector, or mixer. In this way, the optical pulse timing of one laser can be synchronized to another laser or to an electronic signal source. The basic scheme is captured by FIG. 7, whereby the signal from the ultrafast laser is compared to a stable reference oscillator (which can be a microwave oscillator or another laser).

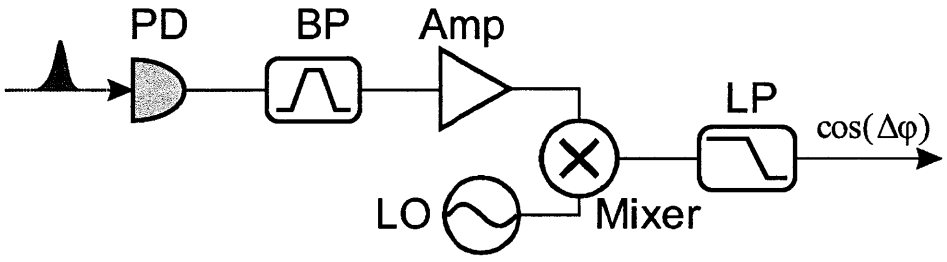

FIG. 7. Block diagram of direct photodetection microwave electronics for ultrafast timing measurement. The bandpass filter (BP) should select a single RF harmonic—the greater the harmonic number, the better the sensitivity. In the above: photodetector (PD), lowpass filter (LP), local oscillator (LO), amplifier (Amp).

To understand how the phase of a single harmonic of the photodetected, electrical pulse train is related to the pulse timing of the laser, consider the idealized process [31]. In

particular, one can model the pulse train as a train of impulses since the pulse envelope is typically 100 fs or less.

Typical semiconductor photodetectors have bandwidths of 50 GHz or less, with rise times on the order of many picoseconds. For this reason, the detector cannot resolve the pulse envelope. Instead, the photodetector can be characterized by its impulse response. However, for simplicity, we consider only an ideal photodetector with very large bandwidth. As a result, the photodetector current consists of an impulse train perturbed by amplitude and timing noise, as in (2.1) [31]. Here, P is the average pulse, T_R is the pulse repetition rate, N(t) is the normalized amplitude fluctuations and J(t) are the pulse timing fluctuations.

$$I(t) = PT_R\left[1+N(t)\right]\sum_{n=-\infty}^{\infty}\delta\left(t-nT_R-J(t)\right) \tag{2.1}$$

However, we may use the relation given by (2.2) to transform (2.1) into a more easily manipulated form, where $n\omega_L = 2\pi n/T_R$. Thus, ω_L is the pulse repetition frequency in radians per second.

$$\sum_{n=-\infty}^{\infty}\delta\left(t-nT_R-J(t)\right) = \frac{1}{T_R}\sum_{n=-\infty}^{\infty}\exp\left(jn\omega_L\left(t-J(t)\right)\right) \tag{2.2}$$

This relation can be derived by considering that an impulse train in time is the convolution of a single impulse in frequency, (2.4), with an impulse train (series of frequency shifted impulses, (2.3)) in frequency, (2.5). Transforming back to the time domain, the convolution of an impulse with a series of frequency shifted impulses is becomes simply a series of complex exponentials [38].

$$e^{j\omega_0 t} \overset{FT}{\leftrightarrow} 2\pi\delta\left(\omega-\omega_0\right) \tag{2.3}$$

$$1 \overset{FT}{\leftrightarrow} 2\pi\delta\left(\omega\right) \tag{2.4}$$

$$\sum_{n=-\infty}^{\infty}\delta\left(t-nT_R\right) \overset{FT}{\leftrightarrow} \frac{2\pi}{T_R}\sum_{n=-\infty}^{\infty}\delta\left(\omega-\frac{2\pi n}{T_R}\right) \tag{2.5}$$

Therefore, (2.1) can be transformed into (2.6).

$$\underline{I}(t) = P\left[1+N(t)\right]\sum_{n=-\infty}^{\infty}\exp\left(jn\omega_L\left(t-J(t)\right)\right) \tag{2.6}$$

However, the bandpass filter in FIG. 7 selects only a single harmonic in the frequency domain from (2.6), which reduces the photodetector current to (2.7).

$$\underline{I}(t) = P\left[1+N(t)\right]\exp\left(jn\omega_L\left(t-J(t)\right)\right) \tag{2.7}$$

Taking the real part of the photodetector current and converting to a voltage signal via the transimpedance gain in Ohms, G, of the photoreceiver, one arrives at (2.8).

$$V(t) = PG\left[1+N(t)\right]\cos\left(n\omega_L\left(t-J(t)\right)\right) \tag{2.8}$$

To perform phase detection, one mixes the photodetector signal with a local oscillator at $n\omega_L$, to eliminate the high frequency carrier. An ideal mixer performs a multiplication operation between two analog signals, exploiting the trigonometric identity (2.9).

$$2\cos(x)\cos(y) = \cos(x-y)+\cos(x+y) \tag{2.9}$$

After mixing and filtering out the sum frequency term in (2.9) with the low pass filter, we arrive at the detected signal, (2.10).

$$V_o(t) = \frac{PG}{2}\left[1+N(t)\right]\cos\left(n\omega_L J(t)\right) \tag{2.10}$$

From (2.10), we may immediately arrive at several conclusions. First, we detect not the jitter directly, but rather $\cos\left(n\omega_L J(t)\right)$. Of course, adding an arbitrary phase offset of $\pi/2$ to (2.10) and taking the small angle approximate of sine, the detected signal near zero reduces to (2.11).

$$V_o(t) \approx J(t)n\omega_L\frac{PG}{2}\left[1+N(t)\right] \tag{2.11}$$

Therefore, the slope, or sensitivity, of this detection scheme depends on the harmonic number, n, selected—with higher harmonic numbers yielding great sensitivity. Since ω_L is merely the pulse repetition rate, and not an optical frequency, even large values of n still

provide limited sensitivity. Typical fiber-coupled photodetectors can detect harmonics up to 10 GHz, or about 100 ps period. Considering that we wish to detect timing fluctuations on the order of 100 as, this represents a fractional signal of 10^{-6}—a difficult task.

Moreover, it is also difficult to discriminate between amplitude noise in N(t) and timing jitter, since both give rise to fluctuations in the output signal. Of course, we also assumed that the phase detection was performed by mixing with a noiseless local oscillator. In practice, the ultrafast laser likely has much lower noise density at higher frequencies than a microwave LO. As a result, fast timing jitter fluctuations in J(t) are often completely overwhelmed by fluctuations in the local oscillator signal [35], [39].

Despite the availability of more complex schemes to improve direct photodetection, such as balanced quadrature detection, microwave electronics suffers from poor long-term stability at the femtosecond level, as well as excess noise in the photodetection process [9], [36], [40–42]. The poor long-term stability is predominately a result of the temperature sensitivity of the microwave transmission lines, such as coaxial cable, and of the phase detector. Shifts in the impulse response of the photodetector with temperature and signal amplitude also contribute [33]. In addition, at the femtosecond level, phase shifts in the transistors of the microwave amplifiers add excess noise [33].

Ignoring the excess noise inherent in photodetection, consider only the phase stability of the microwave electronics, as in FIG. 8, which are temperature stabilized to ±0.2 K. This test apparatus includes standard commercial devices and microwave cavity filters for the local oscillator frequency of 1.3 GHz. The mixer itself was further stabilized to ±0.02 K with a thermoelectric cooler (TEC). With the TEC, it was determined that the mixer, a MiniCircuits ZX05-C24MH, has a temperature coefficient of 30 fs/K. Despite great effort to maintain precise temperature stabilization of the electronics and mixer with a custom machined, aluminum mounting board and the shortest possible coaxial cables (1-3 inches), significant drift occurs.

A measurement of the timing drift over 24 hours, as shown in FIG. 9, demonstrates 230 fs rms daily drift. A similar measurement performed without amplifiers or filters demonstrated 19 fs rms drift over the same period. As a result, it is believed that the amplifiers, and the significant heat they radiate, the filters and the additional cabling compound the stability problem.

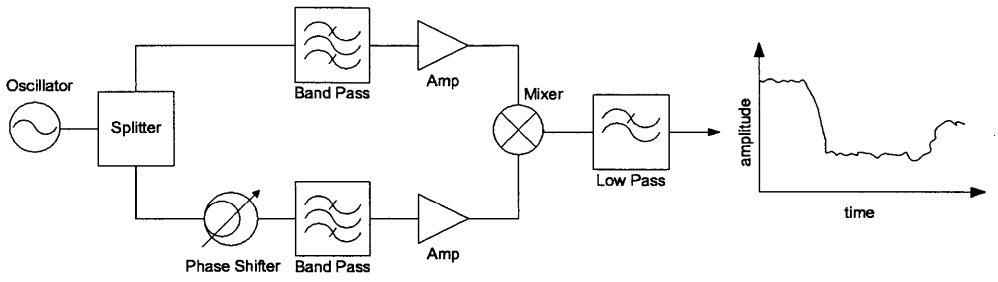

FIG. 8. Schematic of microwave direct conversion electronics phase stability test apparatus. The apparatus is mounted on an aluminum board which is temperature stabilized to ±0.2 K.

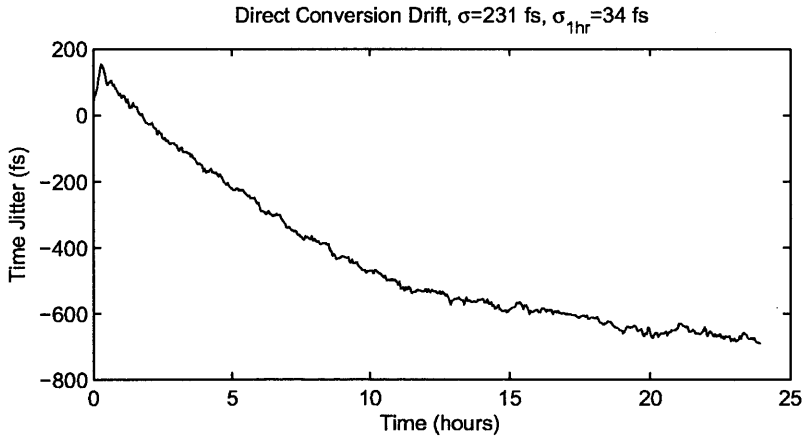

FIG. 9. Drift of a microwave mixer, phase shifter, cavity filters, amplifiers and short coaxial cables which are temperature stabilized to ±0.2 K. The oscillator frequency is 1.3 GHz, from which a timing drift of 231 fs rms over 24 hours is extracted.

2.1.2 Optical Frequency Synchronization

In analogy with direct photodetection and microwave mixing, it is possible to employ optical frequency mixing for phase detection. However, since the optical spectrum of a frequency comb has two degrees of freedom, pulse repletion rate f_R and carrier envelope offset frequency f_{CEO}, both parameters must be considered. However, done properly, this technique provides for extremely sensitive transfer of both pulse timing and carrier envelope phase from one laser to another.

To understand how a frequency comb consisting of thousands or millions of optical harmonics can be transferred in entirety to another by comparing only one or two frequencies, consider a pulse train. An ideal ultrafast pulse train is simply defined as an impulse train at an optical carrier frequency Ω, given by (2.12). The carrier envelope phase is the argument of the complex exponential, Ωt, in radians.

$$E(t) = E_p e^{j\Omega t} \sum_{n=-\infty}^{\infty} \delta(t - nT_R) \tag{2.12}$$

In the frequency domain, (2.12) can be written as (2.13), where $\omega_0 = \mathrm{mod}(\Omega, f_R)$ since the frequency comb is periodic with the comb spacing, $f_R = 1/T_R$.

$$E(\omega) = 2\pi E_p f_R \sum_{n=-\infty}^{\infty} \delta(\omega - \omega_0 - 2\pi n f_R) \tag{2.13}$$

Therefore, we find that a change in repetition rate leads to a change in the comb spacing. On the other hand, a change in carrier envelope frequency leads to a shift of the entire frequency comb by ω_0.

From the expression for the optical frequency comb (2.13), it can be seen that there are only two degrees of freedom, f_R and ω_0. By phase locking both degrees of freedom of one laser to a reference oscillator, both the pulse timing and carrier envelope phase are transferred. Alternatively, one may transfer only one frequency line and lock ω_0 to zero with the self-referencing technique [37]. In the frequency domain, this scheme is described by FIG. 10.

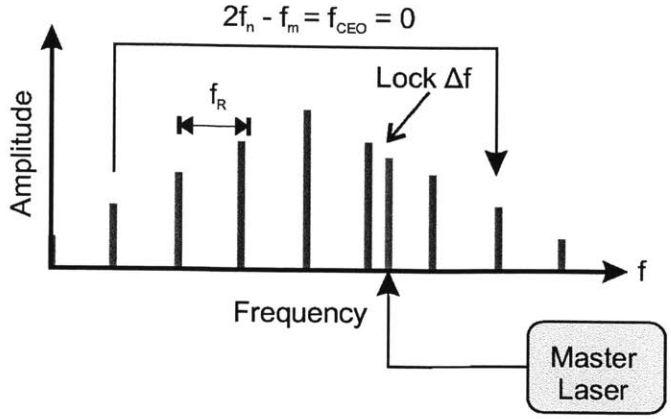

FIG. 10. The frequency comb of one laser can be transferred to another, assuming both lasers have zero carrier envelope phase slip ($f_{CEO} = 0$.) Thus, the pulse timing is transferred by locking one optical harmonic from the master laser to the remote laser frequency comb, shown in blue. When both f_{CEO} and Δf are zero, the frequency combs are identical. Note, however, that this method requires f_{CEO} be exactly zero. Any phase or frequency fluctuations in f_{CEO} give rise to phase or frequency errors in Δf that manifest as measured timing errors.

However, the single frequency transfer method is not without limitations. For instance, self-referencing of the CEP also requires an octave of optical bandwidth, which is difficult to achieve in compact, robust, cost-effective systems. Moreover, since perfect CEP locking is not possible, there is always residual CEP noise that corrupts any timing synchronization, because it is not known if the phase error in the frequency comb arises from fluctuations in f_R or ω_0, which we only assume to be fixed. Instead, we desire a true pulse timing measurement.

2.1.3 Non-linear, Optical Cross-Correlation

A technique which naturally lends itself to timing jitter measurement of the pulse envelope is sum-frequency generation in a non-linear crystal, as described by FIG. 11 [40], [43]. A pair of optical pulses are coupled into a non-linear medium such that they optically mix if they propagate through the crystal with some degree of temporal overlap. In this way, the

interaction of the pulses in the crystal produces a third optical pulse at a different center wavelength.

The scheme has the advantage that the timing detection is done directly in the optical domain, which provides immunity to temperature variation and excess noise, in contrast to direct photodetection. The sensitivity can also be quite great since the process depends on the interaction of femtosecond regime pulses. However, in contrast to optical frequency locking or interferometric techniques, the measurement range is on the order of a few pulse widths—not simply a single cycle of an electromagnetic wave at few hundred terahertz.

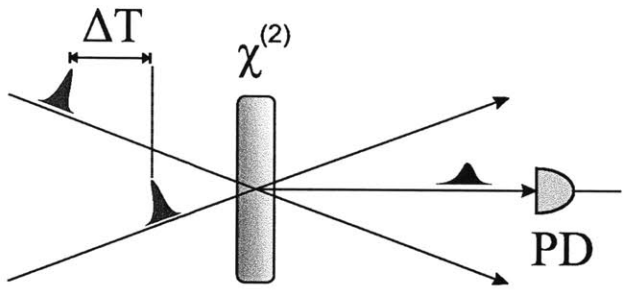

FIG. 11. The relative timing between a pair of ultrafast optical pulses can be directly measured in the optical domain with sum-frequency generation. If the fundamental, red, pulses temporarily overlap to some extent in the non-linear crystal, they will mix to produce a blue pulse which is detected by the photodetector [40], [43]. The energy of the blue pulse is determined, in part, by the degree of temporal overlap of the fundamental pulses in the crystal.

However, this basic scheme is susceptible to amplitude noise. Both timing fluctuations and amplitude fluctuations influence the pulse energy of the sum-frequency generated pulse.

2.2 Balanced Optical Cross-correlation

Sub-femtosecond, ultrafast timing distribution and synchronization requires ultrahigh resolution pulse envelope timing detection that is both amplitude and temperature invariant. The balanced optical cross-correlator permits attosecond resolution timing detection of the pulse envelope, without influence from the optical carrier phase. Furthermore, since the timing detection is performed entirely in the optical domain, it is highly temperature invariant, with ultralow noise and ultrahigh resolution. Of course, as a balanced detection scheme, it is also amplitude insensitive.

There are two main types of balanced optical cross-correlators (BOC), which differ in the way the cross-correlation is performed. The "thin crystal" BOC requires an external, fixed group delay element [32], while the "long crystal" BOC takes advantage of the anisotropic group velocity of a non-linear crystal to provide a distributed group delay [36].

2.2.1 Long-crystal Balanced Optical Cross-correlation

The long crystal BOC is designed with a non-linear, $\chi^{(2)}$ crystal such that the pulses under measurement propagate through the crystal at different group velocities, as shown in FIG. 12. The crystal should be long enough that the pulses move entirely past each other during propagation through the crystal. Pulses may propagate at different group velocities by use of an anisotropic crystal under Type-II phase matching, whereby each pulse sees a different optical crystal axis [44].

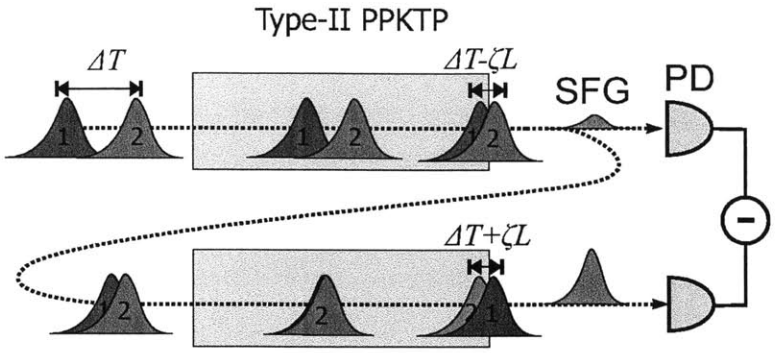

FIG. 12. "Long crystal" balanced optical cross-correlator where the pulses propagate at different group velocities, performing a cross-correlation inside the crystal.

To model the long crystal BOC, first consider the coupled wave equations governing Type-II sum frequency generation, for which the SFG pulse is in the rest frame [45], [46].

$$\left[\frac{\partial}{\partial z}+\left(\frac{1}{v_1}-\frac{1}{v_3}\right)\frac{\partial}{\partial t}\right]E_1 \approx 0 \tag{2.14}$$

$$\left[\frac{\partial}{\partial z}+\left(\frac{1}{v_2}-\frac{1}{v_3}\right)\frac{\partial}{\partial t}\right]E_2 \approx 0 \tag{2.15}$$

$$\frac{\partial}{\partial z}E_3 = i\frac{d_{eff}\omega_3}{n_3 c}E_1 E_2 \tag{2.16}$$

Since the conversion efficiency is typically less than 3% in practice, we may neglect depletion in (2.14), (2.15) [36]. Also, since the crystal need only be a few millimeters in length, it is not necessary to consider group velocity dispersion, either. In fact, for KTP, the dispersion is only 50 fs^2/mm at 1550 nm. Lastly, we use a quasi-phase-matched (QPM), periodically poled KTP crystal (PPKTP), with 100 nm phase matching bandwidth [44], [47]. We can therefore safely neglect phase matching without loss of accuracy. However, it is not possible to neglect the temporal walkoff, since that is integral to the operation of the long crystal device. Previous analysis neglected to properly consider the temporal walkoff, arriving at a result more akin to the short crystal regime [48]. This is made apparent by considering that conversion efficiency should not depend on crystal length (so long as the crystal is sufficiency long), since the interaction length is set by the temporal walkoff.

Rather, the ordinary and extraordinary pulses move through the crystal at different velocities, undistorted. As a result (2.14), (2.15) have the simple solutions (2.17) and (2.18).

$$E_1(t,z) = E_1\left(t - \left(\frac{1}{v_1} - \frac{1}{v_3}\right)z\right) \tag{2.17}$$

$$E_2(t,z) = E_2\left(t - \left(\frac{1}{v_2} - \frac{1}{v_3}\right)z - \Delta T\right) \tag{2.18}$$

We have introduced in (2.18) the offset between the pulses, ΔT. This parameter is the quantity the BOC ultimately measures with attosecond precision.

The solution to the SFG pulse is given by (2.19).

$$E_3(t,z) = i\frac{d_{eff}\omega_3}{n_3 c}\int E_1(t,z)E_2(t,z)dz \tag{2.19}$$

However, the large, 100 nm phase matching bandwidth in PPKTP is obtained by exploiting the zero group velocity mismatch (zero-GVM) properties of KTP between 1550 nm and 775 nm [44]. The zero-GVM condition is satisfied provided $v_3 = 2v_1v_2/(v_1+v_2)$. In other words, the SFG pulse propagates between the fundamental pulses, as they move apart. In practice, since $v_2 \approx v_1 + \delta$ to within a few percent, we can simplify the zero-GVM condition by the approximation $v_3 \approx (v_1+v_2)/2$. Therefore, the SFG pulse propagates nearly in between the fundamental pulses, at their center of mass.

Similarly, we can then approximate the difference in inverse group velocities of the pulses in terms of the parameter ζ, which is the pulse walkoff.

$$\zeta \approx \pm\left(\frac{1}{v_1} - \frac{1}{v_3}\right) \approx \mp\left(\frac{1}{v_2} - \frac{1}{v_3}\right) \tag{2.20}$$

We can then rewrite (2.19) as

$$E_3(t,\Delta T) = i\frac{d_{eff}\omega_3}{n_3 c}\int E_1(t-\zeta z-\Delta T)E_2(t+\zeta z)dz \tag{2.21}$$

Finally, we shall solve (2.21) for a Gaussian pulse, as specified by (2.22), where E_p is the peak field strength of the pulse and τ_p is the pulse width.

$$E_i(t,z) = E_p \exp\left(-\left(t/\tau_p\right)^2\right) \tag{2.22}$$

Thus, for a Gaussian pulse, we may compute the SFG field as a function of time and ΔT, with (2.23).

$$E_3(t,\Delta T) = i\frac{d_{eff}\omega_3}{n_3 c}E_p^2 \int \exp\left(-\frac{2t^2 + 2\zeta^2 z^2 - 2t\Delta T + \Delta T^2 + 2\Delta T\zeta z}{\tau_p^{\,2}}\right)dz \tag{2.23}$$

To simplify the result, without loss of fidelity, we take the crystal to be infinitely long. Therefore, forward propagation through the crystal occurs for z = [-∞, 0], while backward propagation occurs for z = [0, ∞]. Performing the integration with these limits, we find the solution to the SFG field is given by (2.24), where 1^*=1 for the forward pass, and -1 for the backward pass.

$$E_3(t,\Delta T) = i1^* \frac{\sqrt{\pi} d_{eff}\omega_3 E_p^2 \tau_p}{2\sqrt{2} n_3 c\zeta} e^{-\frac{4t^2 - 4t\Delta T + \Delta T^2}{2\tau_p^2}} \left(\operatorname{erf}\left(\frac{\Delta T}{\sqrt{2}\tau_p}\right) + 1^*\right) \tag{2.24}$$

However, the photodetector is a slow detector which is sensitive only to the total pulse energy, and cannot resolve the pulse shape. Therefore, we compute the total SFG pulse energy by (2.25). Also, we must integrate the beam intensity, assuming an effective mode area with a radius *w*. The cycle averaged beam intensity is proportional to the magnitude square of the field amplitude. Below, the constant of proportionality is the index of refraction over the impedance of free space, $\eta_0 \approx 377\ \Omega$.

$$\begin{aligned} J_3(\Delta T) &= \pi w^2 \int_{-\infty}^{\infty} \frac{n_3}{2\eta_0} \left|E_3(t,\Delta T)\right|^2 dt \\ &= \left|E_p\right|^4 \left(\frac{w d_{eff}\omega_3}{\zeta c}\right)^2 \frac{\pi^{5/2}\tau_p^3}{32 n_3 \eta_0} \left(\operatorname{erf}\left(\frac{\Delta T}{\sqrt{2}\tau_p}\right) + 1^*\right)^2 \end{aligned} \tag{2.25}$$

The balanced photodetector voltage is given by (2.26), where G is the gain of the transimpedance amplifier in Ohms, α is the quantum efficiency of the detector in A/W and f_R is the pulse repetition rate in Hertz.

$$\Delta V(\Delta T) = G\alpha f_R (J_3^+ - J_3^-) \tag{2.26}$$

Therefore, we arrive at the expression for the long crystal BOC transfer function, (2.27), in units of Volts. It is proportional to the error function of the timing offset, ΔT.

$$\Delta V(\Delta T) = G\alpha f_R |E_p|^4 \left(\frac{w d_{eff} \omega_3}{\zeta c} \right)^2 \frac{\pi^{5/2} \tau_p^3}{8 n_3 \eta_0} \operatorname{erf}\left(\frac{\Delta T}{\sqrt{2}\tau_p} \right) \tag{2.27}$$

However, the key consideration is the timing sensitivity of the BOC. We also wish to perform the substitutions given in (2.28), in order to recast the timing sensitivity in easily measured parameters.

$$\begin{aligned} E_p &= \frac{2}{w} \left[\frac{\sqrt{\ln(2)} \eta_0 P_{CW}}{\pi^{3/2} f_R n \tau_{FWHM}} \right]^{1/2} \\ \tau_p &= \frac{\tau_{FWHM}}{\sqrt{2\ln(2)}} \end{aligned} \tag{2.28}$$

P_{CW} is the average power of a Gaussian pulse train with full-width-half maximum of the intensity given by τ_{FWHM}. The slope of the transfer function becomes

$$\frac{\partial \Delta V}{\partial \Delta T} = \frac{\sqrt{2}\ G\alpha \eta_0 \omega_3^2 d_{eff}^2 P_{CW}^2}{\pi f_R w^2 n_3^3 c^2 \zeta^2} e^{-\frac{\ln(2)\Delta T^2}{\tau_{FWHM}^2}} \tag{2.29}$$

Since we are interested only in the slope at the balanced point, or zero crossing of the transfer function, we take the limit as ΔT→0, eliminating the exponential term from (2.29). This yields the timing sensitivity, (2.30), in Volts per second.

$$K = \lim_{\Delta T \to 0} \frac{\partial \Delta V}{\partial \Delta T} = \frac{\sqrt{2}\ G\alpha \eta_0 \omega_3^2 d_{eff}^2 P_{CW}^2}{\pi f_R w^2 n_3^3 c^2 \zeta^2} \tag{2.30}$$

Finally, we arrive at the expression, K, for the sensitivity of the BOC in V/s. As expected, we find that the sensitivity is proportional to the square of the average power, but surprisingly, does not depend on the pulse width, to first order. Furthermore, there is no lumped group delay which must be tailored to the pulse width. Instead, the conversion efficiency is determined by the interaction length, which is set by the ζ parameter. Of course, since sensitivity scales with the inverse square of the spot size, w, development of

an integrated waveguide, long crystal BOC is being pursued to achieve robust, highly efficient timing detection [30]. It should also be noted that we neglect diffraction, and presume that the depth of focus (Rayleigh range) is much longer than the interaction length of the pulses. In practice, this is often the case, even in a bulk device, due to the need to use long focal lengths to accommodate the mechanical arrangement.

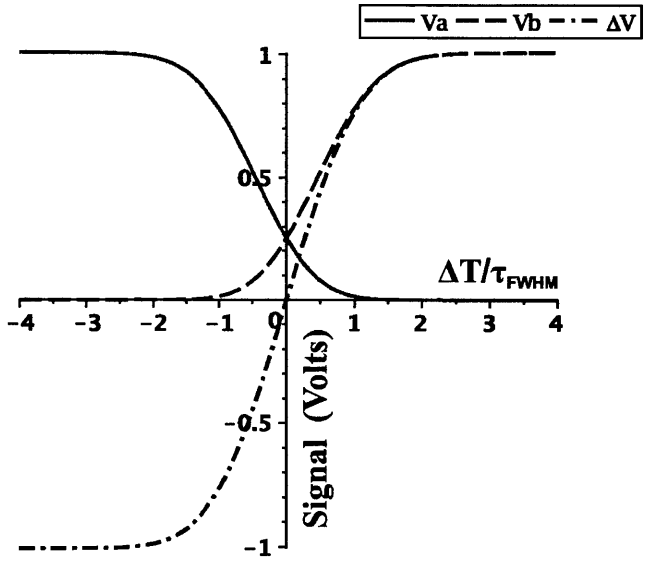

FIG. 13. Normalized photodetector signal verses normalized pulse timing offset, ΔT, for each photodetector branch (Va and Vb). Also shown is the balanced signal, ΔV = Va – Vb.

Interestingly, neglecting diffraction, because there is a relationship between the pulse width and the interaction length, the sensitivity for the long crystal BOC is independent of pulse length variation, to the extent the average power remains constant. For this reason, the long crystal BOC is advantageous for timing applications where the pulse compression may fluctuate. For instance, in a system that compensates for fiber drift by varying the insertion of glass prisms or other material.

For the PPKTP-BOC used in the timing link discussed later, we have n = 1.8, α = 0.5 A/W, G = 10^6 Ohms, d_{eff} = 2/π·3.6 pm/V, P_{CW} = 10 mW, f_R = 200 MHz, ζ = 150 fs/mm, and w ≈

25 μm, which yields a theoretical sensitivity of 180 mV/fs. In practice, the actual sensitivity is usually a factor of four lower since the photodetector may be equipped with optical bandpass filters with a ~50% transmission efficiency, as well as a 50 Ohm electrical output impedance, providing another factor of two reduction in signal when fed to a matched load. This result compares favorably to the typical experimental sensitivity of 20 to 30 mV/fs, since d_{eff} has been well characterized for PPKTP [30].

2.2.2 Thin-crystal Balanced Optical Cross-correlation

The thin crystal balanced optical cross-correlator is analogous to the long crystal BOC, except the pulses do not (or said more precisely, "need not") move with respect to each other throughout the crystal [32]. Since the available crystals may not have favorable parameters at the wavelength of interest, a long crystal BOC could be harder to engineer. In contrast, the short crystal design has the advantage that commercial, off the shelf crystals can be used without periodic polling. One disadvantage, however, is that a lumped group delay element must be designed and tailored to the particular pulse shapes being measured, rendering the short crystal detector less flexible.

Instead of relying on a long crystal to impart a spatially distributed delay between pulses, the short crystal BOC requires only a differential group delay (DGD) element which is external to the crystal, as shown in FIG. 14. This element may take nearly any form, depending on the requirements.

For example, the short crystal BOC has been used for timing detection between few-cycle laser pulses, with the same polarization but different wavelengths, for coherent beam combining [32]. In this case, all that is required is a simple plate of fused silica as the group delay element and a standard LBO crystal for the SFG.

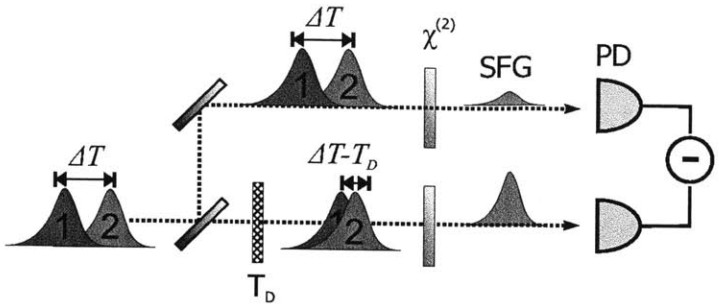

FIG. 14. Diagram of a short crystal balanced optical cross-correlator. The pulses are split into two branches, with each branch sent through a non-linear crystal. However, a differential group delay device, imparting a delay of TD, is placed in one branch.

For the short crystal BOC, we further neglect the group velocity walkoff of (2.14) and (2.15), in which case the solutions are given by (2.31) and (2.32). As before, ΔT is the parameter the BOC measures—the time between the pulses when entering the BOC.

$$E_1(t,z) = E_p \exp\left(-\left(t/\tau_p\right)^2\right) \tag{2.31}$$

$$E_2(t,z) = E_p \exp\left(-\left((t-\Delta T)/\tau_p\right)^2\right) \tag{2.32}$$

Thus, (2.21) becomes

$$E_3^A(t,\Delta T) = i\frac{d_{eff}\omega_3}{n_3 c}\int_0^L E_1(t)E_2(t-\Delta T)dz \tag{2.33}$$

for branch A (upper branch), which has no DGD element, and

$$E_3^B(t,\Delta T) = i\frac{d_{eff}\omega_3}{n_3 c}\int_0^L E_1(t)E_2(t-\Delta T-T_D)dz \tag{2.34}$$

for branch B (lower branch), which has a DGD element imparting a delay of T_D. The integration is performed for a crystal of length L, and the SFG pulse energy is computed for each branch using (2.25).

$$J_3(\Delta T) = \frac{\pi^{3/2} w^2 L^2 \left|E_p\right|^4 \tau_p d_{eff}^2 \omega_3^2}{4 n_3 c^2 \eta_0} e^{\frac{\left(\Delta T + T_D^*\right)^2}{\tau_p^2}} \tag{2.35}$$

For (2.35), $T_D^* = T_D$ for branch B and zero for branch A. We then arrive at the short crystal BOC transfer function, V_{BOC}— the same as before with (2.26).

$$V_{BOC}(\Delta T) = \frac{\pi^{3/2} G \alpha f_R w^2 L^2 \left|E_p\right|^4 \tau_p d_{eff}^2 \omega^2}{4 n_3 c^2 \eta_0} \left(e^{\frac{\Delta T^2}{\tau_p^2}} - e^{\frac{(\Delta T + T_D)^2}{\tau_p^2}} \right) \tag{2.36}$$

But for the short crystal BOC, we must ask: what is the optimal choice of T_D, yielding the greatest sensitivity? To this end, we determine the slope at the zero-crossing, which occurs at $\Delta T = -\frac{1}{2} T_D$. We therefore maximize (2.37), for which we find $T_D = \sqrt{2}\tau_p$, or $T_D = \tau_{FWHM}/\sqrt{\ln(2)}$, yields the greatest sensitivity.

$$\lim_{\Delta T \to -T_D/2} \left(\frac{\partial \Delta V}{\partial \Delta T} \right) = \frac{\pi^{3/2} f_R \alpha G w^2 L^2 \left|E_p\right|^4 d_{eff}^2 \omega_3^2}{2 n_3 c^2 \eta_0 \tau_p} T_D e^{-\frac{T_D^2}{4\tau_p^2}} \tag{2.37}$$

Assuming one always operates the short crystal BOC in an optimal configuration, the timing sensitivity becomes (2.38), after substituting for more easily measured parameters.

$$K_{opt} = 8 \sqrt{\frac{2}{\pi^3 e}} \frac{\ln(2) G \alpha P_{CW}^2 L^2 \omega_3^2 \eta_0 d_{eff}^2}{\tau_{FWHM}^2 f_R w^2 n_3^3 c^2} \tag{2.38}$$

In contrast to the long crystal BOC, sensitivity is improved for shorter pulses and longer crystals, up to the point where phase matching and group velocity walkoff begin to limit conversion. Sensitivity is also maximized for transform-limited pulses.

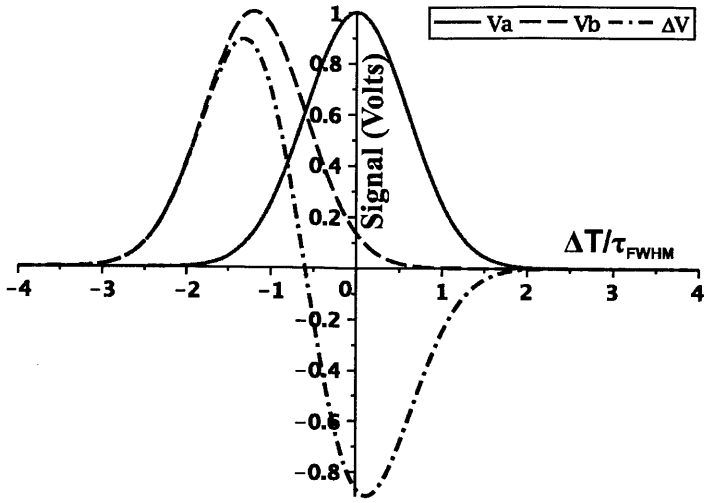

FIG. 15. Normalized photodetector signal versus normalized pulse timing offset, ΔT, for each photodetector branch (Va and Vb). Also shown is the balanced signal, ΔV = Va – Vb. Note, the transfer functions assume an optimal choice of the group delay T_D.

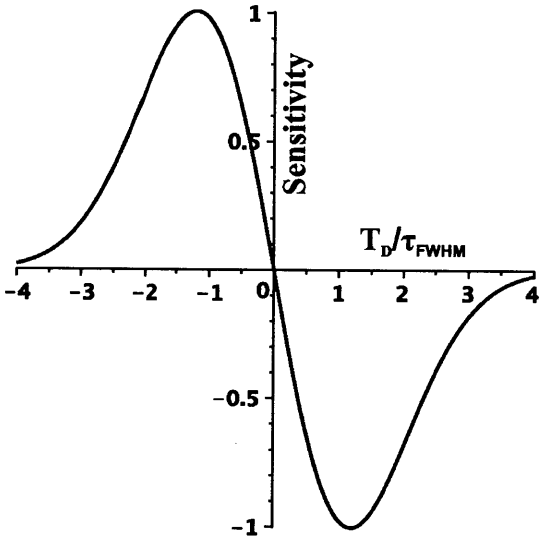

FIG. 16. Plot of cross-correlator slope verses normalized group delay, T_D, for the short crystal balanced optical cross-correlator. Maximum sensitivity occurs for $T_D = \tau_{FWHM}/\sqrt{\ln(2)} \approx 1.2\ \tau_{FWHM}$.

2.3 PPKTP Properties

It is instructive to review the design process for the long crystal PPKTP balanced optical cross-correlator so that BOCs for other wavelengths or pulse durations (e.g. picosecond pulses) may be designed in the future.

For high efficiency sum-frequency generation in a long crystal, broad phase matching bandwidth is needed. However, since the crystal is long, it is also necessary to avoid spatial walkoff from the walkoff angle between the ordinary and extraordinary beams. Spatial walkoff can be eliminated by propagating both beams along principle axes of the crystal. By design, this makes critical phase matching impossible. However, since different principle axes have different *k* vectors in an anisotropic crystal, the only way to achieve phase matching is through quasi-phase matching, which is accomplished by periodically polling the non-linear medium.

Quasi-phase matching (QPM) works by periodically altering the non-linear susceptibility to "shut-off" non-linear conversion until all waves can once again come into phase. The susceptibility is then enabled, and non-linear generation occurs over a short distance, until the phase mismatch again becomes significant. This process is repeated throughout the crystal to prevent the SFG wave from eventually coupling back into the fundamental, as is the case when phase matching is not achieved.

2.3.1 Quasi Phase Matching

We can account for QPM by the addition of a constant wavevector offset term to the typical phase matching condition (2.39), where by the Λ term is the spatial period of the polling. Thus, we first chose Λ so that Δk is zero at a particular frequency, ω.

$$\Delta k(\omega) = k_3(2\omega_0 + 2\omega) - k_2(\omega_0 + \omega) - k_1(\omega_0 + \omega) + 2\pi/\Lambda \tag{2.39}$$

While QPM can achieve perfect phase matching for sum-frequency generation at a single wavelength, the bandwidth depends on the dispersion of the material. It was

recognized that the QPM bandwidth is enhanced by selecting a crystal with a set of principle axes such that the first order Taylor approximation of the phase matching is zero [44]. This condition corresponds to a constraint on the group velocity of the pulses, (2.41), because group velocity is given by (2.40).

$$v_g = \left[\frac{\partial k}{\partial \omega}\right]^{-1} = \dot{k} \tag{2.40}$$

$$\Delta k(\omega) \approx \left[2\dot{k}_3(2\omega_0) - \dot{k}_2(\omega_0) - \dot{k}_1(\omega_0)\right]\omega = 0 \tag{2.41}$$

The so-called "zero group velocity mismatch" (zero-GVM) condition becomes (2.42).

$$v_3 = 2v_1v_2/(v_1 + v_2) \tag{2.42}$$

2.3.2 Crystal Length

It is also necessary to choose the crystal length such that it is adequate for the longest pulse of interest. If the crystal is too short, locking range is sacrificed since the pulses do not completely propagate past each other in the crystal. This limits dynamic range, and reduces the robustness of the control loop.

As can be seen by FIG. 13, the crystal should have a total differential group delay between fundamental pulses of at least $3\tau_{FWHM}$ for the longest pulse of interest. Since the PPKTP is used in a double-pass arrangement, the crystal length should be set to yield a group delay of $1.5\tau_{FWHM}$, or (2.43).

$$L = \frac{3}{2}\tau_{FWHM}\left|\frac{1}{v_y} - \frac{1}{v_z}\right|^{-1} \tag{2.43}$$

2.3.3 Sellmeier Equations and Crystal Properties

Accurate measurement of the crystal index of refraction Sellmeier equations have been compiled from several sources in the literature. For PPKTP, the $2\omega_0$ pulse propagates along the y-axis.

$$n_y^2(\lambda) = A_1 + \frac{A_2}{1 - A_3/\lambda^2} - A_4\lambda^2 \tag{2.44}$$

$A_1 = 2.09930$, $A_2 = 0.922683$, $A_3 = 0.0467695$, $A_4 = 0.0138408$, with λ in μm [44].

$$n_z^2(\lambda) = A_1 + \frac{B}{1 - C/\lambda^2} + \frac{D}{1 - E/\lambda^2} - F\lambda^2 \tag{2.45}$$

$A = 2.12725$, $B = 1.18431$, $C = 5.14852 \cdot 10^{-2}$, $D = 0.6603$, $E = 100.00507$, $F = 9.68956 \cdot 10^{-3}$, with λ in μm [49].

The nonlinear coefficient of PPKTP has been found to be $d_{24} = 3.6$ pm/V, where the effective coefficient for a QPM crystal is $d_{eff} = (2/\pi) \cdot d_{24}$. [30].

With the Sellmeier equations in hand, the wavevectors and group velocities can be calculated for each axis for fundamental and SFG pulses, (2.46) (2.47) [46]. Furthermore, the wavelengths for which the zero-GVM condition is satisfied can be determined by plotting the zero-GVM condition alongside the group velocity of the SFG pulse at $\lambda/2$. For convenience, the group velocity of the SFG pulse is plotted for λ, in FIG. 17. It can be seen that for KTP, the intersection occurs at 1550 nm. A similar analysis with other materials may allow the long crystal BOC technique to be adapted to other wavelengths, such as 1064 nm.

$$v_{g_i} = c\left[n_i - \lambda\frac{\partial n_i}{\partial \lambda}\right]^{-1} \tag{2.46}$$

$$k_i = \frac{2\pi n_i}{\lambda} \tag{2.47}$$

For PPKTP at 1550 nm and 775 nm, the calculated crystal parameters are summarized by Table 1. As can be seen, if we wish to design a crystal for a maximum pulse width of 500 fs, the crystal length should be at least 2.6 mm.

Parameter	Value	Description
$v_{gy}(\omega_0)$	$1.701 \cdot 10^8$ m/s	Group Velocity (y-axis)
$v_{gz}(\omega_0)$	$1.620 \cdot 10^8$ m/s	Group Velocity (z-axis)
$v_{gy}(2\omega_0)$	$1.657 \cdot 10^8$ m/s	Group velocity (y-axis, $2\omega_0$)
$k_y(\omega_0)$	$6.984 \cdot 10^6$ m^{-1}	Propagation constant (y-axis)
$k_z(\omega_0)$	$7.313 \cdot 10^6$ m^{-1}	Propagation constant (z-axis)
$k_y(2\omega_0)$	$1.416 \cdot 10^7$ m^{-1}	Propagation constant (y-axis, $2\omega_0$)
d_{eff}	2.29 pm/V	Effective non-linear coefficient
Λ	46.2 μm	QPM Polling period

Table 1. Properties of PPKTP for 1560 nm and 780 nm wavelengths, as computed from Sellmeier equations for infrared wavelengths found in the literature.

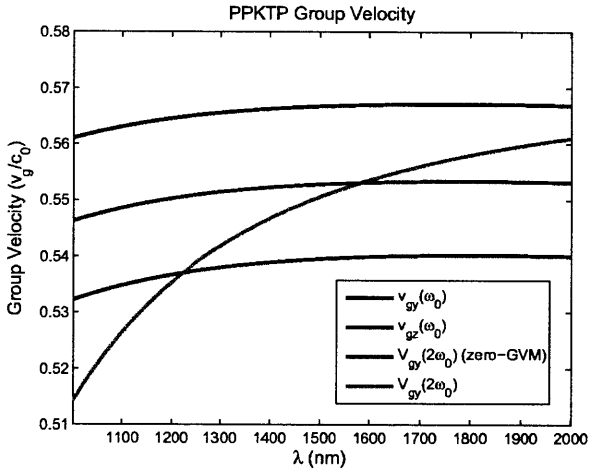

FIG. 17. Plot of normalized group-velocity (v_g/c_0) for y-and z-axes for KTP in the near-IR. Also shown in red is the zero group velocity mismatch (zero-GVM) condition. In light blue is the group velocity of the SFG pulse at λ/2, plotted for convenience at λ. The zero-GVM condition is satisfied when the red and blue lines intersect, at 1550 nm.

3 Timing Stabilized, Fiber-optic, Ultrafast Synchronization System

Ultrafast fiber-optic lasers hold tremendous promise as a practical instrument for synchronizing remote optical and microwave electronic devices via fiber-optic links. Since such lasers simultaneously capture the benefits of exceptionally low-noise optical performance, while pulsing at microwave-frequency repetition rates, it is possible to achieve femtosecond-level timing stability while providing a useful output signal in the microwave band, and at any harmonic of the repetition rate [3], [9], [29].

Having developed an understanding for attosecond timing detection with balanced optical cross-correlation (BOC), we may turn our attention to the stabilization of fiber optic links with sub-femtosecond precision. In particular, BOC provides a means of measuring the time of flight fluctuations of pulses circulating in a fiber link. In this way, these fluctuations can be precisely eliminated, providing a timing stabilized fiber optic link over hundreds of meters.

Ultrafast timing synchronization over optical fiber, based on balanced-optical cross-correlation, is being developed for X-ray free-electron laser facilities requiring femtosecond synchronization over a distance of 300 to 3000 m [35]. However, the BOC method is not limited to measuring timing fluctuations in fiber links. In fact, balanced optical cross-correlation has been explored for attosecond resolution, free-space time-of-flight measurements [50].

However, as with conventional, microwave signal distribution via coaxial cable, optical-fiber links suffer from excess noise due to thermal or mechanical sources, which

corrupts the timing signal being transmitted. Thermal and mechanical stress variations perturb the optical index, fiber length and create birefringence. On the other hand, the ultrafast approach to timing distribution permits femtosecond, and eventually sub-femtosecond, timing synchronization over several kilometers. The specific fiber length is only limited by the need to dispersion compensate the fiber link. Microwave techniques based on coaxial transmission lines cannot achieve femtosecond performance because of the greater thermal instability of the microwave phase detector and associated electronics, as well as the limited timing resolution of microwave frequency signals [9], [37], [42], [51].

Ultrafast timing distribution has other benefits, beyond sensitive timing control. The ultrafast laser is unique in that it combines the convenience of a microwave signal source with the low-noise performance of an optical oscillator. As such, with an ultrafast laser, it is not necessary to distribute a narrow-band, 200 THz optical carrier, and then down-convert to a stable microwave signal with another femtosecond laser frequency comb at the remote end [37], [52]. By distributing the entire pulse train, additional modelocked lasers at the link outputs are not necessary to convert an optical frequency to a microwave frequency.

Nevertheless, there are challenges for ultrafast timing distribution which must be overcome. In particular, performance is limited by polarization mode dispersion (differential group delay) in the single mode fiber. This manifests as a breakdown in the fundamental assumption of timing distribution: that the round-trip propagation is related to the single-trip propagation in a predictable way. Additionally, non-linear fiber effects can couple the optical intensity to the pulse timing, if the pulse energy is great. Also, since the BOC is polarization sensitive, long-term, remote synchronization of lasers through the fiber link requires a polarization maintaining output at the end of the link.

3.1 System design

The ultrafast, timing stabilized fiber link corrects for fluctuations in the time-of-flight of pulses traveling through the optical fiber. Such fluctuations are typically on the order of tens or hundreds of picoseconds, depending on the temperature fluctuations and the length of the fiber. To remove the timing uncertainty from pulses exiting the fiber link, the round-trip propagation time of pulses in the link is stabilized to new pulses emitted directly by the master laser.

Therefore, the fundamental assumption of timing distribution is that the time taken for the signal to reach the remote location (one-way delay) is related to the round-trip propagation delay in a known way. If so, it is possible to measure the round-trip delay, and make corresponding adjustments to the fiber time-of-flight to keep the transmitted signal uncorrupted by fluctuations in the transmission line.

This basic scheme is described in FIG. 18. The master laser, which may be loosely synchronized to a microwave frequency standard, is an additive pulse mode-locked, erbium fiber soliton laser, emitting at 1550 nm with a pulse repetition rate of 200 MHz [53]. A high repetition rate is desirable to keep pulse energy low, while permitting a higher average optical power in the link. This strategy is effective because timing sensitivity scales as the square of the average power over repetition rate (2.30). A half-wave plate (not shown) adjusts the splitting ratio at the PBS. Typically, no more than 10 mW is launched into the fiber link to prevent non-linear effects from occurring. In addition, an optical isolator directly after the fiber laser output is required to prevent the returning pulses from reentering the oscillator.

Most implementations of the fiber link rely on a partially reflecting Faraday Rotating Mirror (FRM) at the end of the link to back-reflect a portion of the transmitted signal. The FRM has the benefit of preserving the polarization of the back-reflected light, regardless of

the fiber birefringence. The relative time, Δt_{il}, between the returning pulse and a new pulse from the laser, emitted mT_R seconds later, is measured with the BOC. This is known as the in-loop timing error, Δt_{il}, and may be written as in (3.1).

$$\Delta t_{il} = T_{rt}(t) + 2T_C(t) - mT_R \rightarrow 0 \tag{3.1}$$

If the round-trip time-of-flight of the pulses returning from the link, T_{rt}, remains constant, then the returning pulses should overlap in time with the new pulses from the master laser. Any change in the time-of-flight is detected as a shift in the relative timing and a corresponding corrective delay, T_C, of exactly $-\Delta t_{il}/2$ is introduced into the fiber link to cancel fluctuations in T_{rt}. In this way, Δt_{il} always remains zero. After measurement of the timing error from the in-loop BOC, the corrective delay is applied by the locking electronics to the link. This delay is imparted with a variable, free space delay line consisting of a high-resolution stepper motor and a 40μm travel piezoelectric stack. The free space delay line avoids the differential group delay and birefringence problems associated with a piezoelectric fiber stretcher—at the cost of increased variable insertion loss. This variable insertion loss may couple to timing drift if the pulse energy in the link is high. Also, a free space delay can accommodate much longer delays than a fiber stretcher, which is useful for long fiber links or links in extreme environments.

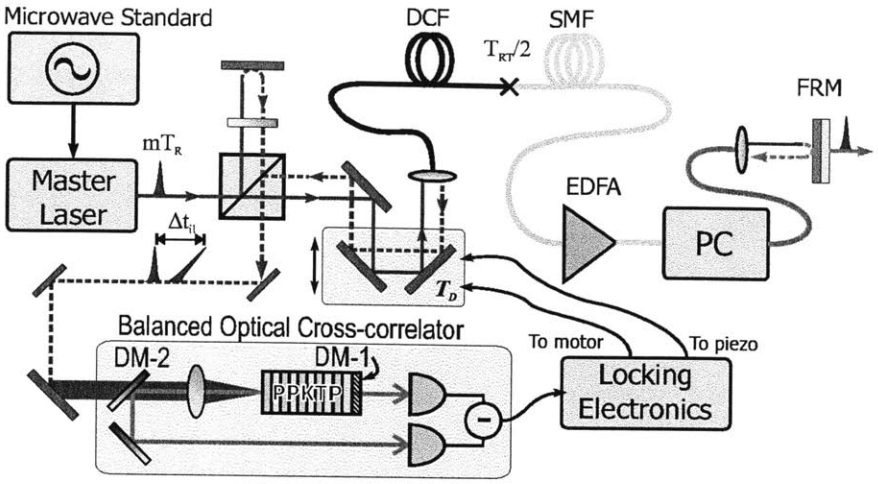

FIG. 18. Layout of an ultrafast timing link with PM output, based on a balanced optical-cross-correlator. DCF; dispersion compensating fiber. SMF; single mode fiber. PC; polarization controller. EDFA; erbium doped fiber amplifier. FRM; faraday rotating mirror. DM-1; dichroic mirror (T: 1550, R: 775 nm). DM-2; (T: 775, R: 1550 nm).

The fiber link in the experimental apparatus consists of 300 meters of Corning SMF-28e fiber, spliced to approximately 40 meters of Avanex dispersion compensating fiber (DCF). The DCF compensates for both dispersion and dispersion slope. For links longer than about 50 m, dispersion slope, or third order dispersion (TOD), becomes significant since the master laser produces 167 fs pulses [54].

It is also necessary to incorporate an erbium doped fiber amplifier (EDFA) in the fiber link to bi-directionally amplify circulating pulses. Typical splice loss for the DCF to SMF has been found to be 1 dB, although 0.7 dB should be possible with optimized fusion splicer routines [55]. Additionally, the round trip loss in the FRM is typically slightly above 50%, or 4 dB. The polarization controller has a loss of 1.2 dB. A system typically incorporates at least five fiber connectors, with a loss of 0.2 dB each, for FC/APC. Thus a typical link will have a total forward single-pass loss of 7 dB, or a round-trip loss of 12 dB.

Finally, an electronic polarization controller (Thorlabs DPC5500) is placed at the end of the link to polarize the output into a 1 m section of PM fiber.

3.2 Experimental results

We aim to understand the limits of timing distribution in the fiber link by conducting long-term tests. Ultimately, long-term timing transfer from the master laser to a remote laser is demonstrated through the fiber link, entirely by optical means.

The length of the fiber link sets an upper bound on fiber noise cancelation, due to causality. The system cannot correct for variations faster than the round-trip time of flight. But for a 10 km fiber, this places a limit on the bandwidth of only $f_c = c/2Ln \approx 10\,\mathrm{kHz}$, which is sufficient to correct for virtually all fiber fluctuations.

3.2.1 Single-link Measurement

To characterize the performance of the timing link system by itself, a 300 m SMF-28e fiber link with 40 m of DCF is stabilized in the laboratory. The PM output of the link is then combined with a portion of the free space output of the master laser, and sent into a second BOC, as shown in FIG. 19.

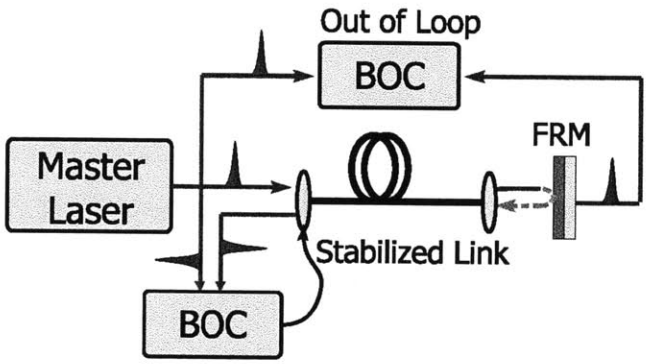

FIG. 19. Long-term timing transfer stability of the link was assessed by comparing the output of the stabilized link to the uncorrupted signal directly from the master laser, through 340 m of fiber.

The results, as shown in FIG. 20, demonstrate 5 fs rms drift over 168 hours, while the system corrected for 25 ps peak-to-peak fluctuations in the fiber. Such long term operation is possible due to the integrated polarization controller and robust, non-interferometric, balanced optical cross-correlator. The great majority of the residual drift is from slow fluctuations correlated to the daily temperature fluctuations of the laboratory. Moreover, the residual out-of-loop jitter is only 1 fs rms [0.1 Hz, 100 kHz] [9].

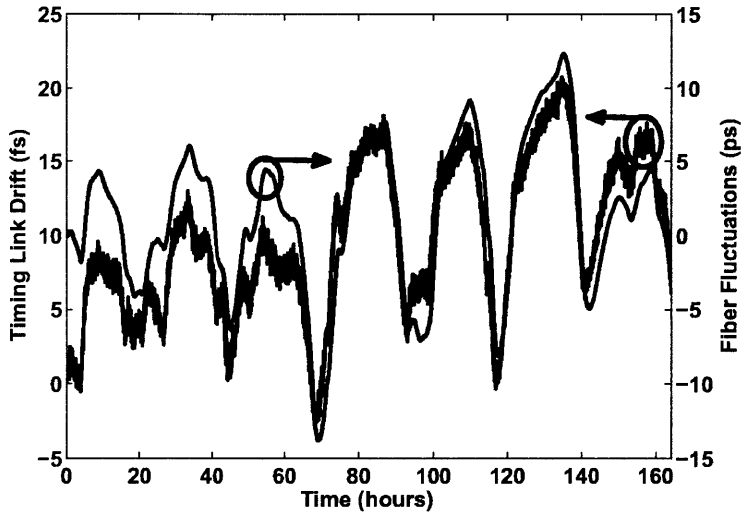

FIG. 20. Out-of-loop drift of the timing link over 168 hours of operation. The blue trace shows the drift of the link output, while the black trace shows the fiber fluctuations for which the link corrected for.

3.2.2 Dual-link Measurement

To is also useful to compare homodyne measurements to a heterodyne measurement for the purpose of excluding common-mode noise from the laser oscillator and drift in the optics. For this purpose, two separate timing link systems were constructed with careful attention paid to the free space optics. As shown in FIG. 21, the laser source is split into separate paths by the first polarizing beam splitter (PBS). The splitting is accomplished on

temperature stabilized Invar alloy breadboards to reduce thermal drift. The layout is also made symmetrical between the links to help eliminate common-mode thermal drift. Finally, at the end of the link, the outputs are recombined on temperature stabilized Invar boards, and sent into the out-of-loop BOC.

In the dual link test, an Optiphase fiber stretcher consisting of 40 m of SMF-28e is incorporated into the link, instead of a free space piezo actuated mirror. Although the fiber stretcher has the benefit of providing several picoseconds of delay at high speed, it has the drawback of significant polarization mode dispersion and voltage dependant birefringence. A typical unit had a measured differential group delay of 83 fs. The piezo resonance at 16—18 kHz permits at least 1 kHz closed loop bandwidth.

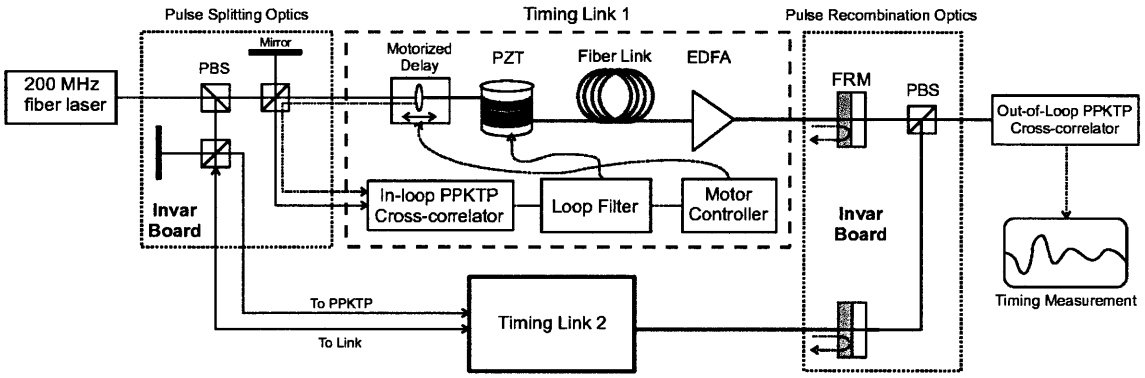

FIG. 21. Schematic of dual-link measurement apparatus. Pulse splitting and recombination optics are mounted on Invar alloy, temperature stabilized breadboards in symmetrical fashion to reduce common mode drift. The dual-link apparatus uses Optiphase fiber stretchers for the fast group delay, as opposed to free space piezo actuated mirrors. Fiber link length is approximately 300 m with 40 m additional in the fiber stretcher.

Over a period of 72 hours, both links were locked while the relative drift in the outputs was monitored with a low-nose, 16-bit resolution National Instruments digital acquisition module. Additionally, the temperature of the dispersion compensated, 300 m Corning SMF-28e fiber link and the Invar boards were monitored. The power output of the

recombined pulses from the links was monitored to verify that the calibration of the BOC remained consistent.

The results are presented in FIG. 22 for temperature, motorized group delay, timing drift and link output power. Timing drift is observed to be 17 fs pk-pk, or 6.4 fs rms over 72 hours, with a sampling rate of 1 Hz. On the other hand, the system corrected for 9 ps pk-pk drift in the fiber. Curiously, it is apparent that one link experienced greater fiber drift than the other. This is likely the result of excessively tight winding of the fiber link around the plastic spool. Therefore, for the dual-link test, which used un-jacked fiber wound tightly around a plastic spool, some of the drift is likely due to stress imparted by the thermal expansion of the spool.

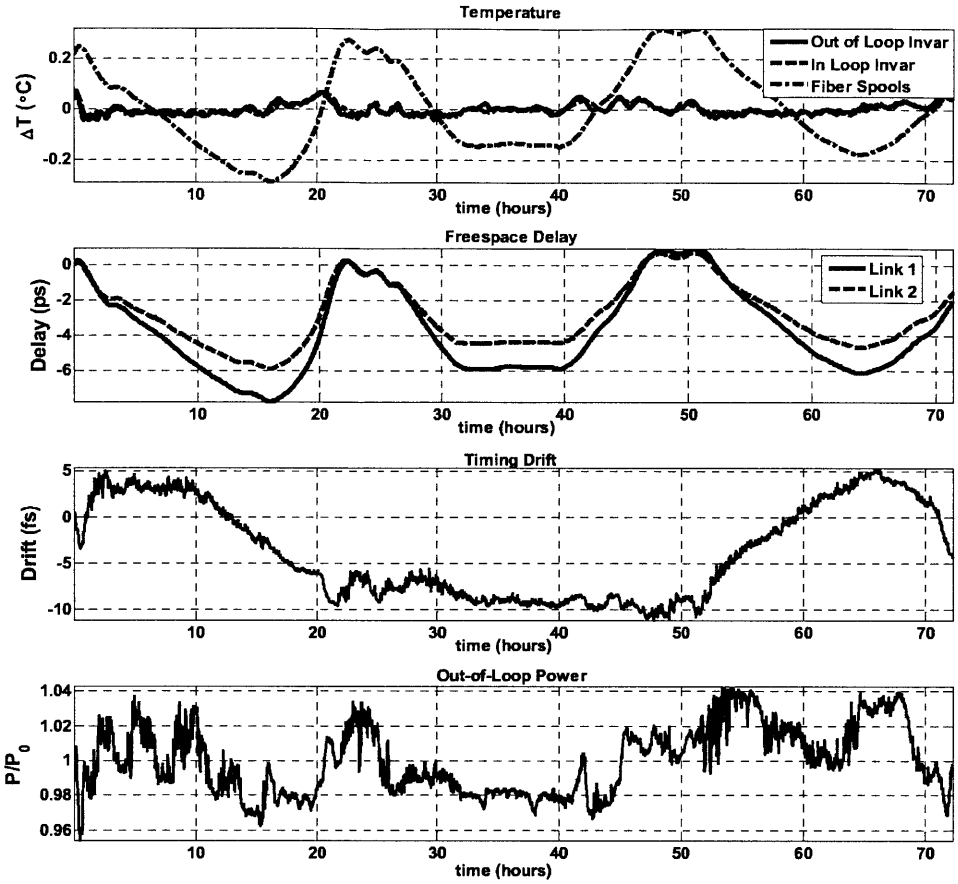

FIG. 22. Time-domain signals from dual-link measurement, spanning 72 hours. From top to bottom, measurements include temperature, motorized group delay, timing drift and combined link output power. Timing drift is observed to be 17 fs pk-pk, or 6.4 fs rms over 72 hours, with a sampling rate of 1 Hz.

The results from the 72 hour, dual-link measurement are combined with high-frequency measurements from a Hewlett Packard Vector Signal Analyzer to produce a composite frequency domain jitter spectral density plot. FIG. 23 shows the jitter spectral density from 35 μHz to 100 kHz. The portion from 35 μHz to 0.5 Hz is simply the power spectral density of the time-domain data in FIG. 20, divided up into nine, eight hour long sections. The JSD of each eight hour section is averaged. For the high frequency portion

from 0.5 Hz to 100 kHz, 100 averages are performed. The JSD shows that the timing stability is less than 1.5 fs from 100 kHz down to 10^{-4} Hz, or approximately 10,000 second timescales. Below 10^{-4} Hz, the drift increases due to the slow, daily drift which is largely correlated with temperature.

The origin of the slow drift appearing beyond one hour time scales is thought to be caused by differential group delay (or polarization mode dispersion) in the optical fiber. Time changing birefringence, due either to thermal stresses on the fiber or the voltage applied to the fiber stretcher, alters the polarization of the pulses within the link. In turn, the DGD leads to out-of-loop drifts, which can be substantial if the DGD of the fiber link is large. Therefore, care should be taken to use only the lowest PMD or DGD components in the fiber link.

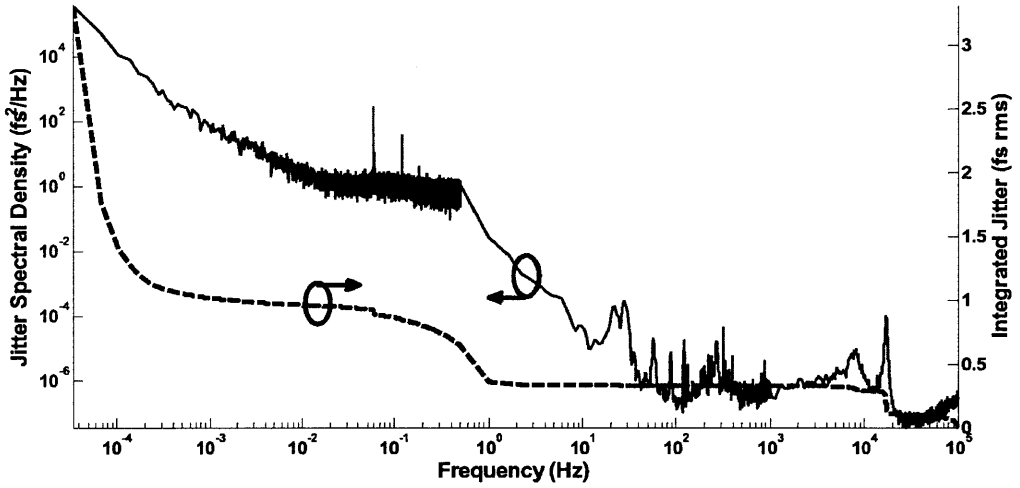

FIG. 23. Composite jitter spectral density plot of dual-link timing jitter from 35 μHz to 100 kHz. The portion below 0.5 Hz is recorded with a low-noise analog-to-digital acquisition board, while the high-frequency segment is recorded with a Hewlett-Packard Vector Signal Analyzer (low-noise spectrum analyzer extending to DC). Total integrated jitter is only 1 fs rms from 100 kHz to 10^{-3} Hz (~1,000 seconds).

3.2.3 Timing Transfer Measurement

To be useful, remote lasers must be synchronized to the timing stabilized output of the fiber links. It is therefore important to demonstrate entirely optical timing transfer from master to remote laser via the link. In this way, the drift of the entire timing transfer technique can be assessed. A continuous measurement over several hours is also necessary to validate the long term stability of the BOC timing transfer technique.

As shown in FIG. 24, the output from the link and of a fraction of the remote laser power is sent to a third BOC, which is used to synchronize the remote laser to the link output. This is done by adjusting an intracavity piezo in the remote laser to keep the remote pulse train phase locked to the link output. The performance of the timing transfer is assessed by sending a fraction of the power from the remote laser, along with some power from the master laser, into the out-of-loop BOC.

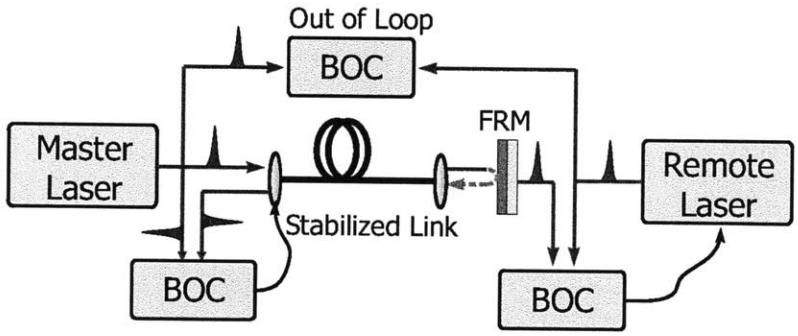

FIG. 24. Schematic of timing transfer system from master to remote laser, through the stabilizing timing link. The performance is assessed by recording the signal from the out-of-loop BOC.

The residual drift for the timing transfer is only 2.3 fs rms over 3.5 hours of operation, as shown by FIG. 25.

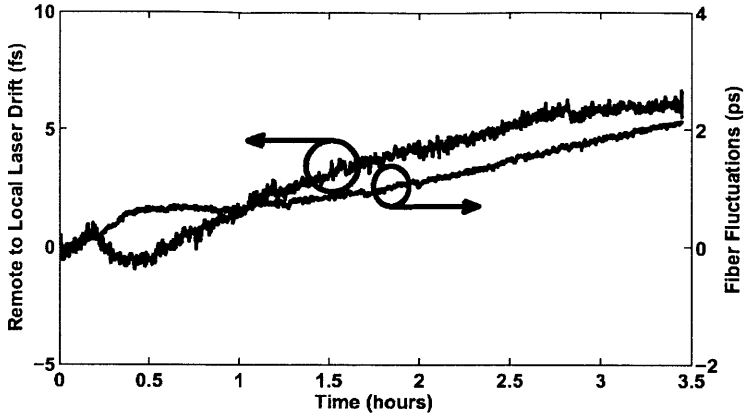

FIG. 25. Timing transfer performance from laser to laser through the stabilized fiber link. The blue line is the out-of-loop drift, while the black line is the fiber fluctuations for which the system corrected.

The timing jitter spectrum at the out-of-loop BOC was measured from 0.01 Hz to 10 MHz, as shown in FIG. 25. From FIG. 26, it can be seen that the optical synchronization and timing link does not introduce significant noise within the locking bandwidth of 18 kHz. Although the resulting synchronization is within 17 fs rms [0.01 Hz, 10 MHz], most of this high-frequency jitter is attributable to spurious noise in our particular master oscillator at 10 kHz, and the servo bump at 18 kHz. In practice, direct, free space synchronization to within 2.6 fs rms has been achieved with the same technique, but with a lower noise fiber laser [29]. This demonstrates that robust, long-term, optical timing transfer via ultrafast pulse trains, with femtosecond precision, is possible.

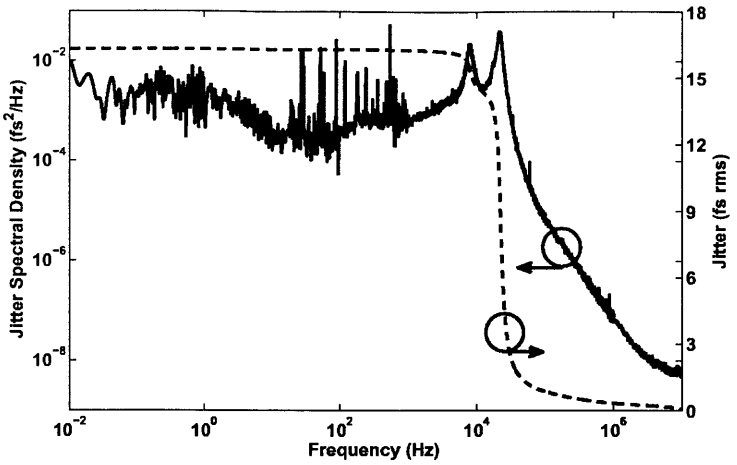

FIG. 26. Timing jitter spectrum of residual, out-of-loop drift for timing transfer from laser to laser, through the stabilized link. The integrated jitter is shown by the black line. The bulk of the jitter is due to noise in the mode-locked laser and servo bump. However, the high-frequency noise remains below 2 fs rms [20 kHz, 10 MHz].

3.3 Limitations and analysis

3.3.1 Theoretical resolution

Perhaps the most important specification of the timing detector is the resolution, which is set by the noise. For an ideal BOC, the noise is due to shot noise and thermal or Johnson noise in the transimpedance amplifier, as illustrated by FIG. 27. In practice, there are other technical noise sources, including dark current in the photodiodes and excess noise in the amplifier. However, the magnitude of these noise sources depends on the technical details in the engineering of the photodetector, and so we are interested only in the fundamental limit. In any event, shot noise and thermal noise are typically the dominant sources.

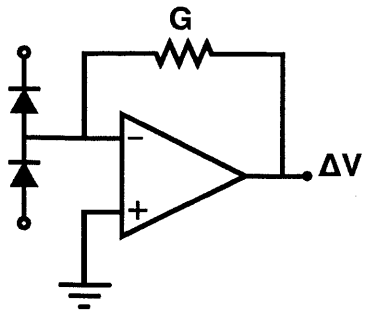

FIG. 27. Schematic of an ideal transimpedance amplifier, where shot noise current fluctuations are detected by the photodiodes and thermal noise voltage fluctuations are generated by the feedback resistor, G. The output voltage noise, ΔV, can be expressed as a timing uncertainty via the timing sensitivity, K.

The shot noise current fluctuations for a balanced photodetector are given by the well known expression, (3.2), where the current fluctuations have been converted to timing fluctuations by multiplication by G/K (transimpedance gain over timing sensitivity).

$$\sigma_{sn} = 2G\sqrt{q\alpha P_{CW}^{SFG}\Delta f}\Big/K \tag{3.2}$$

In this expression, $P_{CW}^{SFG} = f_R J_3(\Delta T = 0)$ is the average power of the converted light, incident on each detector, Δf is the photodetector signal bandwidth, and q is the elementary charge. Note, P_{CW} can be taken as the average power for which $V_{BOC} \approx 0$, since it is the role of the feedback electronics to keep the signal at zero mean.

Additionally, the thermal noise voltage fluctuations of the feedback resistor is given by the well known expression for Johnson noise, as in (3.3), which has also been expressed as timing uncertainty by division by K.

$$\sigma_{th} = 2\sqrt{k_B T G \Delta f}\Big/K \tag{3.3}$$

Here, k_B is Boltzmann's constant, T is the temperature of the photoetector, and K is the sensitivity of the BOC, as previously derived. For the short and long crystal BOCs, we therefore find the resolution is given by (3.4)—(3.7). For the following, superscript *L* and *S*

refer to the long and short crystal device, respectively, while subscript *th* and *sn* refer to thermal and shot noise, respectively.

$$\sigma_{th}^{L} = \frac{\sqrt{2k_B T \Delta f}\,\pi f_R w^2 \zeta^2 n^3 c^2}{\sqrt{G}\alpha P_{CW}^2 \omega_3^2 d_{eff}^2 \eta_0} \tag{3.4}$$

$$\sigma_{th}^{S} = \frac{\sqrt{2e\pi^3 k_B T \Delta f}\,\tau_{FWHM}^2 f_R w^2 n^3 c^2}{8\ln(2)\sqrt{G}\alpha P_{CW}^2 L^2 \omega_3^2 d_{eff}^2 \eta_0} \tag{3.5}$$

$$\sigma_{sn}^{L} = \left(\frac{2\pi^3}{\ln(2)}\right)^{1/4} \frac{\zeta w c}{2P_{CW} d_{eff} \omega_3} \sqrt{\frac{\tau_{FWHM} f_R q n^3 \Delta f}{\alpha \eta_0}} \tag{3.6}$$

$$\sigma_{sn}^{S} = \left(\frac{2e\pi^3}{\ln(2)^3}\right)^{1/4} \frac{wc}{4P_{CW} L d_{eff} \omega_3} \sqrt{\frac{\tau_{FWHM}^3 f_R q n^3 \Delta f}{\alpha \eta_0}} \tag{3.7}$$

For the PPKTP long crystal detector, with a photodetector bandwidth of 1 MHz and all other parameters the same as previously mentioned, σ_{sn}= 13 as rms and σ_{th}= 0.7 as rms. Perhaps it is not surprising that increasing the gain does not improve the shot noise limit, only the thermal noise limited resolution. Therefore, it is necessary to achieve greater optical conversion to reduce shot noise.

3.3.2 Polarization Mode Dispersion

To achieve femtosecond stable long-term timing distribution, higher order effects which impact timing performance must be considered. Most pernicious of these effects is Polarization mode dispersion (PMD). PMD, as pertains to ultrafast timing distribution, is the effect whereby the two orthogonally polarized components of a pulse propagate at different group velocities [56]. In other words, the differential group delay (DGD) between of pulses in the link also depends on polarization. This manifests as a breakdown in the fundamental assumption of timing distribution: that the one-way and round-trip propagation delays are related in a known way. The issue is that randomly changing birefringence in the fiber, due to thermal changes or mechanical stresses, changes the

polarization of the pulse, and therefore the propagation time for the forward path in an unknown way. Understanding and limiting DGD in the fiber link is therefore key to long-term timing distribution with femtosecond precision.

The pulses coupled out at the end of the link may evolve through any number of polarization states, and thus propagate along a random mixture of fast-and slow-PMD axes before reaching the end of the link. The result is that the time required for the pulse to travel once through the fiber is unknown, while the round-trip group delay is fixed by the Faraday Rotating Mirror (FRM) [57]. This leads to an observed drift at the output. In practice, one sees a distorted pulse with a center of mass that shifts around in time, by simply stressing the fiber at one point by hand.

Typical single-mode telecommunications fiber, such as Corning SMF-28e has a specified maximum PMD of 200 fs/√km, although this value varies considerably depending on the manufacturing variations of the particular fiber. PMD can also be greatly increased by coiling or stressing the fiber.

Mechanical stress on the fiber during link installation adds to the innate PMD from the manufacturing process. In practice, this can be a significant source of PMD. For this reason, great care must be taken to avoid coiling or stressing the fiber. Previous implementations of the timing link relied on a piezoelectric fiber stretcher consisting of 40 m of SMF tightly wound around a 5 cm piezo. This device has a measured DGD of 83 fs. Perhaps more troubling, the act of stretching the fiber with the piezo induces birefringence. This birefringence couples the piezo signal to drift in the output, within the closed-loop piezo bandwidth of 1 kHz. As a result, a free space piezo mirror and motorized delay stage was implemented to replace the fiber stretcher.

To directly measure the DGD effect, consider the out-of-loop drift of the timing link as the polarization of the launched pulse is varied with a zero order $\lambda/2$ plate and $\lambda/4$ plate placed just before the input fiber collimator. As shown in FIG. 28, the measurement describes the magnitude of the DGD which was present for our initial link with high PMD

components [9]. For this test, the polarization at the link output was held constant by the polarization controller while the waveplate was varied. The link incorporated the fiber stretcher, DCF and 300 m of SMF, which was wound around a fiber spool. More than 200 fs peak-to-peak drift at the output was measured simply by rotating the waveplate. By eliminating the stretcher and using jacketed fiber, the PMD is significantly reduced. Unstressed fiber links consisting of Corning SMF-28e nominally have a typical PMD_Q of only 60 fs/√km, as specified by Corning. Thus, we expect typical PMD-origin drift of 33 fs peak-to-peak for a 300 meter link with properly jacketed fiber without a fiber stretcher.

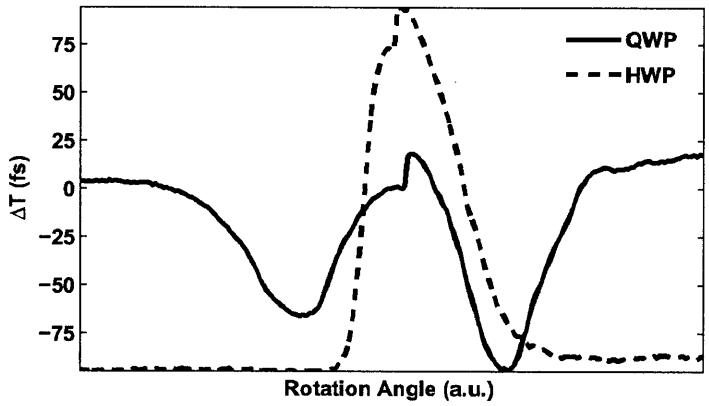

FIG. 28. Out-of-loop drift of the timing link, with fiber stretcher and un-jacked fiber, as half and quarter wave plates are rotated. During this measurement, the link output polarization controller was enabled. The waveplates are placed directly before the pulses are coupled into the fiber link.

3.3.3 Non-linearity

PMD is not the only contributing factor to timing link drift at the femtosecond level. Non-linear effects in the fiber can distort the pulse shape, and lead to measurement errors in the BOC. In effect, fiber non-linearity places a limit on the maximum pulse energy that can propagate in the link without impacting timing transfer. Ideally, neglecting non-linearity, in a dispersion and dispersion slope compensated link, pulses should return to the same shape as when they were injected into the link by the laser. However, self-phase

modulation (SPM) generates intensity dependent temporal phase that distorts the compression in the DCF. Therefore numerical simulations of pulse propagation in the link were studied. These simulations are based on the well known split-step method for solving the non-linear Schrödinger equation, (3.8) [54].

The simulation follows the standard split-step technique whereby the exact solution for dispersion is implemented in the frequency domain, and the non-linear solution is solved in the time domain with the fourth order Runge-Kutta method. In other words, to propagate a pulse along a fiber a distance Δz, the pulse is first chirped by applying the frequency dependant phase in the frequency domain, according to a step size of Δz/2. Next, the half-chirped pulse is propagated a distance Δz by applying the non-linear operators with Runge-Kutta. Finally, the remaining half of the dispersion is applied for a distance Δz/2 in the frequency domain.

$$\frac{\partial}{\partial z}A(z,t)=\left[-i\frac{\beta_2}{2}\frac{\partial^2}{\partial t^2}+i\frac{\beta_3}{6}\frac{\partial^2}{\partial t^2}+j\gamma|A|^2\right]A(z,t) \tag{3.8}$$

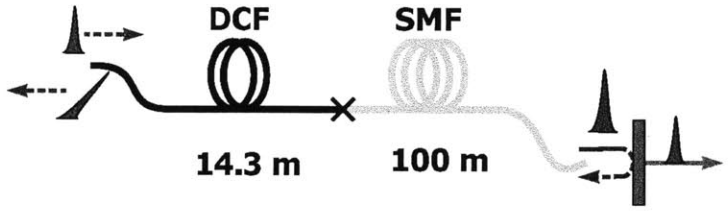

FIG. 29. Schematic of pulse propagation simulation of timing link, consisting of 14.3 m of DCF and 100 m of SMF-28. The end mirror is assumed to be 100% reflecting, in place of implementing an EDFA. The DCF has 1/7th the 2nd and 3rd order dispersion, but about four times greater nonlinear coefficient.

The simulation models pulse propagation through a lossless link consisting of 100 m of Corning SMF-28e and an equivalent amount of Avanex DCF, for 167 fs pulses from the soliton laser, as shown in FIG. 29. DCF has a specified non-linear parameter, γ, about 3.7 times greater than for SMF-28e, due to the 20 um^2 effective mode area of DCF [58]. The

simulations capture dispersion, dispersion slope and SPM. Self-steepening and Raman scattering are also considered, but found to impact performance only at much greater pulse energies.

The simulation was conducted for both one-way and round trip propagation through the link. The pulse timing in each case was then calculated by computing the BOC and interpolating the zero-crossing time offset. For comparison, the center of mass of the pulse was calculated—which is defined as the true pulse timing. The effective out-of-loop timing error was then found by subtracting the round trip timing shift from twice the one way timing shift, in accordance with (3.1).

These simulations reveal that the pulse timing and energy are coupled predominantly through SPM. For high energies, the pulse begins to split in two after recompression in the DCF on the return trip. Thus, the BOC transfer function also begins to split, as shown for the long crystal BOC in FIG. 30. This effect forces the feedback electronics to track the zero-crossing at earlier times. For an SMF-28e and DCF based lossless link, this effect becomes significant at 40 pJ, or 8 mW at 200 MHz, as shown in FIG. 31. Indeed, this effect was encountered experimentally, and placed a limit on the pulse energy so that high pulse quality is maintained.

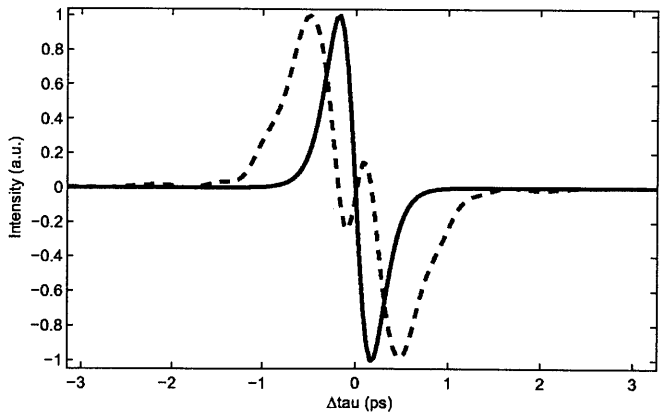

FIG. 30. Balanced optical cross-correlation at the in-loop BOC for 1 mW average power (solid blue) and 9 mW (dashed green). At 8 mW, the pulse begins to split, pushing the zero crossings outward.

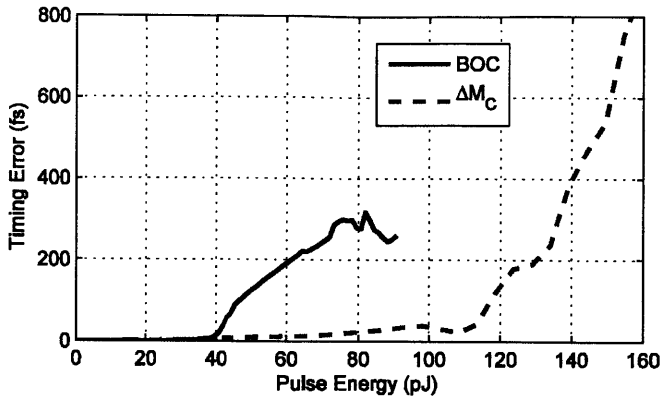

FIG. 31. Timing link error vs. average optical power for a simulated link of 100 m SMF-28 and 14.3 m DCF. The error is the difference in pulse timing, as measured via a simulated BOC, between a BOC at the link output (single-pass) and an in-loop BOC (round-trip). Non-linearity becomes significant for this lossless link at 8 mW, or 40 pJ.

3.3.4 Non-linear effects at high pulse energies

While the simulation can account for intrapulse Raman scattering and self-steepening effects, it was found that these effects do not play a role until much higher pulse energies. At very high pulse energies, beyond 100 pJ, the pulse becomes so distorted that the BOC fails to provide any meaningful measurement of pulse timing. Therefore, one must resort to the center of mass definition of pulse timing (4.16) to obtain meaningful results.

Above 100 pJ, the spectral broadening from SPM becomes significant enough that the dispersion slope in the fiber leads to a timing shift. The spectrum broadens asymmetrically, and the pulse position shifts to earlier time. This process reaches a threshold at about 100 pJ, or 20 mW. The effect is calculated by measuring the shift in the center of mass of the pulse, as shown in FIG. 32.

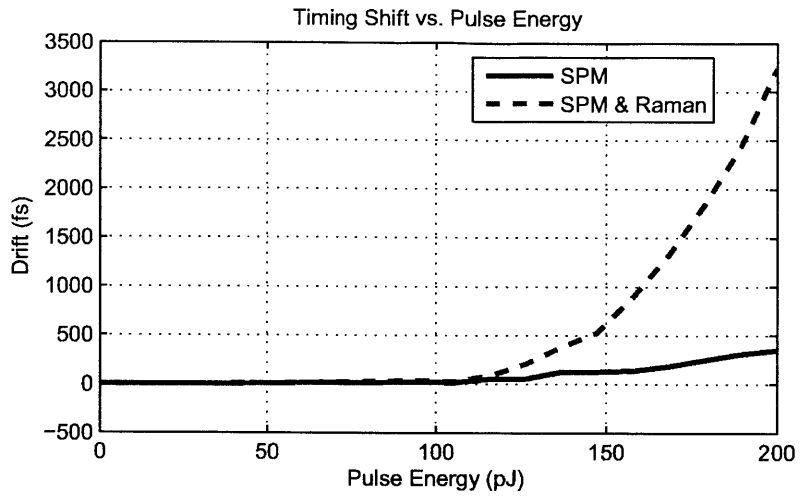

FIG. 32. Timing shift (drift) at link output verses pulse energy for simulated timing link. The simulations assume 167 fs $sech^2$ pulses. The timing shift is calculated based on the center of mass of the pulse, not the BOC. The drift due to self-phase modulation (SPM) alone is shown in solid blue. The drift due to SPM and the Raman shift is shown in dotted red.

For instance, at energies approaching the soliton pulse energy in SMF-28e, the Raman self-frequency shift begins to affect pulse center of mass timing. The Stokes shift from the fiber shifts the pulse to longer wavelengths, or lower energy. However, due to the group velocity dispersion of the fiber, longer wavelengths have different group velocities. Therefore, the pulse propagates at a different rate. As the pulse travels down the link, and heads back, the pulse continues to shift to longer wavelengths. As such, the average velocity for the return path is different than the average velocity of the single-pass propagation. This discrepancy leads to a drift in the output, as pulse energy is varied. FIG. 32 shows the timing shift verses pulse energy due to SPM and the Raman self-frequency shift. The center of mass verses pulse energy is plotted for high pulse energies. Clearly, beyond 100 pJ, the Raman shift begins to induce significant timing link drift.

To study how these effects impact a practical system, the timing shift was measured in the 300 m test bed link by modulating the pump power for typical operating conditions. At an intra-link pulse energy of 25 pJ, a modulation of ±3.6 pJ produced a measured out-of-loop timing shift of ±5 fs drift, or 1.4 fs/pJ, as shown in FIG. 33. In the test bed, the insertion

loss variation was typically 10% over the full travel of the free space delay. Therefore, when operating below the 40 pJ limit, the intensity induced drift is expected to be only a few femtoseconds. This drift, however, becomes significant for sub-femtosecond timing transfer links.

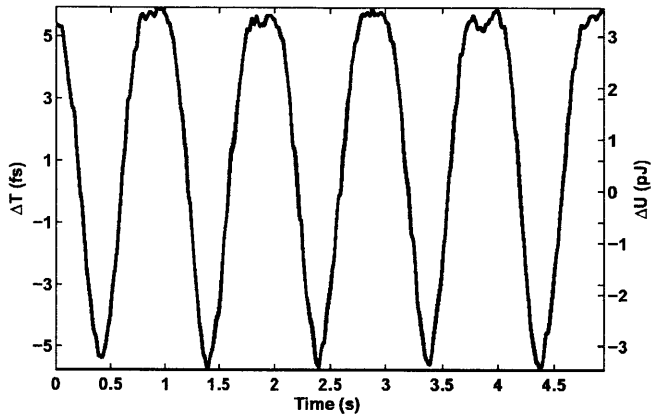

FIG. 33. Measurement of out-of-loop timing drift verses intra-link pulse energy. Intra-link EDFA is modulated at 1 Hz such that pulse energy varies by ±3.6 pJ, producing a ±5 fs drift, or 1.4 fs/pJ. Average pulse energy is 25 pJ.

3.3.5 Strategies for reducing non-linear effects

Since the sensitivity of balanced optical cross-correlation is so great, large pulse energy is not needed for the synchronization of remote lasers to the timing stabilized output of the fiber link. Nevertheless, if pulse energy beyond 40 pJ is eventually required, non-linear effects can be reduced by externally chirping and recompressing the pulse outside of the fiber link. By pre-chirping the pulse before entering the fiber, and then recompressing at the end of the link, pulse energy can be increased, somewhat analogous to the principle of chirped pulse amplification. For example, by doubling the pulse width from 167 fs to 334 fs, the critical pulse energy is increased from 40 pJ to 60 pJ. Such a chirped pulse fiber link could be constructed, for instance, with volume Bragg gratings or with a grating stretcher and compressor pair.

On the other hand, one may suppose that non-linear effects can be more easily reduced by using narrower bandwidth, longer duration, transform limited pulses—instead of designing a chirped pulse fiber link. However, simulations (see FIG. 34) reveal that reducing optical spectrum does not improve timing error. Although longer pulses do have less peak power for the same pulse energy, they disperse more slowly in the fiber, thus negating any benefit from reduced peak power. In fact, the simulations suggest that the power dependent drift is more pronounced for longer (transform limited) pulses. This is because the longer pulses with narrower optical spectrum disperse more slowly in the fiber, accumulating non-linear phase along a greater distance.

Also, in a real-world situation, it is unlikely that the length of the DCF fiber exactly cancels the dispersion of the SMF link. The primary reason is that the fiber length cannot be arbitrarily chosen, but most be such that the round-trip group delay is an integer multiple of the repetition rate of the master oscillator. Otherwise, the back reflected pulse will not overlap in time with new pulses from the laser at the in-loop BOC. Therefore, there is typically a mismatch of several tens of centimeters of SMF-28 fiber.

One may therefore suppose that by intentionally choosing a length of DCF that does not totally compress the pulse, fiber non-linear effects can be mitigated. In a perfectly compensated link, the pulse is compressed to the transform limit in three positions in the fiber: at the beginning when initially launched, at the end of the link and when returning to the beginning. If the length of DCF is too short, then the pulse is compressed only at the beginning and somewhere in the DCF after the back reflection. Indeed, by shortening the DCF, simulations in FIG. 34 do predict that the critical pulse energy increases by approximately 5 pJ to roughly 45 pJ. Since shortening the DCF still induces pulse compression at some point inside the DCF, the improvement is limited.

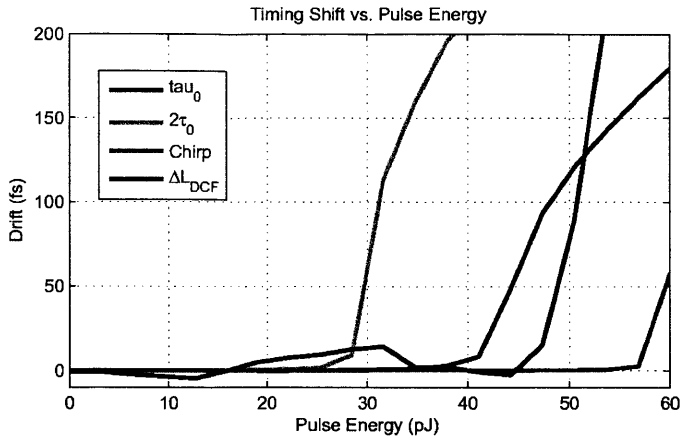

FIG. 34. The effect of various schemes for reducing non-linear timing shift is compared, based on simulations. In blue, the baseline drift for the prototypical system. In green, the drift when the pulse width is doubled to 334 fs (transform limited). In red, the drift when the 167 fs pulse is chirped to 334 fs. In black, the drift after reducing the length of the DCF by 1 m less than that for perfect compensation. It is apparent from the above results that external stretching and compressing of the pulse is the most effective scheme.

4 Complete Characterization of Ultrafast Laser Timing Jitter with Quantum-limited Resolution

The full characterization of the timing jitter of ultrafast pulse trains is necessary to advance the theory and to improve the noise properties. Eventually, improved understanding will lead to the development and adoption of lower jitter mode-locked lasers for applications, such as photonic analog-to-digital conversion [59]. However, the low noise of femtosecond, passively mode-locked lasers makes timing jitter measurements extremely challenging. To progress toward the goal of practical, ultrafast microwave signal sources, a method for fully characterizing the timing jitter fluctuations is necessary. In this way, progress toward engineering more robust and lower noise sources can be achieved.

In this chapter, experimental work toward the characterization of the timing jitter of ultrafast, passively mode-locked fiber lasers is demonstrated. The chapter begins with a review of the fundamental origin and properties of timing jitter, in a way that facilitates an intuitive understanding for engineering. Secondly, measurements of the jitter for both 80 MHz stretched pulse erbium doped fiber lasers and for 200 MHz erbium soliton fiber lasers are presented.

4.1 Timing Jitter Models

Haus et al. have developed advanced, analytical noise models by studying perturbations to the Non-linear Schrodinger Equation (NLSE) describing the laser dynamics [60]. This soliton laser noise model is particularly useful for understanding and optimizing the noise of laser systems for which it describes well. However, one may be interested in other types of lasers or in the underlying noise source itself—and not the laser dynamics. To this end, we present a more elementary model that describes the physical origin of timing jitter on a more fundamental level.

Work by *R. Paschotta* has also concentrated on complex numerical models for modeling timing jitter. These models have the advantage of providing accurate results for lasers systems for which there is no known analytical solution. However, since the models rely on brute-force simulation of many thousands of round-trips, with results averaged to form the power spectral density, the efficiency is quite low [8]. Numerical models also do not readily lend themselves to gaining engineering intuition for the development of lower noise lasers.

On the other hand, we seek the simplest, most intuitive and general model which captures the major parameters influencing timing jitter performance. In this way, intuition is gained that can guide future development toward lower jitter sources.

4.2 Timing Jitter Theory

Before presenting measurements of timing jitter in ultrafast fiber lasers, it is useful to gain a greater understanding of the basic physics which lead to timing jitter. To this end, a simple, yet intuitive understanding of timing jitter can be gained by considering the action of spontaneous emission upon an optical pulse, as developed by *R. Paschotta* [61]. This treatment expresses the timing jitter imparted to a pulse from additive white noise due to

spontaneous emission. The timing jitter imparted to a particular pulse shape is found by way of calculating the second moment of the noisy pulse.

First, consider the ideal ultrafast ring laser, which consists of a gain medium, an output coupler (loss) and a mode-locking mechanism, as in FIG. 35. Ideally, one expects that pulses are emitted from the output coupler every T_R seconds, which is given by the cavity length over the group velocity of the pulses. Instead, every time the pulse passes through the gain medium, some spontaneous emission noise is added to the pulse, which perturbs the center of mass of the pulse in time. Each time the pulse travels through the ring, the timing uncertainty grows as additional noise is added. As the noise from roundtrip to roundtrip is independent, the timing uncertainty (or variance) adds linearly. Thus, in a passively mode-locked laser, there is no restoring force, and so the pulse undergoes a random walk. This is to say, the timing uncertainty of the pulse continues to diffuse forever, such that the ultrafast laser has infinite timing jitter from DC to the Nyquist frequency.

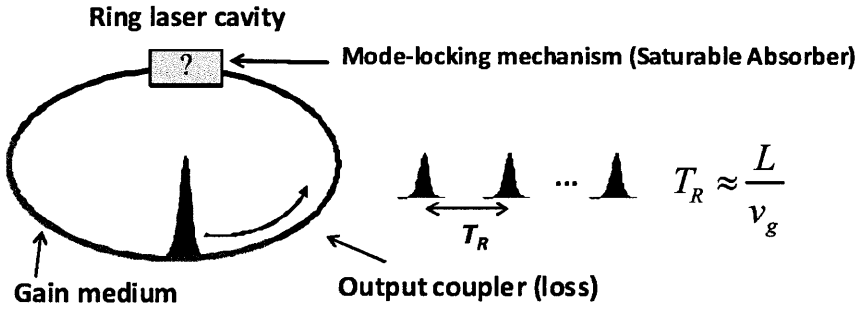

FIG. 35. Simplified model of an ultrafast ring laser. The cavity consists of a gain medium, an output coupler (loss) and a mode-locking mechanism, or saturable absorber. Ideally, the pulses should be coupled out every roundtrip time T_R, given by the cavity length over the group velocity.

4.2.1 Power Spectral Density of Spontaneous Emission

As the first step toward arriving at the quantum-origin timing jitter of an ultrafast laser, consider the power spectral density of spontaneous emission due to an amplifier of gain g [62], [63]. It is a well known principle of quantum mechanics that the probability of spontaneous emission into a single mode is equal to the stimulated emission rate, B_{21}, rate with a single photon occupying the mode [63]. Therefore, the spontaneous emission rate into a single mode for a two-level system, A_{21}, is given by (4.1).

$$A_{21}^{m} = h\nu B_{21} \tag{4.1}$$

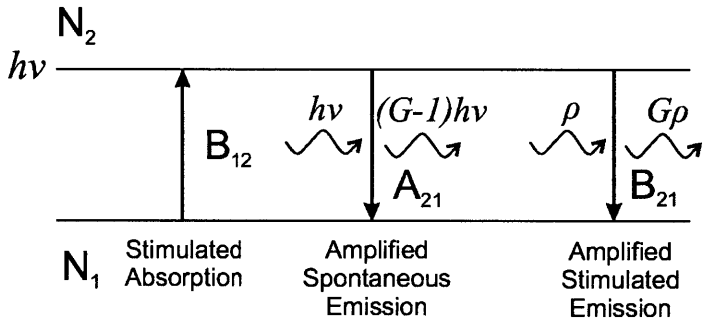

FIG. 36. Diagram of two-level atomic transition. Interactions of the transition with the electromagnetic field include stimulated absorption, spontaneous emission and stimulated emission.

Since we are interested only in single mode fiber lasers, there exists only two modes—one for each polarization state. We therefore ask, what is the increase in the number of photons in a single mode, ΔN_m, after traveling a distance Δz through the gain medium (4.2)? For the following, N_2 is the number density (number per unit volume) of excited atoms, N_1 is the density of ground state atoms, ρ is the radiation density (in energy per unit volume) in the mode, B_{21} is the stimulated emission rate and B_{12} is the stimulated absorption rate. Additionally, we may eliminate the radiation density, ρ, by recognizing that

it is equal to the number density of photons per mode times the photon energy (4.3). Furthermore, we assume $B_{21} = B_{12}$ for a non-degenerate transition.

$$\begin{aligned}\Delta N_m &= \left[(\text{stim. emiss.}) + (\text{stim. abs.}) + (\text{spon. emiss.})\right]\Delta z \\ &= \left[N_2 B_{21}\rho - N_1 B_{12}\rho + N_2 B_{21} h\nu\right]\Delta z\end{aligned} \tag{4.2}$$

$$\rho = h\nu N_m \tag{4.3}$$

Note, the increase in the photon number for a particular mode, ΔN_m, due to stimulated emission and stimulated absorption is proportional to the radiation density in the mode. In the same way, as mentioned earlier, the increase in photon number due to spontaneous emission is proportional to the radiation density, assuming there is always exactly one photon per unit volume in the mode, with energy hv. In other words, it is as if the emission is driven by exactly one photon that always exists in each mode. This phenomenon is ultimately the fundamental source of quantum noise from the laser gain medium.

Next, we define the inversion parameter n_{sp} (4.4), which is a measure of how completely inverted the gain medium is.

$$n_{sp} = \frac{N_2}{N_2 - N_1} \tag{4.4}$$

Then, we recast (4.2) as a differential equation, and integrate both sides along the length of the optical fiber (4.5).

$$\int_0^L \frac{dN_m}{N_m + n_{sp}} = \int_0^L \left(N_2 - N_1\right) B_{21} h\nu \, dz \tag{4.5}$$

Performing the integration, one arrives at (4.6).

$$\ln\left[\frac{N_m(L) + n_{sp}}{N_m(0) + n_{sp}}\right] = B_{21} h\nu \left(N_2 - N_1\right) L \tag{4.6}$$

Assuming there is no gain saturation (small signal gain regime), the argument of the natural log on the left hand side of (4.6) is really the number of photons out of the amplifier over the number of photons into the amplifier. This is the gain, G, as in (4.7).

$$e^{B_{21}h\nu(N_2-N_1)L} = e^{gL} = G \tag{4.7}$$

Solving (4.6) in terms of G (4.7), we arrive at the number of photons in a mode, (4.8). On the right hand side of the equation, the first term represents the amplified input signal (from z = 0), while the second term represents the amplified spontaneous emission noise.

$$N_m(L) = GN_m(0) + n_{sp}(G-1) \tag{4.8}$$

Now that we have the number density of photons *per frequency mode* at the output of the amplifier, for a single spatial mode, we can derive the power spectral density of the spontaneous emission noise. For each frequency *v* there exists a mode with photon energy *hv*. Thus, in a bandwidth of Δv, a given mode has a power per unit area of P_m^{ASE} (4.9).

$$P_m^{ASE} = h\nu N_m^{sp}(L)\Delta\nu \tag{4.9}$$

Therefore, the power spectral density (PSD) is simply the power per unit frequency, S_{ASE} (4.10).

$$S_{ASE}(\nu) = n_{sp}(G-1)h\nu \tag{4.10}$$

Immediately, one sees that, for a high gain amplifier (G >> 1) which is perfectly inverted (N_2 >> N_1), the PSD (4.10) can be simplified to (4.11).

$$S_{ASE}(\nu) \approx Gh\nu \approx Gh\nu_0 \tag{4.11}$$

Interestingly, the PSD is not white, but rather increases linearly with frequency. However, since near-infrared and visible lasers operate at a center frequency from 200 THz to 400 THz, with a bandwidth of not more than 10%, we may approximate the PSD as white over this bandwidth. In other words, we take $\nu = \nu_0$ to be the center frequency of the optical spectrum.

4.2.2 Timing Jitter from Spontaneous Emission

Having arrived at the power spectral density of amplified spontaneous emission, the timing uncertainty added to a pulse can be computed from the second moment of the noisy pulse. The noisy pulse can be written as the sum of the noiseless pulse envelope and of the spontaneous emission noise (4.12), where $\overline{A}(t)$ is the pulse envelope and $\delta A(t)$ the ASE.

$$A(t) = \overline{A}(t) + \delta A(t) \tag{4.12}$$

Next, we recognize that the autocorrelation that produces the PSD of the spontaneous emission (4.11) must have the form of (4.13). Recall that the autocorrelation of white noise is the delta function.

$$R_{ASE}(t-t') = \langle \delta A(t) | \delta A(t') \rangle = h\nu G \delta(t-t') \tag{4.13}$$

In the same way, we also surmise that the noisy pulse intensity can be written by (4.14), where the noise power is simply given by (4.15). The noise power in the pulse is not simply the magnitude of the ASE noise, $\delta A(t)\delta A^*(t)$ because an additive noise does not also add in power. Instead, imagine a pulse with peak amplitude A_0. If a small perturbation is added, δA, then the total power becomes $P = |A_0 + \delta A|^2$. Thus, we compute the noise power from the total power, minus the noiseless pulse power. Furthermore, we make the simplifying approximation that the noise power outside the pulse envelope is negligible, $\delta A \delta A^* \approx 0$.

$$P(t) = \overline{P}(t) + \delta P(t) \tag{4.14}$$

$$\begin{aligned} \delta P &= AA^* - \overline{A}\overline{A}^* \\ &= (\overline{A} + \delta A)(\overline{A}^* + \delta A^*) - \overline{A}\overline{A}^* \\ &= \overline{A}^* \delta A + \overline{A}\delta A^* + \cancel{\delta A \delta A^*} \\ &\approx \overline{A}^* \delta A + \overline{A}\delta A^* = \overline{A}^* \delta A + \text{c.c.} \end{aligned} \tag{4.15}$$

First, we must define exactly what we mean by pulse timing: the pulse timing is the center of mass of the pulse intensity (4.16), normalized by the total pulse energy.

$$t_p \equiv \frac{\int tP(t)\,dt}{\int P(t)dt} \tag{4.16}$$

Since we are interested in the timing uncertainty, we calculate the variance, or second moment, of the pulse timing noise—assuming zero mean noise (4.17).

$$\sigma_t^2 = \left\langle t_p^2 \right\rangle = \frac{1}{E_p^2}\left\langle \left(\int t\delta P(t)\,dt \right)^2 \right\rangle \tag{4.17}$$

In the following, we work with the above relations to reduce (4.17) to an expression containing only known, measurable quantities. First, we can expand the squared integral into two equivalent series integrals, simply by rewriting one of the integrals in terms of t'.

$$\sigma_t^2 = \frac{1}{E_p^2}\left\langle \int\int tt'\delta P(t)\delta P(t')\,dt\,dt' \right\rangle \tag{4.18}$$

Next, we rewrite (4.18) in terms of the noisy pulse amplitude from (4.15).

$$\begin{aligned}
\sigma_t^2 &= \frac{1}{E_p^2}\left\langle \int\int tt' \left(\bar{A}^*(t)\delta A(t) + \text{c.c.}\right)\left(\bar{A}^*(t')\delta A(t') + \text{c.c.}\right) dt\,dt' \right\rangle \\
&= \frac{1}{E_p^2}\int\int tt' \left\langle \left(\bar{A}^*(t)\delta A(t) + \text{c.c.}\right)\left(\bar{A}^*(t')\delta A(t') + \text{c.c.}\right) \right\rangle dt\,dt' \\
&= \frac{1}{E_p^2}\int\int tt'dt\,dt' \left(\bar{P}(t)\left\langle \delta A(t)\delta A^*(t') \right\rangle + \bar{P}(t)\left\langle \delta A^*(t)\delta A(t') \right\rangle\right) \\
&= \frac{1}{E_p^2}\int\int tt'dt\,dt' \left(\bar{P}(t)hvg\delta(t-t') + \bar{P}(t)hvg\delta(t-t')\right) \\
&= \frac{2}{E_p^2}\int\int tt'\bar{P}(t)hvg\delta(t-t')\,dt\,dt' \\
&= \frac{2hvg}{E_p^2}\int t^2\bar{P}(t)dt
\end{aligned} \tag{4.19}$$

Assuming a sech^2 pulse of energy E_p (4.20), we can calculate the integral of (4.19), which is the second moment of the pulse.

$$\bar{P}(t) = \frac{E_P}{2\tau}\text{sech}^2\left(\frac{t}{\tau}\right) \tag{4.20}$$

$$\int t^2 \overline{P}(t) dt = \frac{\pi^2}{12} E_P \tau^2 \tag{4.21}$$

Thus, for a sech^2 pulse, a single pass through the amplifier results in a timing uncertainty of (4.22), where we replace τ by the full width half maximum for a sech^2 pulse.

$$\sigma_t^2 = \frac{\pi^2}{24 \operatorname{arcsec}^2\left(1/\sqrt{2}\right)} \frac{hvg\, \tau_{FWHM}^2}{E_P} \approx 0.529 \frac{hvg\, \tau_{FWHM}^2}{E_P} \tag{4.22}$$

To determine the power spectral density of the timing fluctuations, we first need to determine how the uncertainty grows per round-trip. However, it is well known that the variances of independent random variables simply add [64]. Indeed, since the spontaneous emission from one round-trip to the next is independent, we can leverage this property. Thus, the variance grows linearly with time (4.23).

$$\sigma_{\Delta t}^2(t) = \sigma_t^2 \frac{t}{T_R} \tag{4.23}$$

With the growth of variance in hand, we can compute the PSD of the timing uncertainty fluctuations by way of the Laplace transform of (4.23). The action of the linear increase in variance with time is like a ramp function, for which the Laplace transform is known to be (4.24).

$$S_{\Delta t}(s) = \frac{\sigma_t^2}{T_R} \int t e^{-j\omega t} dt = \frac{\sigma_t^2}{T_R} \frac{1}{s^2} \tag{4.24}$$

Therefore, we conclude that the PSD of the growth of jitter fluctuations in a ring laser are distributed according to (4.25). Again, we note the characteristic 1/f^2 slope of timing or phase fluctuations, which is due to white noise.

$$S_{\Delta t}(s \to 2\pi f) = \frac{0.529}{(2\pi f)^2} \frac{hvg\, \tau_{FWHM}^2}{T_R E_P} \tag{4.25}$$

Photonic analog to digital conversion and low-noise microwave signal generation generally require a high-frequency signal, typically 10 GHz. Although (4.23) predicts that the jitter decreases as the repetition rate decreases (T_R grows larger), this effect is merely the

consequence of the fact that the pulse goes around the ring fewer times per second. In other words, less noise is added per second if the pulse passes through the amplifier fewer times per second.

The phase noise is proportional to the timing jitter according to the relation (4.26), where f_s is the microwave frequency of interest. Therefore, decreasing the pulse width has the most impact toward reducing the phase noise. In theory, decreasing the repetition rate has the same effect as increasing the pulse energy. However, in reality, as the repetition rate is decreased, it becomes more and more difficult to extract a clean signal at f_s.

$$\begin{aligned}\sigma_{\Delta\varphi}(t_0) &= 2\pi f_s \sigma_{\Delta t} \\ &= 2\pi f_s \sqrt{0.529}\sqrt{\frac{h\nu g t_0}{E_P T_R}}\tau_{FWHM}\end{aligned} \tag{4.26}$$

4.2.3 Simplified Analytical Jitter Model

Although it is instructive to derive the timing jitter and phase noise for an ultrafast laser from the fundamentals, it is interesting to have a still simpler model that provides additional perspective. For experimental purposes, one would like to understand precisely what the shape of the jitter spectral density should be. In this respect, it is helpful to think of the ultrafast laser as a discrete system, radiating a periodic train of impulse functions [65]. The precise timing of these impulse functions will, of course, have some jitter. In essence, the timing jitter can be accurately modeled by a simple, discrete, finite difference equation, (4.29). The timing uncertainty of the pulses can be thought to undergo a random walk driven by a white noise process. This white noise process results from spontaneous emission due to the gain compensating the cavity roundtrip losses and vacuum fluctuations entering the cavity [65].

In this spirit, consider a finite difference equation whereby the timing of the next pulse emitted by the laser is the same as the timing of the previous pulse, plus some

additive noise, F[n] (4.27). The finite difference equation can be solved by transforming into the frequency domain with the z-transform, yielding (4.28). Finally, by recognizing that the z parameter is simply a complex exponential, the power spectral density of the solution can be computed, as in (4.28). Notice, the sampling frequency of the z-transfrom, $\Omega = \omega T_R$ since the ultrafast laser is in essence a periodic impulse train with a Nyquist frequency of $\omega_n = \pi/T_R$. Since we take the additive noise to be white, F(z) is simply given by a constant magnitude, σ_t. This magnitude represents the timing jitter imparted to the pulse from the amplifier by a single pass.

$$t[n] = t[n-1] + F[n] \tag{4.27}$$

$$T(z) = F(z)\frac{1}{1-z^{-1}}$$
$$\left|T\left(z \to e^{j\Omega}; \Omega \to \omega T_R\right)\right|^2 = \frac{1}{2}\frac{\left|F\left(e^{j\Omega}\right)\right|^2}{1-\cos(\omega T_R)} \tag{4.28}$$

$$S_{\Delta t}(f) = \frac{\sigma_t^2}{2\left(1-\cos\left(2\pi T_R f\right)\right)} \tag{4.29}$$

FIG. 37 shows the predicted jitter spectral density for an 80 MHz laser along with a $1/f^2$ slope. The jitter density declines until reaching the Nyquist frequency, and then rises to a singularity at the repetition rate, as well as at DC.

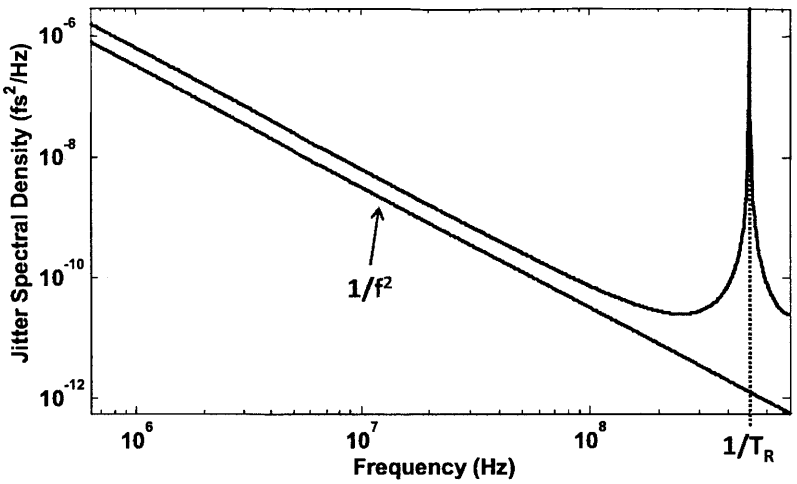

FIG. 37. Power spectral density (in fs^2/Hz) of finite difference quantum noise model. Notice, the density reaches a minimum at the Nyquist frequency (half the repetition rate) and reaches singularity at the repetition rate ($1/T_R$). Below the Nyquist frequency, we expect a slope of $1/f^2$, or two decades per decade. This matches precisely with the analytical PSD in (4.29). For this example, $\sigma^2_t = 3 \cdot 10^{-11}\ fs^2/Hz$.

For the finite difference model, T_R is the repetition rate and σ_t, with units of fs/√Hz, is the additional timing jitter imparted in a single roundtrip. This value is therefore proportional to the minimum jitter spectral density at $f_{rep}/2$.

For comparison, FIG. 41 in the next section also shows the theoretical timing jitter density as expected from the finite difference model. It should be noted, that while this model predicts that the jitter grows without bound, resulting in a singularity at frequencies that are multiples of the repetition rate, in practice this does not occur because the measurement time is finite [66] and the repetition rates are phase locked with a low-bandwidth loop below 3 kHz. Therefore, the jitter spectral density rolls over at 3 kHz and rapidly decreases at low frequencies, for real measurements as in FIG. 41. Moreover, the characteristic shape of timing jitter fluctuations due to white noise is a slope of -20dB/decade, flattening out at the Nyquist frequency, and peaking at the repetition rate. It can be seen from FIG. 41 that the measured slope agrees exactly with this basic model.

4.3 Calibration of the Balanced Optical Cross-correlator

To measure the timing jitter between two lasers, the calibration of the balanced optical cross-correlator must first be performed. In contrast to calibrating the timing link, calibration of the BOC between two laser pulse trains is simpler, but more subtle. For the timing link, the motor or piezo can be varied a known distance to map out the cross-correlation verses time delay. In other words, sweeping the pulses through a mechanical delay can directly produce the cross-correlation verses time delay.

However, when measuring the timing jitter between a pair of lasers, a time delay cannot be used because the pulse timing is completely incoherent between lasers. Fortunately, it is possible to take advantage of this fact to quickly and rapidly calibrate the cross-correlator.

Image a pair of pulse trains with different repetition periods, traveling together in a beam, as in FIG. 38. The observer sits at a fixed point in space, and sees each pair of pulses as they whiz by. Every repetition period, T_R, a new pair of pulses is seen. Since the repetition periods between the pulse trains differs by ΔT_R, they temporally walkoff with respect to each other by another ΔT_R, every T_R. Eventually, they come back into overlap after the beat interval, T_B.

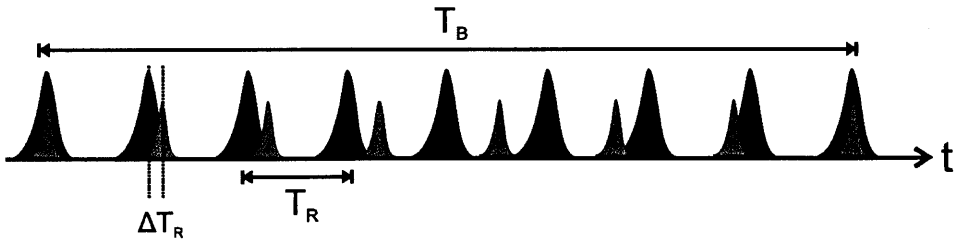

FIG. 38. A diagram of a pair of pulses, with different repetition periods, traveling together in a beam. An observer at a fixed point in space observes pulses every T_R with an offset between them increasing by ΔT_R after every period. The pulses come back into overlap after the beat time, T_B.

The beating interval is given by the difference between the lasers' repetition rates, which is very small.

$$T_B = \left[\frac{1}{f_{R1}} - \frac{1}{f_{R2}}\right]^{-1} = \frac{T_{R1}T_{R2}}{T_{R2} - T_{R1}} \approx \frac{T_R^2}{\Delta T_R} \tag{4.30}$$

As a result of this temporal pulse "sliding", the BOC photodetector sees a cross-correlation every time the pulses collide, every T_B seconds. Thus, an oscilloscope records a cross-correlation, as in FIG. 39. On the oscilloscope, one can measure the slope of the cross-correlation at the zero crossing point, in volts per second or $\Delta V/\Delta T$. However, the next challenge is to convert this measured slope to the actual cross-correlator sensitivity.

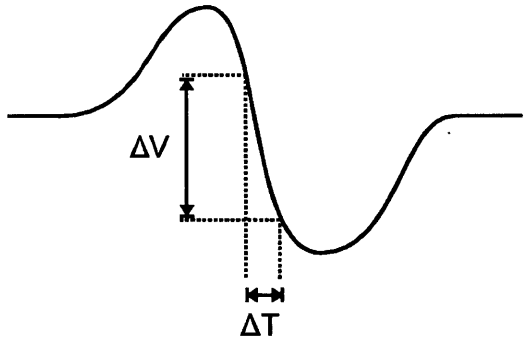

FIG. 39. The balanced optical cross-correlation that is measured with an oscilloscope between a pair of repetition rate detuned ultrafast lasers. Every T_B seconds, the pulses collide and produce this cross-correlation on the photodetectors.

To convert the slope measured on the oscilloscope to the actual BOC sensitivity, recognize that every time a new pair of pulses is emitted from the lasers, their temporal separation increases by $\Delta T_R = T_{R1} - T_{R2}$. Therefore, in a given number of seconds ΔT, we can compute the number of periods T_R that transpire, and deduce how far the pulses have been offset over ΔT seconds. In other words, the pulse offset time, T_{OS}, after ΔT seconds is given by (4.31).

$$T_{OS} = \frac{\Delta T}{T_R} \Delta T_R \tag{4.31}$$

Therefore, the conversion factor from the slope measured on the oscilloscope, ΔV/ΔT, to the BOC sensitivity, K, is given by (4.32).

$$K = \frac{\Delta V}{\Delta T}\left[\frac{\Delta T}{T_{OS}}\right] = \frac{\Delta V}{\Delta T}\left[\frac{T_R}{\Delta T_R}\right] = \frac{\Delta V}{\Delta T}\left[\frac{T_R}{T_R^2 / T_B}\right] = \frac{\Delta V}{\Delta T}\frac{T_B}{T_R} \tag{4.32}$$

In practice, the best method for quickly calibrating the BOC is to tune one laser so that the repetition rate almost exactly matches that of the other laser. As a result, the beat time will become very large, or about 10 to 100 ms. Then, the oscilloscope record length (seconds per division) can be increased until three BOC traces are visible, and a single shot can be recorded. The beat times between the three cross-correlations can be measured with the oscilloscope's cursors, and averaged. Then, provided the digital oscilloscope has a large memory, one can zoom in on the center cross-correlation and measure ΔV/ΔT with cursors. Since T_R does not vary much, the average value for both lasers, as measured with a spectrum analyzer, is perfectly suitable. This technique is the most accurate and simplest method for calibrating the BOC sensitivity.

4.4 Measurement of Timing Jitter

To date, jitter measurement methods relying on direct photodetection and microwave components such as mixers, amplifiers and reference oscillators suffer from limited sensitivity [29], [35], [67]. Early attempts based on heterodyne detection against microwave oscillators were not able to measure the quantum noise since they were limited by the noise of the microwave reference oscillator itself. While quantum-limited jitter has been observed out to the Nyquist frequency for actively mode-locked, picosecond semiconductor lasers [68], [69], which have large timing jitter, these technical limitations prevent

observation of the quantum-origin timing jitter beyond a few hundred kilohertz, at best, for femtosecond, passively mode-locked lasers [37], [39], [43], [68–73]. The jitter of femtosecond, passively modelocked lasers is typically two orders of magnitude or more lower, and so a more sensitive technique is necessary to observe the jitter. Fortunately, balanced optical cross-correlation can provide the requisite sensitivity to fully characterize the timing jitter of passively mode-locked, ultrafast waveguide lasers.

Optical techniques for jitter measurement based on interferometric cross-correlation have very limited measurement range (a single optical cycle), and are simultaneously sensitive to the optical phase [73], and as such do not constitute a pure timing jitter measurement. Therefore, these methods can only provide a ceiling for the timing jitter. Since noise below a few kilohertz is often dominated by classical or external noise sources such as vibrations and pump intensity noise, it has not been possible to clearly observe the intrinsic timing jitter of passively mode-locked, femtosecond lasers at high enough frequencies and over a sufficiently large bandwidth to make a complete comparison with theory. Also, it has not been proven experimentally if the jitter continues to decline at the theoretical rate of -20dB/decade, or if the noise spectrum declines more slowly, or shows other unexpected features.

However, a measurement of the timing jitter is presented for a 79.4 MHz, dispersion managed (stretched pulse), femtosecond erbium fiber laser with unprecedented resolution that enables quantum-limited timing jitter measurements up to the Nyquist frequency, or half the repetition rate. To the author's knowledge, this is the first complete characterization of the timing jitter of a pulse train from an ultrafast, passively mode-locked laser. To achieve this observation, balanced optical cross-correlation (BOC) with a single, periodically poled, KTP crystal (PPKTP), as demonstrated in [36], is used. This technique provides direct measurement of the timing jitter with attosecond resolution, while remaining amplitude insensitive. Moreover, BOC provides a sufficiently large temporal measurement range, on the level of the pulse width. Also, since the detection is done

directly in the optical domain without the use of any microwave electronics, the aforementioned limitations of microwave techniques are avoided [35].

4.5 Experimental Technique

The measurement achieves attosecond resolution with cross-correlation directly in the optical domain, between the outputs of a pair of similar fiber lasers. These fiber lasers are assumed to have similar noise properties, and are shown in FIG. 40. In order to keep the pulses in the linear, balanced measurement range of the BOC, a low-bandwidth, repetition rate phase-lock between the lasers is implemented. Instead, the repetition rate is directly locked in the optical domain without reliance on direct photodetection with microwave electronics, as was previously done [35]. This assures that the measurement is uncorrupted by the noise and drift of the feedback from the photodetection and microwave electronics. Thus, the pulses remain much more tightly synchronized, which allows the measurement of shorter pulses that are more tightly held within the linear, balanced region of the BOC. Therefore, efficiency can be much higher, in turn providing much greater measurement sensitivity. The sensitivity of the BOC is further increased, by using the full output power from both lasers.

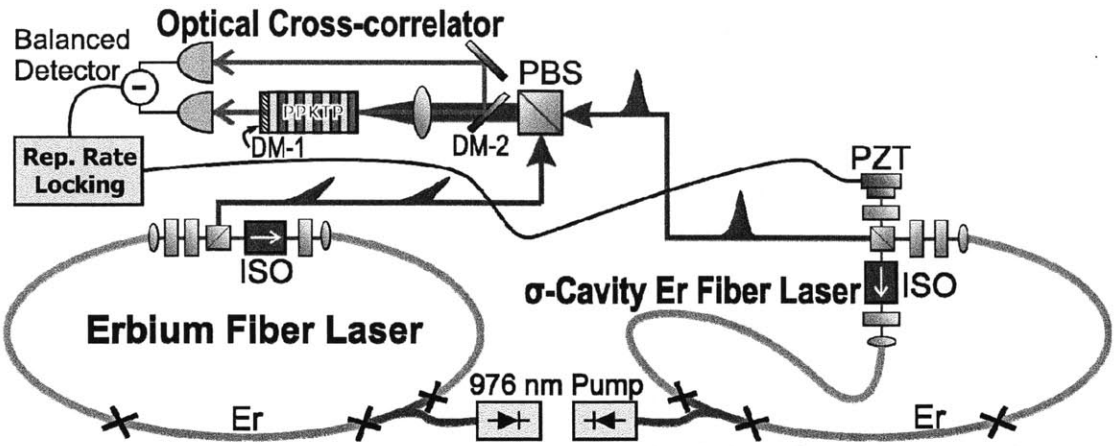

FIG. 40. Schematic of the timing jitter measurement based on balanced optical cross-correlation (BOC) with a periodically poled KTP (PPKTP) crystal. The repetition rates of a pair of similar ultrafast lasers are tightly locked with a kilohertz feedback loop via direct optical detection of the signal from the BOC. The jitter beyond the loop bandwidth, known as the out-of-loop timing jitter, is measured at the BOC, and reveals the timing jitter between the two lasers. DM-1, dichroic mirror coating (T: 775 nm, R: 1550 nm); DM-2, dichroic mirror (T: 1550 nm, R: 775 nm); Er, erbium doped fiber; ISO, Faraday isolator; PBS, polarizing beam splitter; PZT, piezo mirror actuator.

A pair of nearly identical, 79.4 MHz stretched pulse fiber lasers were constructed from normal dispersion, erbium doped fiber (Liekki Er80-4/125) and standard single-mode fiber (SMF-28), such that the roundtrip group delay dispersion is close to zero [74]. The lasers are passively mode-locked using the principle of additive pulse mode-locking with free space waveplates and polarizing beam splitter [53]. In addition, they are optically pumped at 976 nm with low-noise, fiber Bragg grating stabilized telecom pump diodes. The optical bandwidth directly from the oscillators is 79 nm. Both lasers generate about 35 mW of optical power corresponding to a pulse energy of about 450 pJ.

4.6 Stretched Pulse Fiber Laser Jitter Measurements

As shown in FIG. 41, the measured integrated timing jitter for these lasers is 2.6 fs from the Nyquist frequency, 39.7 MHz, to 10 kHz. Note, this number represents the actual measured noise divided by a factor of √2, which expresses the equivalent noise for a single laser. The Si balanced detector used for the measurement is a Thorlabs PDB150A, with an RF

bandwidth of 50 MHz at a gain of 10^4 V/A (−3dB). As is shown in FIG. 41, the measurement extends to 40 MHz without being limited by either shot noise, the electronic noise of the Tektronix RSA3000 spectrum analyzer used to acquire the data, nor from the noise of the amplified photodetector.

$$S_{\Delta t}(f) = \frac{\sigma_t^2}{2\left(1-\cos\left(2\pi T_R f\right)\right)} \tag{4.33}$$

The measured jitter is compared against the simple, finite difference model which was presented in the previous section, (4.33). We may arrive at a theoretical value for σ_t by considering the theory by Namiki and Haus [66] for the timing jitter of a stretched pulse laser. The following typical values for the stretched pulse fiber laser are used, as described in [75]: a reference pulse width, τ_0, of 50 fs, a saturated gain, g, of 0.8, a gain bandwidth, Ω_g, of 40 nm, and a saturable absorption coefficient, α, of 0.2. Also, we estimate an excess noise factor, Θ, for this non-optimal erbium doped amplifier of 10, and an intracavity pulse energy, w, of 550 pJ—assuming a typical output coupling of 50% and an additional intracavity loss of 30% from fiber splices and free space to fiber coupling. Lastly, we estimate a net cavity dispersion, D, of +0.004 ps^2. This theory predicts a jitter corresponding to a value for σ_t of 2×10^{-5} fs/√Hz, as shown in FIG. 41. Note, the Namiki and Haus theory, which is specific to the stretched pulse laser, predicts a timing jitter greater than that caused purely by spontaneous emission acting alone on a transform limited pulse with length τ_0, due to the chirp parameter, β, which increases the timing jitter of stretched pulsed lasers with positive net cavity dispersion [60], [76] [66].

Unexpectedly, relatively broadband noise bumps are observed at a quarter and an eighth of the repetition rate—although they contribute only about 100 as to the total jitter, indicating potential instabilities due to period quadrupling and higher order instabilities. Not surprisingly, the contribution of high frequency noise can be much worse depending on the quality of the mode-locked state, so it is necessary to finely adjust the intracavity waveplates to achieve the lowest noise performance. Nonetheless, these high-frequency features can be important factors, as shown in FIG. 41(b), since it can be seen that they may

contribute as much as 5.5 fs to the timing jitter for non-optimium wave plate settings, i.e. for a non-optimum mode locking state. In this case, it is likely the mode-locking state is on the verge of period doubling instability—although this is not apparent by observing either the RF spectrum from direct photodetection with a RF spectrum analyzer or by observing the optical spectrum on a standard optical spectrum analyzer. Thus, it is indispensible to measure the total integrated jitter up to the Nyquist frequency for a full characterization of the timing jitter, as is widely recognized for harmonically mode-locked lasers [68], [69]. It turns out, this is equally important for passively, fundamentally mode-locked lasers. One cannot simply assume that the 20-db per decade roll-off of the phase noise is automatically a given.

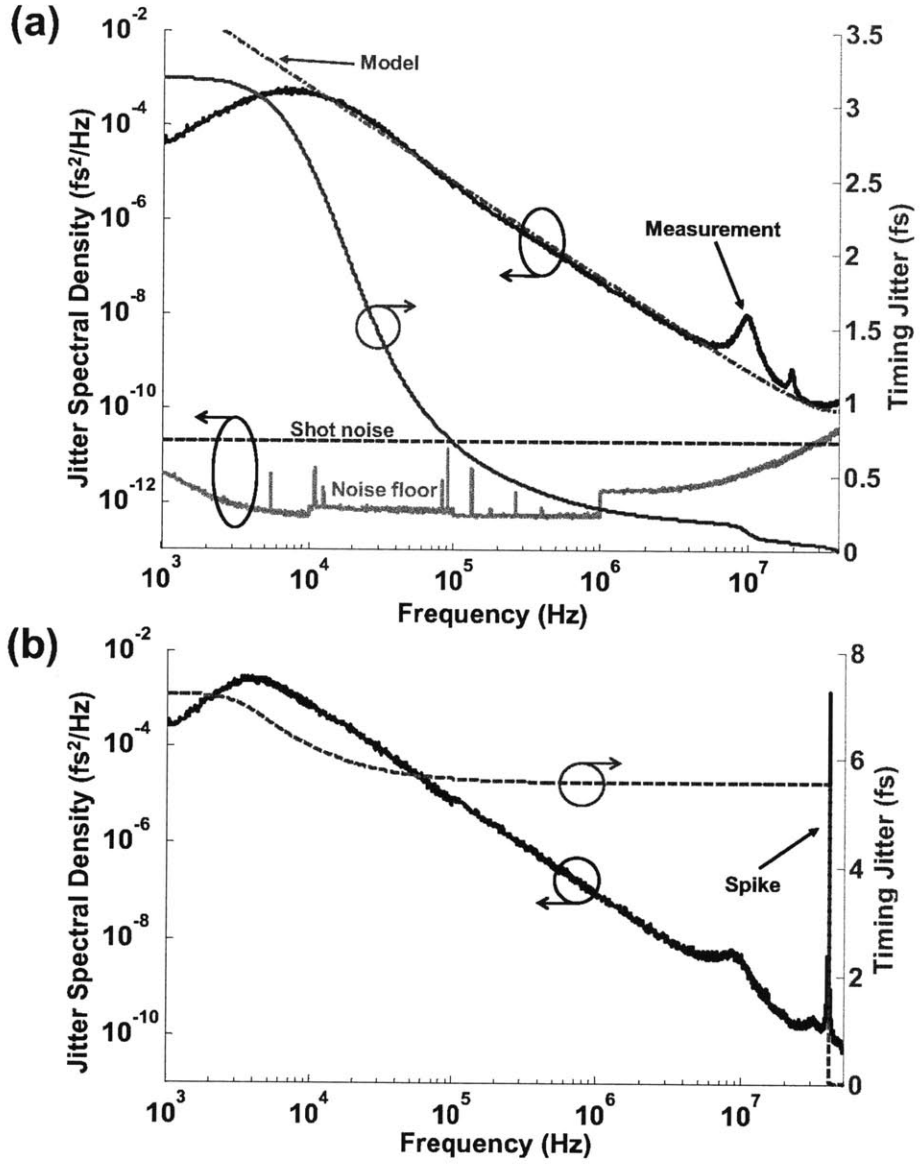

FIG. 41. (a)—(b) are the jitter spectral density for the 79.4 MHz stretched pulse fiber lasers (divided by two for the equivalent noise of a single laser) and the integrated timing jitter (divided by √2). (a) shows the integrated jitter is 2.6 fs [10 kHz, 40 MHz], and only 0.7 fs [100 kHz, 40 MHz]. Also shown are the combined detector and instrument noise floor and the theoretical shot noise. For comparison, the theoretical slope, $1/f^2$, described by Eqn. 1 is shown. Note, the measurement extends to the Nyquist frequency ($f_{rep}/2$) without being limited by the instrument, detector or shot noise. (b) shows the measured jitter, [1 kHz, 50 MHz], for the same lasers in a noisier mode-locked state with a spike at $f_{rep}/2$ contributing 5.5 fs to the jitter.

In summary, the timing jitter of a pair of passively mode-locked, femtosecond erbium fiber lasers has been fully characterized using the single-crystal, balanced optical cross-correlation method—entirely in the optical domain. The improved sensitivity afforded by this technique provides an unprecedented shot noise limited resolution of 2×10^{-11} fs^2/Hz [35]. As a result, we are able to measure the quantum limited timing jitter out to the Nyquist frequency of 39.7 MHz, yielding a total quantum-limited jitter of 2.6 fs rms [10 kHz, 39.7 MHz]. The measurement exactly confirms the noise expected for a random walk process driven by a white noise source of quantum-origin over more than three decades, extending out to the Nyquist frequency. Finally, unexpected contributions to the noise are discovered around $f_{rep}/2$, $f_{rep}/4$ and $f_{rep}/8$, which nominally contribute only ≈100 as to the total jitter, but have been found to be as large as 5.5 fs rms, depending on the mode-locked state.

4.7 Soliton Laser Timing Jitter Measurement

Since the analytical theory of the timing jitter of the soliton laser has been well established, measurement of its timing jitter spectral density is ideal for comparing to theoretically predicted performance. In this way, the theory can provide insight on the inner workings of the laser. For instance, one can estimate the excess noise of the amplifier and the decay time of center frequency fluctuations by comparison of the data with theory. As a result, it is important to also characterize the jitter of soliton lasers as well as possible. Thus, the same method is used to measure the jitter between a pair of soliton lasers as was for the pair of 80 MHz stretched pulse lasers.

For the following measurement, a 200 MHz erbium-doped soliton fiber laser was measured. Total cavity dispersion is estimated at -23,000 fs^2, assuming a cavity length of one meter and a fiber dispersion of -23 ps^2/km (Corning SMF-28). Pulse energy is 700 pJ, assuming 50% output coupling, or 70 mW output power. Pulse duration has been previously characterized for this particular laser [70].

The measurement results are shown in FIG. 42, along with the measured detection noise floor and the calculated shot noise. The shot noise is calculated from the estimated sum frequency power at 780 nm, knowing the sensitivity of the balanced photodetector, and the voltage signal level of the cross-correlation. Thus, the SFG power is estimated to be about 300 mW when locked. The photodetector gain is 10^4 V/A, with a silicon sensitivity of 0.4 A/W, yielding a timing sensitivity of 26.5 mV/fs. By fitting to the data, we are able to measure the excess noise (which simply shifts the PSD vertically) and the center frequency decay time, which sets the breakpoint frequency as the slope transitions to $1/f^4$. To the best of our knowledge, this represents the first direct measurement of these parameters in an ultrafast laser. Precious attempts lacked the required bandwidth to observe the jitter at 20 MHz or beyond, without reaching the noise floor and hiding these effects.

Additional parameters of the soliton laser noise theory can be determined from the measurement. For instance, the center frequency decay time constant τ_p, can be found by carefully observing the jitter spectral density slope at high frequencies. This is done by choosing τ_p so that the break point from $1/f^2$ to $1/f^4$ slope occurs at the proper frequency, so as to fit the data. Lastly, it is still necessary to assume an excess noise Θ of 10 to obtain agreement with the measurement. This final point leads us to the conclusion that the amplifier likely contributes significant excess noise. These parameters are summarized in Table 2.

Parameter	Value	Description
$\hbar\omega_0$	0.8 eV	Photon energy
τ	167 fs FWHM	pulse duration
D	-23,000 fs^2	Total cavity dispersion
T_R	5 ns	Repetition rate
g_s	0.5	Saturated round-trip gain
Θ	10	Excess noise factor
τ_p	17 ns	Decay time of center frequency fluctuations
w_0	700 pJ	Cavity pulse energy

Table 2. Parameters used for modeling the 200 MHz erbium fiber soliton laser.

Interestingly, from these measurements, it is consistently found that the timing jitter is on average an order of magnitude greater than predicted theoretically for soliton lasers. It is not yet known with great certainty if this discrepancy is due mainly to complex pulse formation mechanisms (laser dynamics) or simply to an excessively noisy amplifier [76]. Only recently have experimental studies of the effect of laser dynamics on timing jitter been conducted [77]. However, these studies suggest that laser dynamics may account for a factor of 2—3 in integrated timing jitter at most. Therefore, it is likely the case that timing jitter performance can be further improved by reducing the excess noise of the amplifier.

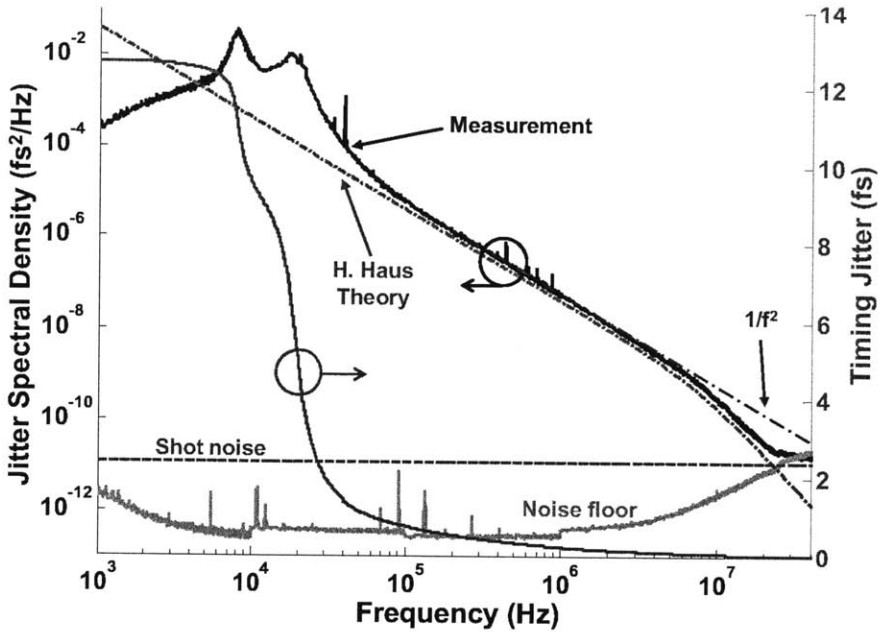

FIG. 42. Measurement of 200 MHz erbium fiber soliton laser with PPKTP balanced optical cross-correlator and 50 MHz bandwidth Thorlabs amplified balanced photodetector. The measurement reaches the calculated shot noise floor at 20 MHz, after transitioning to a $1/f^4$ slope at 8 MHz. The change in slope occurs due to the center frequency decay time (Haus Gordon jitter) parameter, τ_p. To fit the Haus soliton timing jitter model to this measurement, an excess noise factor of 10 is assumed.

Since the analytical model for soliton timing jitter is well documented in the literature, we briefly note the principle features [78]. First, the magnitude of the PSD is shifted up by the pulse width, gain, pulse energy and excess noise, as expected from the basic theory. This corresponds to the "1" term in (4.34). An additional jitter, known as the Gordon-Haus jitter, is caused by the total cavity dispersion. The origin of this jitter is the conversion of center frequency fluctuations to group velocity changes, due to the group velocity dispersion of the fiber. These fluctuations decay back to the fixed center frequency with a decay constant τ_p. As a result, the PSD slope transitions from $1/f^2$ to $1/f^4$, until reaching the shot noise limit. By observing this break frequency, $1/\tau_p$, the center frequency fluctuation decay time can be estimated.

$$S_{\Delta t}(f)^2 = \left(\frac{\tau}{2\pi f}\right)^2 \frac{\Theta g_s \hbar\omega_0}{6T_R w_0}\left(1+\frac{4}{\pi^2}\frac{4|D|^2}{\tau^4 T_R}\frac{1}{1/\tau_p+(2\pi f)^2}\right) \tag{4.34}$$

5 Coherent synthesis of independent ultrafast lasers for short pulse generation

Coherent pulse synthesis from uncorrelated laser sources has been actively pursued to generate higher energy radiation or shorter duration pulses [13], [32]. Due to the expense and limitations of scaling laser energy, beam combining has been an attractive method for scaling continuous wave laser power [79]. However, beam combining of disparate pulsed laser sources with different center wavelengths permits the synthesis of a broader optical spectrum. In this way, shorter duration pulses can be synthesized without placing excessive demands on the individual sources.

However, the coherent synthesis of ultrafast sources is considerably more challenging than continuous wave laser beam combining. For ultrafast sources, there are two dimensions requiring precise synchronization: pulse envelope timing and carrier wave phase. In contrast, CW sources require only the synchronization of the carrier waves. The control of both carrier wave and pulse envelope is made difficult by the need for simultaneous, orthogonal control of both parameters with high speed.

For ultrafast pulse generation, the limited gain bandwidth of any ultrafast laser places a lower limit on the attainable pulse duration. By improving the bandwidth of the oscillator, the radiated spectra can be compressed to a shorter duration pulse. One common technique for increasing the spectral emission of ultrafast lasers is to perform nonlinear spectral generation either internally or externally to the laser oscillator. This

technique has been widely employed to generate 5 fs pulses at 800 nm with Ti:Sapphire lasers [80], [81] by way of self-phase modulation in the Ti:Sapphire crystal. However, the self-focusing effects which accompany the non-linear spectral generation degrade the beam quality of few-cycle Ti:Sapphire lasers. As the nonlinear spectral generation is driven harder, beam quality further degrades [82]. Moreover, mode locking becomes more unstable and crystal damage can occur [83].

Other techniques toward short pulse generation have focused on non-linear spectral generation with high energy optical parametric amplifier systems driven by a Ti:Sapphire oscillator. In this way, the spectrum from a single Ti:Sapphire laser can be shifted to a long wavelength portion, amplified and broadened, and then recombined with the short wave portion. In contrast to synchronizing independent lasers, the "master oscillator, multiple amplifier", or MOMA, technique supplants the need for complex locking electronics because most noise is common mode to the oscillator [12], [18], [19], [34].

On the other hand, there are advantages to the coherent synthesis of independent oscillators. High repetition rate pulse synthesis, as has been shown with supercontinuum generation in fiber, is not easily scalable in pulse energy because the non-linear process tends to clamp the pulse energy of the supercontinuum [18].

Attempts at coherent synthesis of a Ti:Sapphire laser with a Cr:Forsterite laser, which lead to the work presented in this thesis, was unsuccessful, in large part, because a technique for high speed, orthogonal control of pulse timing and carrier envelope phase had not been developed. As an additional complication, the Cr:Forsterite laser, in the 30 fs regime, was reported to be unreliable and suffer from sensitivity to thermal effects in the laser crystal. Without reliable sources, tackling the formidable challenges involved in laser synchronization is extremely difficult [5], [13].

However, as an investigation into laser synchronization and high-speed, attosecond precision timing and phase control, coherent synthesis of independent lasers can provide

great insight. High repetition rate, high pulse energy sources can be actively synchronized without limitation by non-linear processes. Moreover, many of the techniques developed for coherent synthesis solve challenges in related areas. For instance, gigahertz, fiber supercontinuum-based frequency combs pumped by waveguide ultrafast lasers can benefit from the high-speed, extra-cavity carrier envelope phase (CEP) locking method. In addition, non-linear shifting techniques, such as the Raman self-frequency shift, can introduce considerable timing jitter. This phenomenon is due to the intensity to center frequency shift coupling, which in turn couples to the group velocity of the Raman soliton. Thus, it is desirable to maintain high-speed synchronization between the Raman soliton and the pump pulses. Therefore, the high-speed, attosecond precision pulse timing locking techniques developed in this thesis can provide a solution.

5.1 Approaches to Pulse Synthesis

Coherent synthesis of ultrafast pulse trains has a rich and interesting history over the past decade. There are essentially three main schemes for synthesizing ultrafast pulses, plus an additional hybrid scheme. From a control theory perspective, these schemes different in the degree of active synchronization required—and span the entire gamut from requiring no active synchronization to complete synchronization of both CEP and pulse timing.

The most electronically simple approach for pulse synthesis is to synthesize pulses from a single ultrafast laser by splitting the output and generating additional spectrum. In this way, nearly all of the noise, except slow drift, is common to both pulses. For long term stable performance, only a slow feedback loop for pulse timing is required to combat thermal drifts. As described by FIG. 43, the pulses are generally split, separately amplified and shifted in wavelength by a nonlinear process. This nonlinear process may be accomplished by an optical parametric amplifier (OPA) or a highly nonlinear fiber (HNLF) [12], [19].

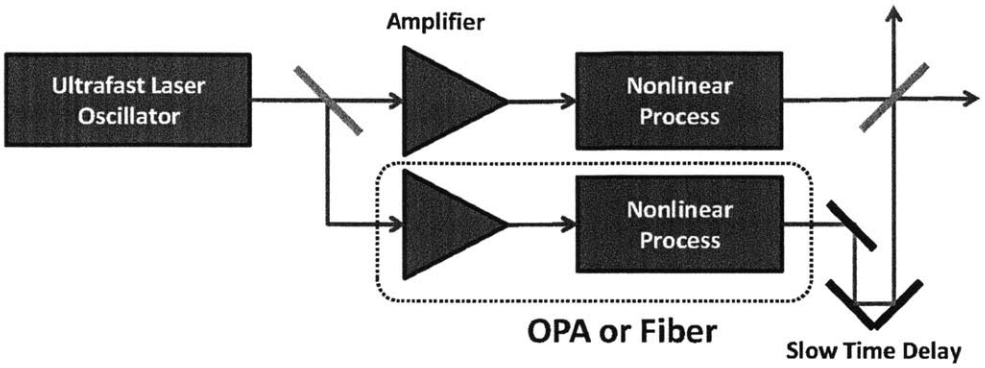

FIG. 43. A single-oscillator pulse synthesis scheme with only amplifiers and nonlinear spectral generation requires the least electronic synchronization complexity. Only a slow time delay feedback is needed to counteract drift, since CEP and timing coherent is preserved.

Typically, the nonlinear process in the aforementioned scheme places severe limitations on the repetition rate or pulse energy which can be synthesized. As a hybrid approach with greater flexibility, a laser can be synchronized to an optical parametric oscillator (OPO), as in FIG. 44 [20–22]. Since the OPO is pumped by the laser pulses, pulse timing synchronization is automatically achieved in a passive, optical fashion. However, CEP is not preserved in an OPO since additional phase slip is present in the OPO cavity, and oscillations may anyway build up from noise. In this approach, it is only necessary to detect the CEP between the laser and OPO, and to correct for the CEP of the OPO with active feedback. With only a single feedback loop, orthogonal control between timing and CEP is not required—greatly simplifying the entire scheme.

It should be mentioned that a similar hybrid scheme is also possible with two ultrafast lasers. Passive, optical timing synchronization between a Ti:Sapphire laser and a Cr:Forsterite laser has been demonstrated with composite laser cavities. In this way, only CEP feedback is needed, as with the OPO method [84], [85].

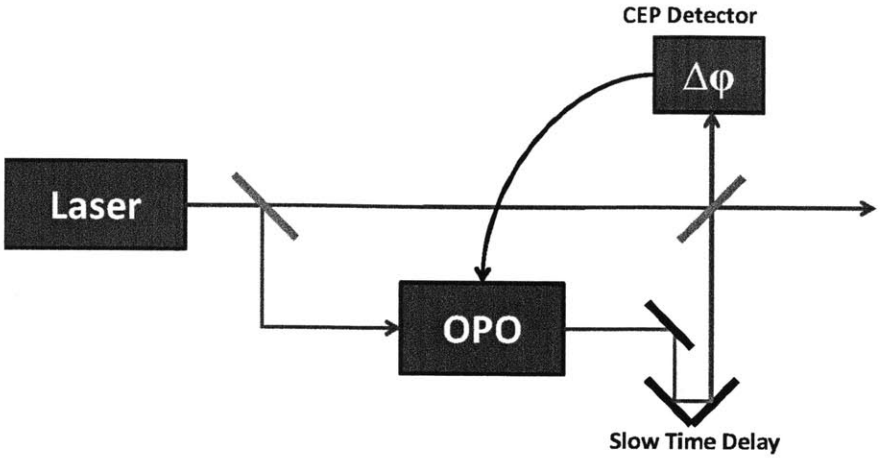

FIG. 44. Hybrid approach to pulse synthesis, whereby an optical parametric oscillator (OPO) is pumped by a laser oscillator. The pulse timing of the OPO is automatically locked to the pump laser. Only a CEP lock is required, and so orthogonality between pulse timing and CEP is not a concern.

The most electronically complex, but general, means of coherently synthesizing ultrafast pulses is to combine two entirely independent ultrafast lasers, as in FIG. 45. Since both the CEP and pulse timing of both lasers is entirely independent, high-speed, orthogonal active synchronization of pulse timing and CEP must be achieved between the lasers.

Prior work toward this scheme has been limited due to the extreme demands of performance necessary for long-term stable, sub-cycle synchronization. Attempts to coherently combine totally independent lasers for pulse synthesis have been limited to synchronizing slightly wavelength detuned, 20 fs Ti:Sapphire oscillators [23]. The work achieved 5 fs timing jitter within a bandwidth of only 160 Hz. Furthermore, phase coherence was observed only at time scales up to 20 ms. Phase stabilization was achieved with a very slow, swiveling end mirror in a prism-based Ti:Sapphire to tune the carrier envelope phase. Other work did not demonstrate phase coherence, but rather broadband frequency comb synthesis with low frequency error between lasers [86]. In essence, without balanced

optical-cross correlation and high-speed, orthogonal actuators, long-term, sub-cycle active synchronization cannot be achieved.

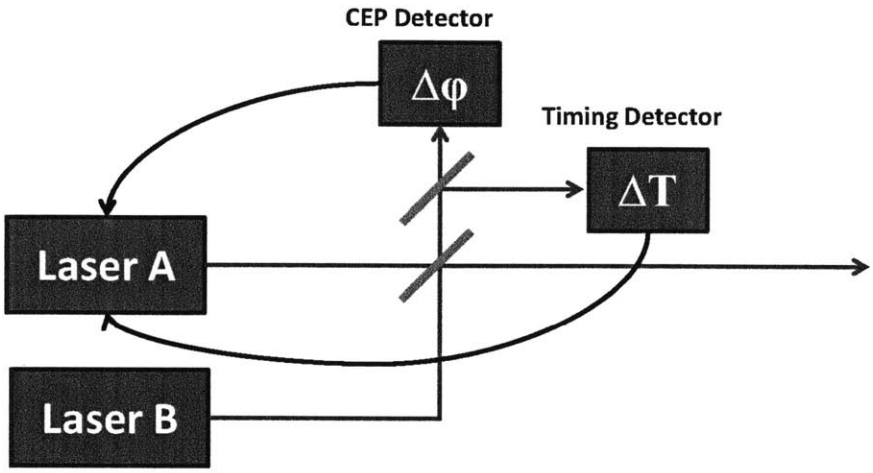

FIG. 45. The synchronization of completely independent ultrafast lasers requires high-speed detection and orthogonal control of both pulse timing and CEP. Two high-performance feedback loops must be simultaneously engaged, and so this scheme has the most electronic complexity.

In this chapter, work enabling the sub-cycle precision, long-term stable coherent synthesis of independent, <10 fs ultrafast sources is presented. The method leverages balanced optical-cross correlation to achieve attosecond precision control of pulse envelope timing with long-term stability [13], [29], [32], [35]. High speed CEP stabilization without corruption of pulse timing is achieved by incorporating an acouto-optic frequency shifter in a fiber supercontinuum in a feedback configuration. Reduction of timing jitter well below the femtosecond level is further demonstrated by feedback upon a high speed, waveguide phase shifter in the fiber supercontinuum system. Additionally, these techniques are effectively used to control the pulse timing and CEP of an octave spanning supercontinuum with sub-cycle precision, without degrading the optical bandwidth or beam quality.

5.2 Principles of Frequency Comb Synthesis

The output of an ultrafast laser can be thought of as a frequency comb in the frequency domain, as in FIG. 46. In the time domain this corresponds to the periodic emission of ultrafast pulses at the repetition rate f_R. The laser radiates at a center wavelength, of carrier frequency, much like how an AM radio broadcasts at a central carrier frequency. For this reason, the frequency comb is defined not only by the repetition frequency, but also the phase and frequency of the carrier offset, f_{CEO}. Therefore, the frequency comb is uniquely defined by these two parameters. The repetition frequency sets the spacing of the comb, while the carrier offset, f_{CEO}, sets the shift of the entire comb. As can be seen in the figure, since the comb is periodic, an f_{CEO} shift of f_R returns the comb to an identical state, albeit with a carrier frequency shift. This corresponds to a carrier envelope phase shift of 2π per pulse in the time domain [87].

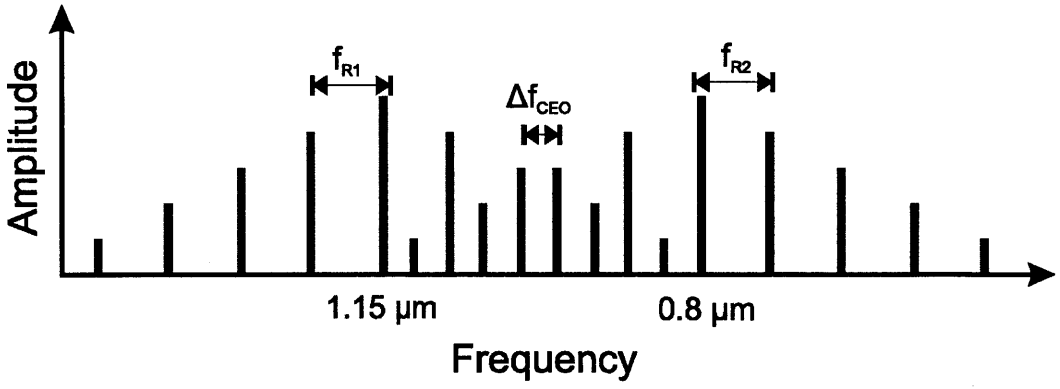

FIG. 46. Frequency comb of two laser spectra, characterized by the repetition frequency of both combs and the difference in carrier envelope offset frequency.

To coherently combine two frequency combs to synthesize a broader spectrum, it is necessary to lock the timing of the repetition rate and the carrier envelope, with zero offset.

The equivalent time domain picture for frequency comb synthesis is shown in FIG. 47. In the time domain, both laser pulses may be separated by some time offset, ΔT. In addition, the carrier wave may have a phase offset, $\Delta\phi_{CEO}$. Provided these parameters are locked to zero, constructive interference results, producing a broader spectrum and shorter pulse. If this spectrum is broad enough, the resulting pulse intensity can be as short as a single optical cycle at the carrier frequency, or center wavelength. At a center wavelength of 1000 nm, a single cycle of the carrier wave is only 3.3 fs in duration.

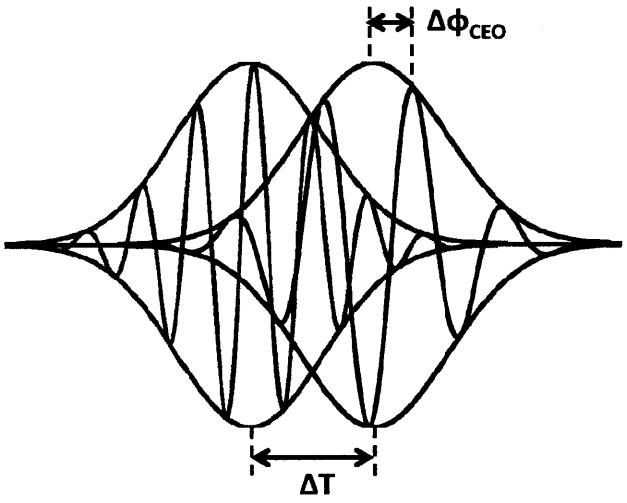

FIG. 47. Equivalent time-domain picture of frequency comb synthesis. In the time domain, the red and black pulses may be separated by some time offset, ΔT. In addition, the carrier wave may have a phase offset, $\Delta\phi_{CEO}$. Both parameters must be locked to zero offset for proper frequency comb synthesis.

Pulse timing coupling to repetition rate remained the major roadblock toward successful single cycle synthesis with independent lasers [88]. Modulating the pump power also shifts the group velocity of pulses in the laser cavity by changing the pulse energy [25]. Indeed, this effect was noted in earlier attempts at laser synchronization with longer pulse lasers [23]. As an alternative to pump power modulation, tilting of the cavity end mirror in a Ti:Sapphire with dispersion compensating prisms in the cavity provided a possible solution.

However, mechanical tilting is quite slow. The method also requires a prism based Ti:Sapphire laser, which is less mechanically robust and produces longer pulses than the modern Double Chirped Mirror design.

Synchronizing a fiber supercontinuum, instead of a Cr:Forsterite laser, to a Ti:Sapphire laser has many benefits. For instance, the telecommunications fiber Bragg stabilized pump diodes available for such erbium fiber lasers are known to be relatively low noise and low cost. But perhaps more importantly, with fiber technology, one can exploit a range of techniques and telecommunications technology. This permits far better synchronization. For instance, because the fiber supercontinuum source is constructed in stages, with each stage increasing bandwidth or optical power, faster actuators can be situated earlier in the chain, where optical bandwidth and power is at a minimum. If the oscillator directly outputs a high power, broad bandwidth free space beam, high speed telecom devices, such as acouto-optic frequency shifters and waveguide phase shifters cannot be readily incorporated. Instead, a single mode fiber laser at 1550 nm benefits from the availability of high-speed, waveguide phase shifters, small piezoelectric mirrors and fast acousto-optic frequency shifters. Moreover, since these actuators are placed before the laser bandwidth is broadened into a supercontinuum, the high-speed actuators need not perform over a very broad bandwidth without either spectral filtering or degrading the spatial quality.

5.3 System Description

The laser synchronization system consists of a fiber supercontinuum source pumped by a passively mode-locked erbium fiber laser, which is locked to a broadband Ti:Sapphire laser. The Ti:Sapphire laser is of a recent design, as pictured in FIG. 49 [83]. It uses all dielectric, double-chirped, dispersion compensating mirrors to compensate cavity dispersion for short pulse generation [89]. Also, it uses the inverse gain output coupler to improve laser stability

by compensating for the limited gain bandwidth. This is accomplished by providing less output coupling at the wings of the spectrum. In this way, mode-locking can be achieved with less non-linearity [90]. The Ti:Sapphire is not configured to achieve octave spanning bandwidth, and is not run near the stability limit of mode-locking.

The spectra of both the supercontinuum and the Ti:Sapphire lasers are shown in FIG. 48 on a linear scale. The Ti:Sapphire laser spans 700 to 950 nm, while the fiber supercontinuum spans 950 nm to 1400 nm. Although the supercontinuum is exceptionally flat, the compression of such a broad bandwidth is challenging with a prism compressor. With F2 prisms, only the portion below 1200 nm is well compressed. The Ti:Sapphire laser, however, benefits from the availability of double chirped mirrors. In this case, three 7^{th} generation DCM mirror pairs are used to compress the Ti:Sapphire pulse at the system output to 7 to 8 fs, depending on the exact mode-locking state.

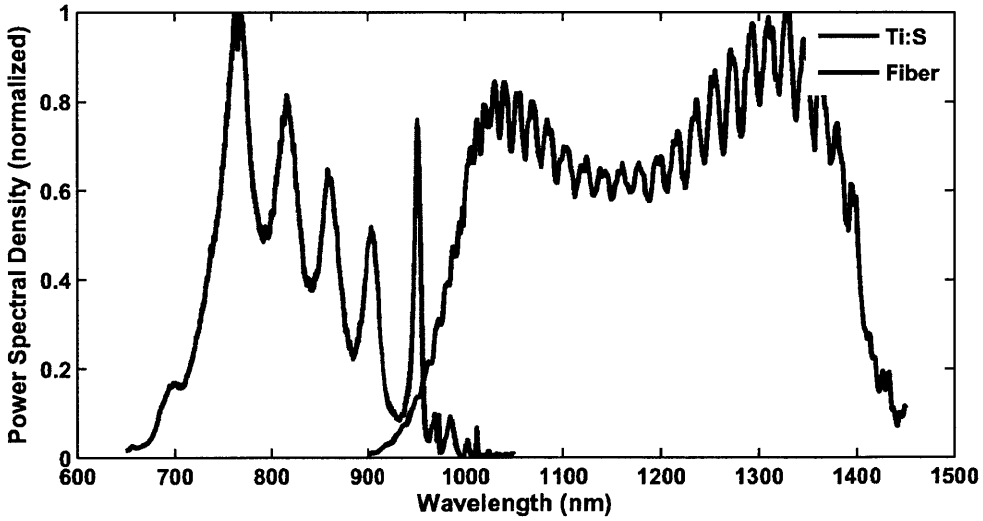

FIG. 48. Combined spectra of Ti:S laser and fiber laser supercontinuum source on a linear, normalized scale.

The fiber supercontinuum system, shown in the upper portion of FIG. 51, consists of three main stages with dispersion compensating optics in between. The erbium fiber amplifier (EDFA) is seeded by an additive pulse mode-locked erbium fiber laser with a repetition rate of 78.4 MHz and an optical bandwidth of roughly 60 nm [53], [91]. It produces about 25 mW average power, or a pulse energy of 300 pJ. The pulses out of the oscillator are amplified to about 5 nJ by an EDFA, yielding an average power of about 390 mW. Next, the amplified pulses are compressed with a pair of silicon, Brewster angle cut prisms to 63 fs. The measured and retrieved pulses are shown by the second harmonic Frequency Resolved Optical Gating (FROG) method in FIG. 52. To obtain symmetric FROG traces over broad bandwidths, the FROG was built with a Mach-Zehnder geometry and broad-band dielectric beam splitters coated on a 1 mm fused silica substrate [5], [92], [93].

Note, it is not expected that FROG can easily retrieve few-cycle pulses due to several issues. First, SHG FROG needs efficient phase matching across the entire optical bandwidth. Even with 10 μm Type-I BBO, conversion efficiency is not particularly flat from 650 nm to 1400 nm. More significantly, it is exceptionally difficult to couple in the entire SFG signal from 325 to 700 nm to the grating spectrometer without spatial filtering. Also, since the optical bandwidth exceeds an octave, it is difficult to filter out the fundamental spectrum with SHG FROG. Finally, SHG FROG pulse retrieval depends on the successful convergence of an iterative algorithm under non-ideal conditions of noise and spectrogram distortion. As such, convergence can often fail for complicated spectra. For these reasons, a two-dimensional spectrum shearing interferometer (2DSI) is implemented for characterization of the combined spectrum with greater simplicity, accuracy and confidence.

After amplification and compression, the pulses are sent into a fiber assembly developed by the Leitenstorfer group at the University of Konstanz [18]. It consists of a two-part assembly of Corning SMF-28e fiber spliced to a few millimeters of a small core, germanium doped, highly-nonlinear fiber (HNLF). First, approximately 40 mm of SMF-28e performs soliton compression of the pulse to about 30 fs. The pulse then enters the HNLF, where it

generates dispersive and soliton pulses due to four wave mixing. The anomalous dispersion pulse is down-shifted to longer wavelengths. The dispersive pulse is generated by the Cherenkov radiation, which produces a pulse at shorter wavelengths [94]. The dispersion of the HNLF is tailored such that the group velocity dispersion is zero at about 1400 nm. In this way, the group velocity of both short wave and long wave portions of the supercontinuum propagate at the same group velocity, dramatically enhancing the efficiency of the supercontinuum process. Remarkably, the dispersive pulse spectrum can be made nearly completely flat from 1000 nm to 1400 nm, and retains a well-behaved, parabolic phase that can be compressed with common prism materials.

After supercontinuum generation, the output from the high numerical index (NA = 0.35) fiber is collimated with a chromatically invariant gold-coated parabolic mirror with an effective focal length of 5 mm. This yields a beam diameter of 2 mm. It is necessary to use a parabolic mirror because for such a high NA and broad spectrum (2000 – 950 nm), a lens or spherical mirror will provide too much spherical or chromatic aberration. Also, the dispersion introduced by the lens is undesirable.

The supercontinuum centered about 1200 nm is then compressed in a pair of F2 equilateral prisms with a separation of 25 cm. At the end of the prism compression, a knife-edge filter has been inserted to eliminate the strong pump at 1550 nm (although this is not necessary). Compression yields a pulse of 8 fs duration, which is slightly above the transform limit of 7 fs. The pulse shape has been verified, also with the FROG technique, as shown in FIG. 53. It can be seen that the spectra at wavelengths greater than roughly 1200 nm are not well compressed, and contribute only a broad pedestal to the pulse.

It is also possible to use other prism materials to compress the supercontinuum. The difference in performance between SF10 and F2 prisms for compressing the supercontinuum can be seen by studying the dispersion slope (TOD) for each prism compressor. FIG. 50 shows the group delay dispersion (GDD) and dispersion slope (TOD) for SF10 and F2 glass prism compressors with apex separation distance of 21 cm and 34.5 cm,

respectively. It can be seen that the TOD is zero at 1150 nm for F2 prisms and 1250 nm for SF10 prisms. Therefore, SF10 prisms more optimally compress the central portion of the supercontinuum, while F2 prisms compress the portion below 1200 nm effectively. Both result in about 8 fs pulse durations, however. In either case, it is not possible to optimally compress the entire supercontinuum. Inserting a deformable mirror in the prism compressor can provide a means of eliminating the residual higher order dispersion.

The beam from the fiber supercontinuum is then combined with the Ti:Sapphire with a ultra-broadband beam splitter with low dispersion, which was previously developed. This beam splitter provides spectrally flat, 50% splitting from 600 nm to 1400 nm.

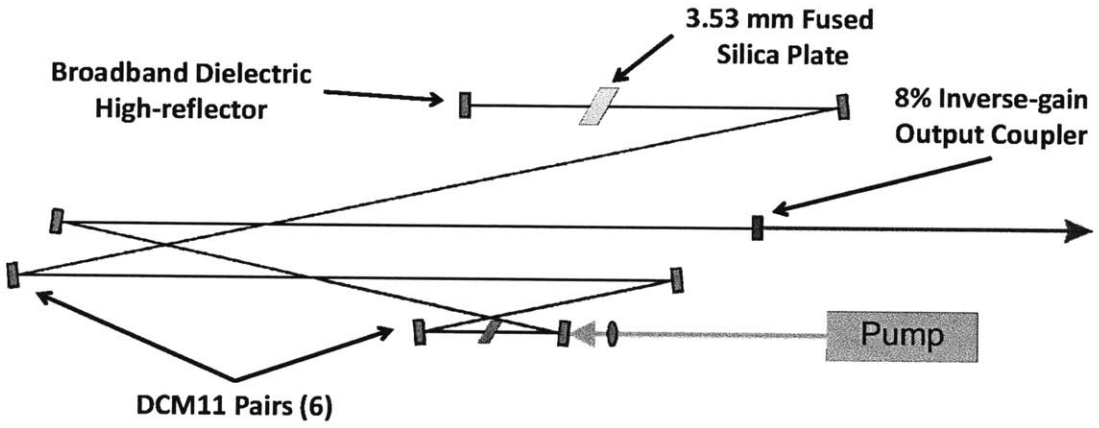

FIG. 49. Schematic of Ti:Sapphire laser with inverse gain output coupler (8%) and 11th generation Double Chirped Mirrors (DCM). Dispersion compensation is provided by 3.53 mm fused silica plate in the long arm. A broadband high reflector end mirror (C5-HR) replaces the lossy silver mirror of previous generations.

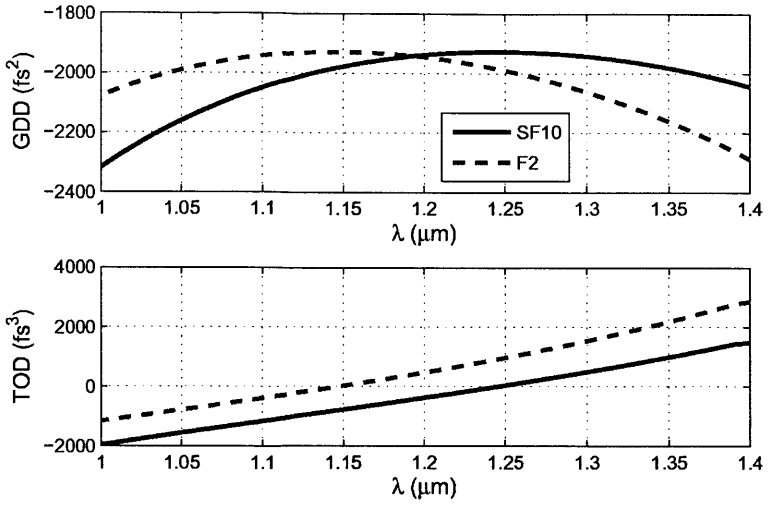

FIG. 50. Group delay dispersion (GDD) and dispersion slope (TOD) for SF10 and F2 glass prism compressors with apex separation distance of 21 cm and 34.5 cm, respectively. It can be seen that the TOD is zero at 1150 nm for F2 prisms and 1250 nm for SF10 prisms. Therefore, SF10 prisms more optimally compress the central portion of the supercontinuum, while F2 prisms compress the portion below 1200 nm effectively.

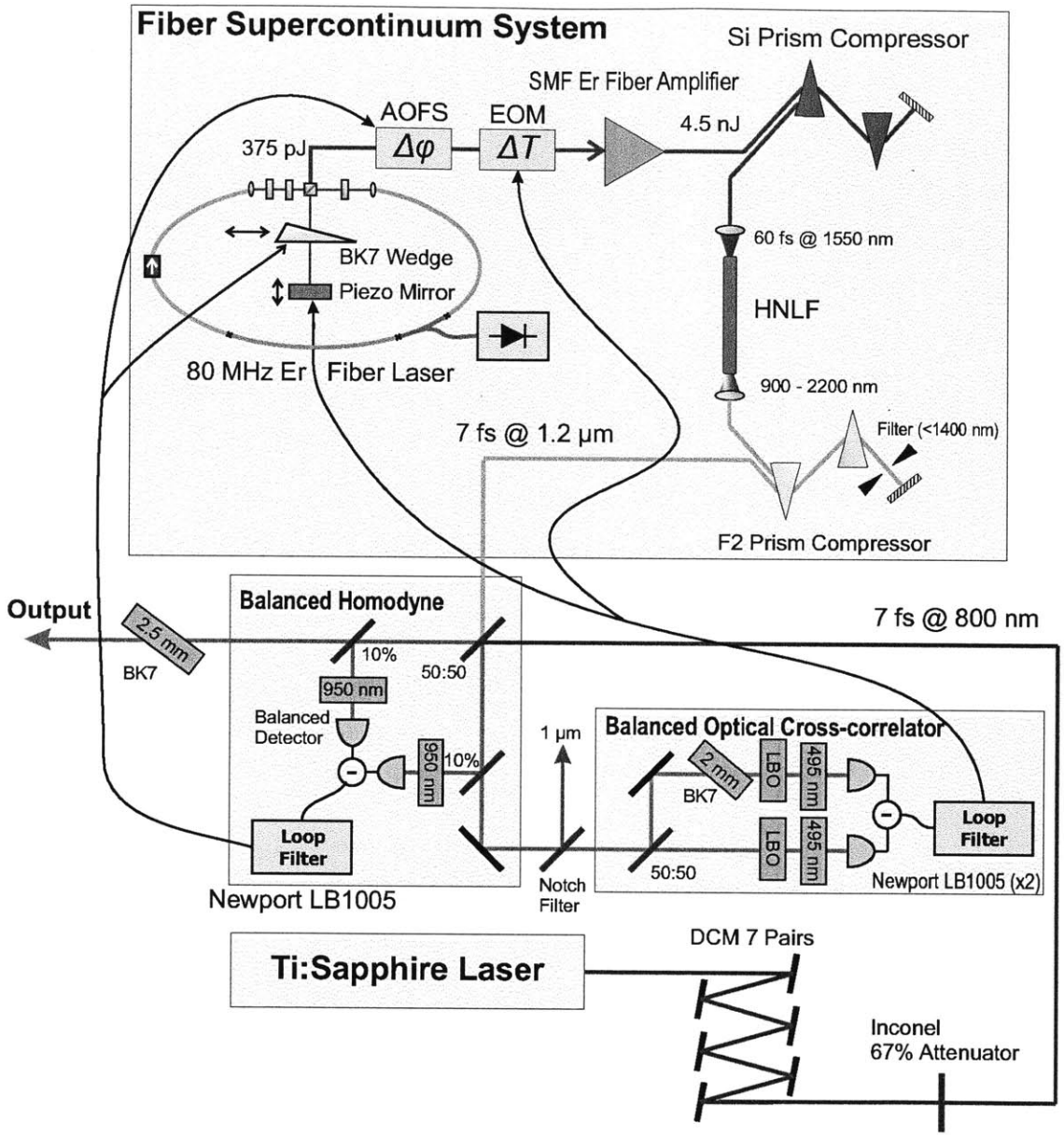

FIG. 51. Schematic of the coherent synthesis system. Fiber supercontinuum and Ti:S laser are combined on beam splitter. f_{CEO} is detected at balanced homodyne detector and pulse timing at the optical cross-correlator. The BK7 wedge and AOFS are used to lock the f_{CEO}, while the piezo mirror and EOM are used to lock the repetition rates / pulse timing.

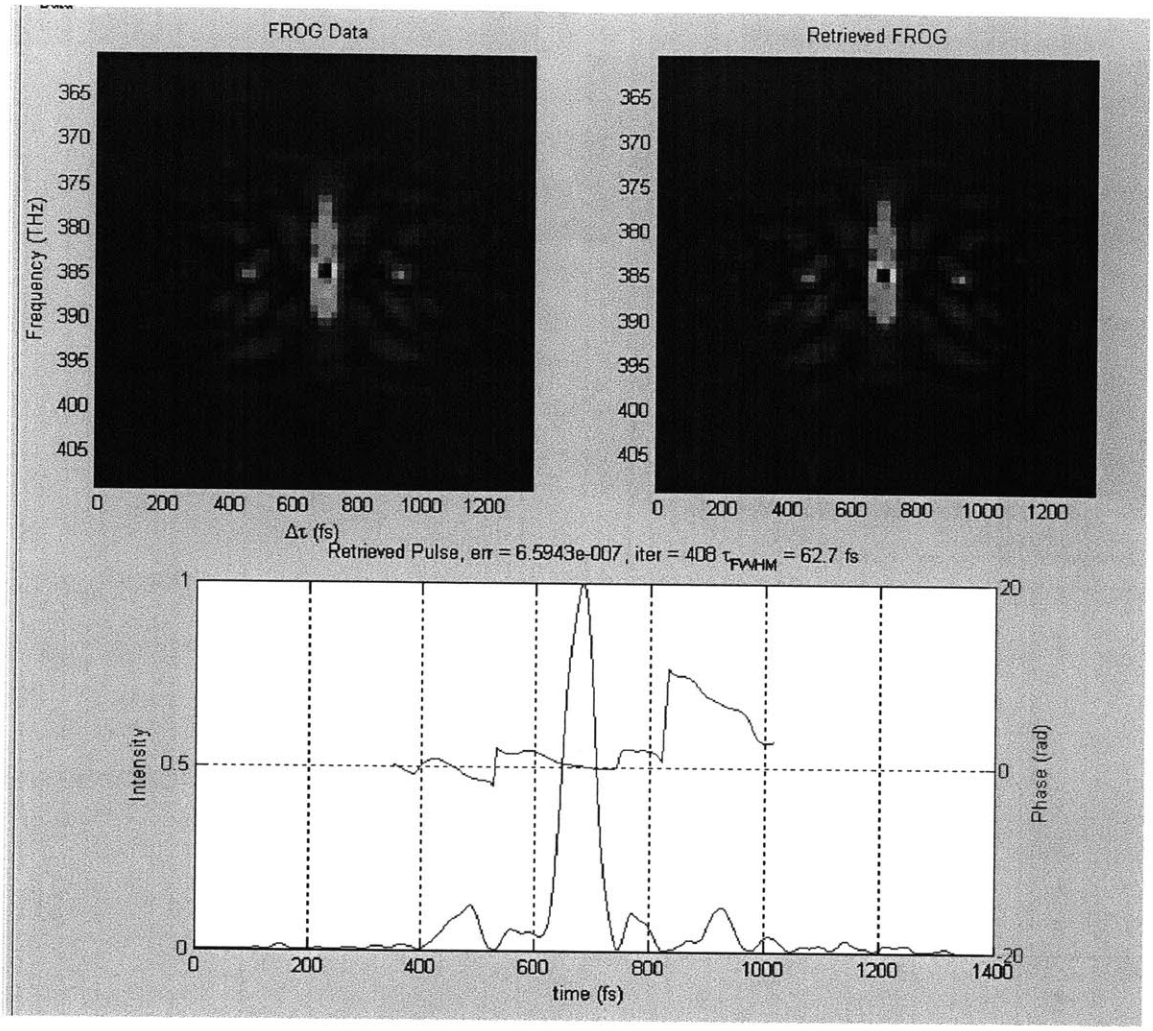

FIG. 52. Measured and retrieved FROG traces from the output of the EDFA, but before the highly non-linear fiber. The retrieved pulse duration is 63 fs.

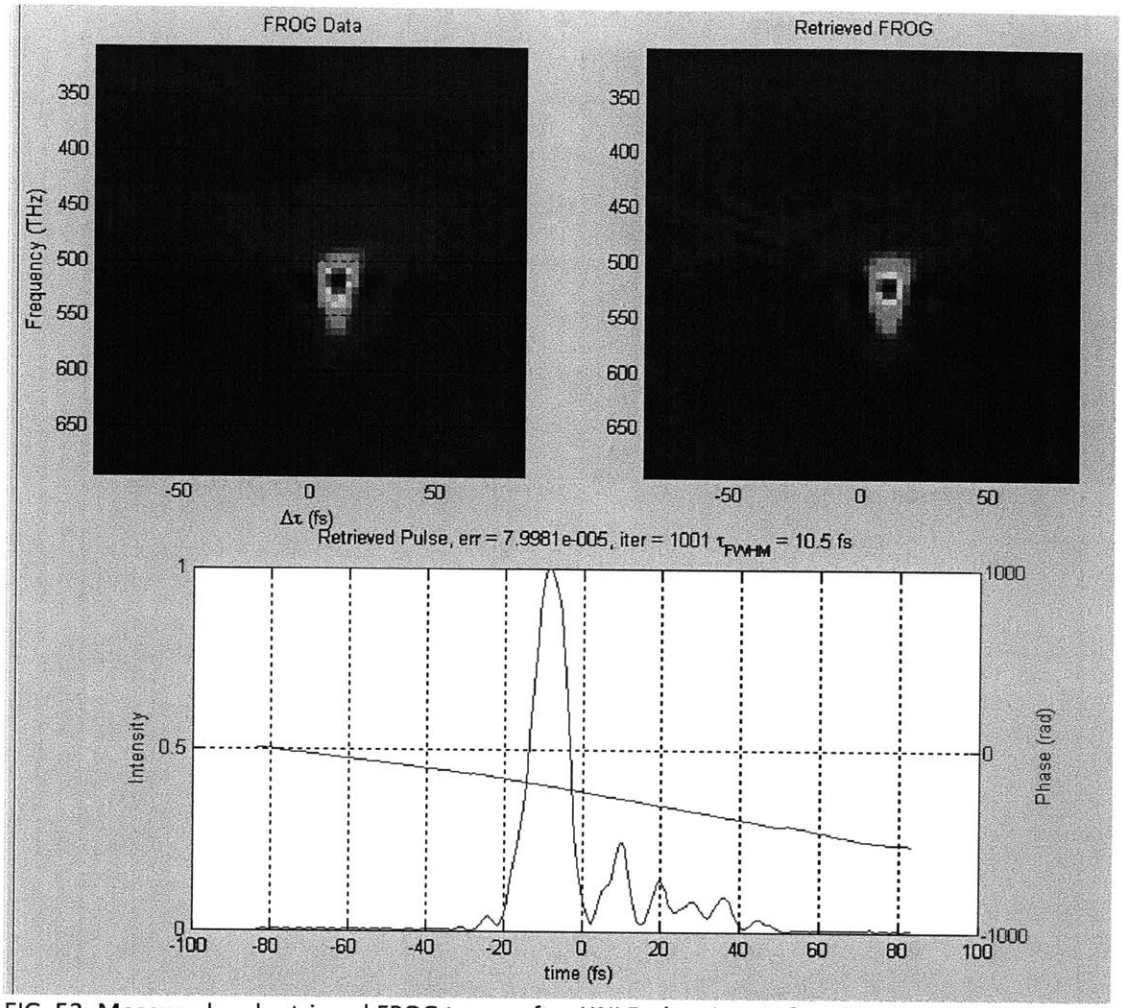

FIG. 53. Measured and retrieved FROG traces after HNLF, showing 10 fs pulse. It is apparent from the FROG spectrogram that the portion beyond 1200 nm wavelength is not well compressed by the F2 prisms. Fine adjustment of the prism compressor can achieve, at best, an 8 fs pulse.

5.4 Temporal Locking Approach and Absolute Jitter Measurement

The BOC consists of 1 mm LBO crystals that are Type-I phase matched for 820 nm and 1250 nm sum-frequency generation. The fundamental light around 1000 nm is first filtered with a thin film notch filter, so that it does not interfere at the balanced photodetector with the SFG pulses at 495 nm. The fixed group delay between arms of the BOC is provided by 2 mm of BK7 inserted at Brewster's angle. For convenience, the relative group delay from BK7 and fused silica glasses, between 1250 nm and 800 nm, is shown in FIG. 54. Also shown is the group delay for 2 mm plates inserted at Brewster's angle, accounting for the variation in angle of refraction across such a wide bandwidth.

The timing lock is adjusted with a movable piezo mirror within the fiber laser cavity. Since the mirror/piezo assembly has a sharp natural resonance at 60 kHz, the closed-loop bandwidth of the phase locked loop is 18 kHz. By measuring the residual timing jitter at the BOC, we determine the absolute timing jitter of the fiber laser as measured against the negligible timing jitter of the Ti:Sapphire. The resulting jitter spectral density plot is shown in FIG. 55. The timing synchronization between the fiber laser and Ti:Sapphire is about 2.2 fs rms from 700 kHz to DC. From 700 kHz to 100 kHz, the integrated jitter is only 250 as. However, the piezo resonance and low-frequency noise contribute fully 1.75 fs at 60 kHz and below. It is interesting to note that this measurement is an absolute measurement of fiber supercontinuum timing jitter since the Ti:Sapphire serves as a low-noise reference oscillator for comparison.

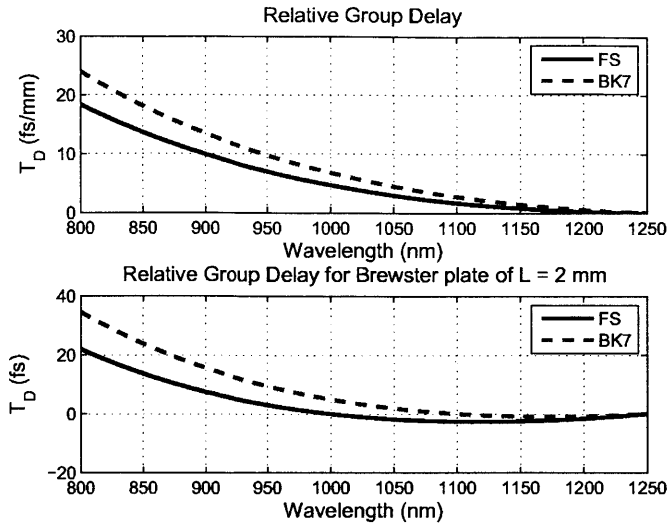

FIG. 54. Relative group delay between 1250 nm and 800 nm for BK7 and fused silica glass plates. The upper plot shows the group delay in fs/mm for a glass plate. The lower plot shows the group delay for a plate at Brewster's angle, accounting for the index variation and variation of angle of refraction across such a wide bandwidth. It can be seen that BK7 provides greater delay than fused silica.

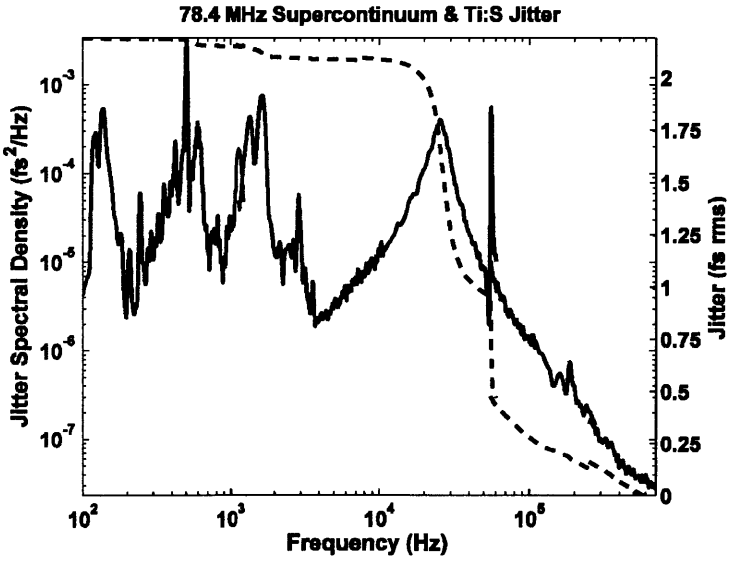

FIG. 55. Timing jitter between supercontinuum source and Ti:S laser as measured with thin crystal balanced optical cross-correlator. Detector bandwidth is 700 kHz. This measurement also provides the first absolute timing jitter measurement of an ultrafast fiber laser against a Ti:Sapphire reference.

5.5 Electro-optic Modulator as a High-Speed Timing Shifter

Timing jitter feedback with a piezoelectric mirror assembly can achieve 2 fs rms jitter with an 18 kHz bandwidth. For tighter synchronization in the attosecond regime, faster feedback is necessary. An electro-optic modulator (EOM) can be a high-speed actuator for pulse timing adjustment since it has no moving parts, unlike a piezoelectric stack. The EOM "phase shifter" works by exploiting the linear electro-optic effect (or Pockels effect), whereby the index of refraction of the crystal changes in proportional to the applied electric field. The change in refractive index with applied field is analogous to Hook's Law for a spring. Just as Hook's Law is only the first order Taylor approximation of the spring mechanics, the Pockels effect is the first order approximation of the index with respect to applied electric field. The full Pockels effect is given by (5.1), where the second order term is typically very small.

$$n(E) \approx n + \alpha E + \beta E^2 + \cdots \tag{5.1}$$

For materials such as ADP, KDP, Lithium Niobate and CdTe, the linear electrooptic effect is given by (5.2), where the index is proportional to the applied field [95]. This is different than the Kerr effect, where the change in index is proportional to E^2.

$$n(E) \approx n - \frac{1}{2} r n^3 E \tag{5.2}$$

Next, we ask to what extent the electrooptic effect perturbs the phase and group velocities? By Taylor expanding the group and phase velocity after inserting (5.2) for the index, we arrive at (5.3). We see that the phase velocity is perturbed by $v_p \propto cr(n/2)E$, where as the group velocity $v_g \propto cr(n/2 - \lambda \cdot \partial n/\partial\lambda)E$. The question therefore reduces to the value of $\lambda \cdot \partial n/\partial\lambda$ compared to $n/2$. For the ordinary axis of Lithium Niobate, $(n/2 - \lambda \cdot \partial n/\partial\lambda) \approx 1.158$ while $n/2 \approx 1.11$ at 1550 nm. Thus, we expect that group velocity will increase by 4% over phase velocity with a given applied field. Since the phase modulator has a range of only ±5 fs (at most), we expect up to ±200 as of carrier envelope phase noise

introduced by the phase modulator. However, ±200 as is only about ±60 mrad phase error assuming a center wavelength of 1 μm. Such a small amount of phase noise is tolerable.

$$v_p(E) = \frac{c}{n(E)} \approx \frac{c}{n} + \frac{1}{2} crnE + \cdots$$
$$v_g = v_p(E)\left[1 - \frac{\lambda}{n(E)}\frac{\partial n}{\partial \lambda}\right] \approx \frac{c}{n} - \frac{\lambda}{n}\frac{\partial n}{\partial \lambda} + cr\left(\frac{1}{2}n - \lambda\frac{\partial n}{\partial \lambda}\right)E + \cdots \quad (5.3)$$

In reality, less noise than 60 mrad is actually introduced into the fully locked system. Although ±60 mrad phase noise is possible due to a ±5 fs timing modulation, the feedback loops minimize this effect. For instance, almost all timing jitter for the fiber laser is below 60 kHz. However, since the carrier envelope phase feedback bandwidth is 450 kHz, the vast majority of additional phase noise is still eliminated.

The use of a phase modulator for high speed timing feedback has been demonstrated within the laser cavity. A bandwidth of 230 kHz has been reported with an intracavity, free space EOM [96]. However, an intracavity EOM would exacerbate the excess phase noise since the integrated timing adjustment is much higher for the intracavity actuator. In our scheme, we make the vast majority of timing corrections with the piezo mirror, and only compensate for ±5 fs of timing error with an extracavity EOM.

A two stage lock is implemented to leverage the strengths of both the intracavity piezo and the extracavity EOM. First, a tight, 2 fs rms lock is obtained with an intracavity piezo. Next, the high frequency, small amplitude fluctuations can be removed with a 10 GHz fiber coupled, lithium niobate waveguide EOM outside of the cavity. This has the advantage of being much faster and not perturbing the cavity or carrier phase significantly.

The waveguide electro-optic phase modulator is inserted after the fiber laser, but before the EDFA. Such devices commonly have a bandwidth of 10 GHz with a range of 2π, or about 6.6 fs at 1550 nm. The particular waveguide EOM employed in the apparatus has only 2 dB of loss. The EOM used is an EO Space lithium niobate waveguide phase modulator (2 dB loss, PM fiber) driven by a home built, high-current op-amp driver based on an Apex

Microtechnology PA98 op-amp. The op-amp driver has a useful bandwidth of about 4 MHz into the 50 Ohm load of the EOM.

A second loop filter is used to drive the EOM with the same error signal as used to drive the piezo loop filter. However, the EOM loop filter is configured to suppress high frequency noise with a fast response time. In addition, the EOM helps to suppress the natural resonance of the piezo, permitting the piezo loop gain to be increased, if desired. This effect helps reduce the jitter still further, albeit at the expense of reduced system stability.

The timing jitter with both piezo and EOM feedback loops enabled is shown in FIG. 56. The timing jitter is reduced to only 280 as rms, reaching the noise floor at 700 kHz. Interestingly, it can be seen that the low frequency fluctuations are not significantly suppressed because the amplitude of the fluctuations generally exceeds the travel of the fiber EOM. However, beyond 3 kHz, the jitter density is reduced by as much as 1000. In particular, the piezo resonance at 60 kHz is significantly dampened by the EOM.

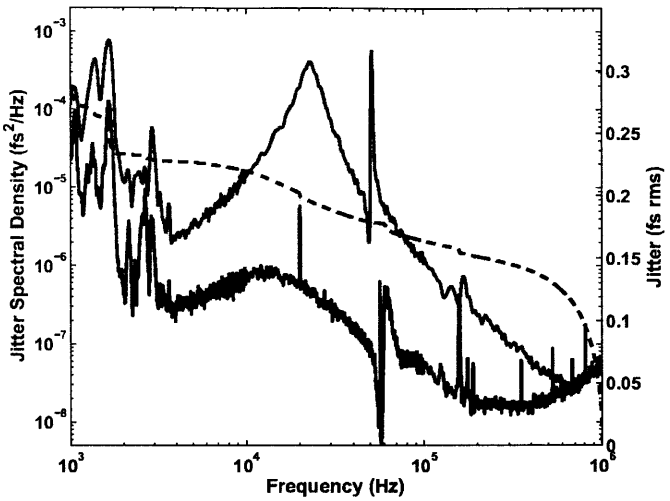

FIG. 56. Timing jitter spectral density (blue) and integrated timing jitter (dashed black) when the fiber EOM lock is enabled. Shown for comparison is the jitter density without the EOM lock (red). Note, the jitter is reduced from ≈2 fs rms to 280 as rms with the EOM lock. The jitter density rises beyond 700 kHz since the density reaches the noise floor of the photodetector, which has a bandwidth of 700 kHz.

While placing the fiber EOM outside the laser cavity simplifies design and construction, it is not without its limitations. Primarily, the limited phase shifting range, about 5 fs, means that strong, transient disturbances can exceed the range of the EOM. Fortunately, however, in a typical laboratory setting, vibration dampening materials and thick, acrylic boxes are incorporated to suppress most of the acoustic disturbances. In this way, a reasonable level of robustness can be achieved that permits fiber EOM locking for minutes.

5.6 Carrier Envelope Phase Locking

After a tight timing lock is achieved, the frequency combs from both lasers are identically spaced. However, the offset of each frequency comb freely shifts. The difference in these offsets must be detected and locked to zero, such that the harmonics of the frequency comb form one evenly spaced comb. It is important to recognize that the phase, not just the

frequency, must be precisely synchronized to the milliradian level. In this way, phase coherence between lasers is achieved.

The difference in f_{CEO} between the lasers is detected with a balanced homodyne detector, as shown in FIG. 57. Ten-percent of the power from one port of the combining beam splitter is sent to one photodiode, while ten-percent from the other port is sent to the other photodiode. A 10 nm wide band pass filter centered at 950 nm is placed before each photodiode. The band pass filter filters out a portion of spectrum for which each laser has some power. As a result, the frequency combs from both lasers beat, or mix, in the silicon photodiodes. The sum and difference frequencies of all of these lines are detected, which yields the f_{CEO}. To achieve amplitude insensitivity, this balanced detection scheme relies on the phase shift on reflection when the beams are combined on the beam splitter. If not for the phase shift between branches of the beam splitter, the balanced photodetector would see an identical signal in each photodiode. Instead, the phase shift yields a balanced error signal proportional to the cosine of the difference in the pulse carrier envelope phases.

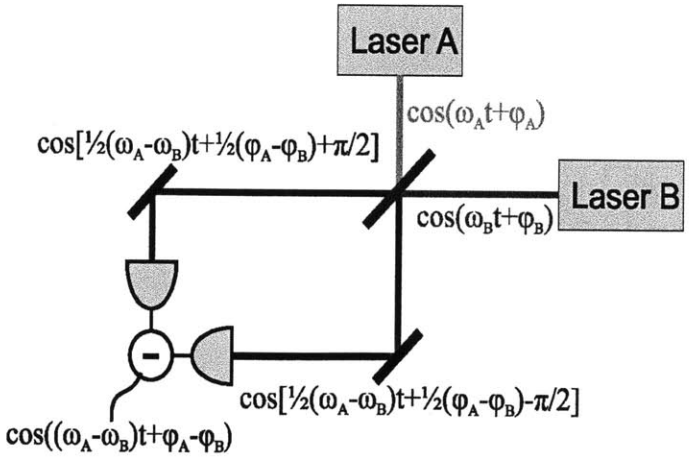

FIG. 57. Schematic of balanced homodyne detector used for detection of difference between f_{CEO} frequency and phase of laser combs. The π phase shift due to reflection off of the 50:50 beam splitter is the key to the balanced detection method.

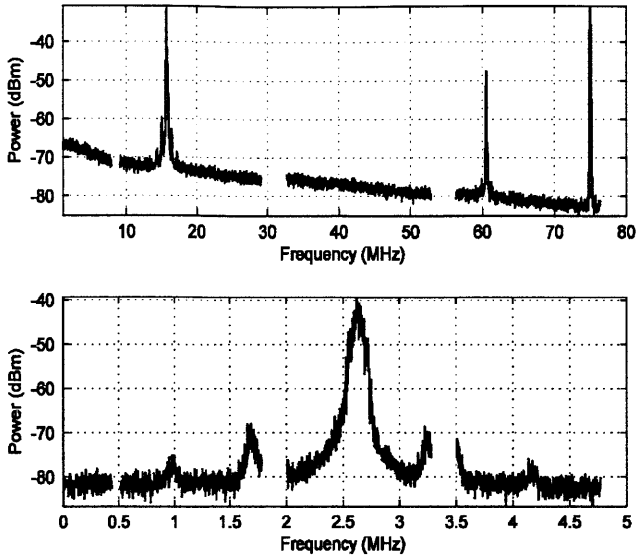

FIG. 58. f_{CEO} spectrum measured at the balanced homodyne detector between Ti:Sapphire and fiber supercontinuum. The Signal to Noise Ratio is 40 dB.

After locking the pulse timing, the f_{CEO} beat signal can be seen on the balanced homodyne detector because the beating of thousands of evenly spaced lines add coherently. FIG. 58 shows the free running f_{CEO} RF spectrum for the detector. The f_{CEO} beat appears as two relatively sharp lines at the sum and difference of the two laser's combs. These beat signals have a SNR of about 40 dB, which is considered quite satisfactory. Upon closer inspection, the power spectral density can be evaluated, as in FIG. 59. By fitting with a Gaussian, it is determined that the -3dB bandwidth of the beat is about 65 kHz, while the -10 dB bandwidth is about 200 kHz. This suggests that an actuator with a bandwidth in excess of 200 kHz is required to fully suppress all CEP fluctuations.

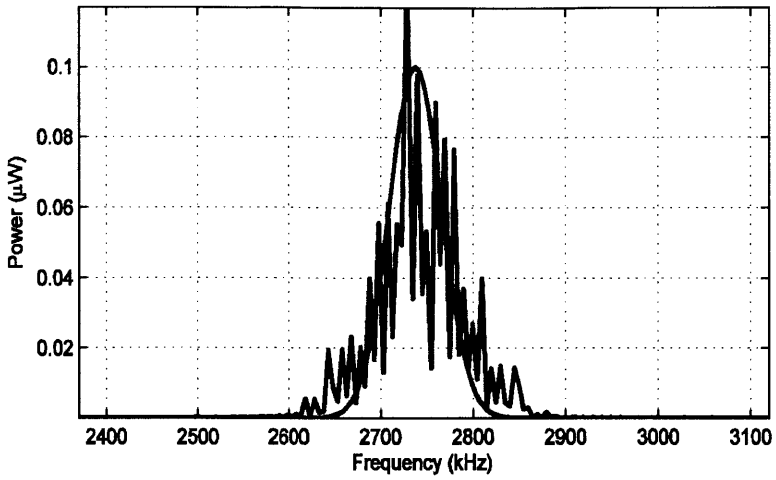

FIG. 59. f_{CEO} spectrum measured at the balanced homodyne detector. The spectrum is fit to a Gaussian with a -3dB bandwidth of 65 kHz.

The f_{CEO} is commonly stabilized by adjusting the pump power to the oscillator. Through non-linear effects, pump power modulation shifts the group velocity and phase velocity in the laser, shifting the f_{CEO} [25]. However, this scheme has several significant shortcomings. First, one cannot independently shift just the f_{CEO} without affecting the pulse timing through the group velocity. Therefore, stabilizing the f_{CEO} creates a tremendous amount of excess timing jitter, which is very difficult to suppress. In addition, the rate at which the f_{CEO} can be shifted by changing the pump power is severely limited by the upper state lifetime of the gain medium and the laser dynamics. For Ti:Sapphire, which has an upper state lifetime of 3 μs, the maximum bandwidth due to the laser dynamics has been shown to be 70 kHz [26]. On the other hand, erbium doped fiber gain media have an upper state lifetime of 3 ms, limiting servo bandwidth to a few kilohertz. However, through careful application of control theory, a maximum bandwidth of 80 kHz has been reported. Regardless, the pump intensity to timing jitter coupling is so significant that both timing and phase locks cannot be simultaneously achieved [88].

5.7 Acousto-optic Frequency Shifter for f_{CEO} Stabilization

Sub-cycle laser synchronization requires overcoming the limitations of existing f_{CEO} locking methods. A technique widely known for beam combining of CW lasers, and only recently considered for pulsed lasers, is carrier phase shifting with an acouto-optic frequency shifter (AOFS) [24], [79], [97]. Recently, an AOFS was used to stabilize the CEP of a portion of an octave spanning frequency comb using a feed-forward technique [24]. However, feed forward lacks long-term, drift free operation.

Equally as important, placing the AOFS after the supercontinuum diffracts only a narrow bandwidth, and cannot stabilize the entire supercontinuuum. Only a fraction of the supercontinuum can satisfy the Bragg diffraction criteria, (5.4). For the Bragg condition, f_s is the frequency of the AOFS driving signal, while c_s is the speed of sound in the medium. Fortunately, since the Bragg angle is a relatively soft function, the entire bandwidth of a typical stretched pulse erbium fiber laser (60 nm) can be diffracted with negligible filtering. Therefore, to eliminate out-of-loop drifts and stabilize the entire supercontinuum, the f_{CEO} of the supercontinuum is stabilized by placing an AOFS outside the fiber laser cavity, but before the amplifier and highly non-linear fiber.

$$\theta = \sin^{-1}\left[\frac{m\lambda}{2}\frac{f_s}{c_s}\right] \tag{5.4}$$

Since the AOFS is placed before the saturated EDFA, the output of the AOFS is regenerated. Of course, since the AOFS is also used in a feedback system, the stabilization is immune to slow drifts. Feed forward systems suffer from thermal drifts in the uncompensated signal path due to the coaxial cables, mixers and other microwave devices. As the AOFS is inserted before the EDFA and fiber supercontinuum, spatial effects such as beam spreading and driving frequency dependent beam pointing are eliminated. Instead, the diffracted beam is coupled back into a single mode amplifier before supercontinuum generation.

However, since the Bragg condition induces a frequency dependent angle of diffraction, the tuning range of the AOFS should be limited to ±5 MHz. In this way, <10% power fluctuation occurs over this tuning range. Larger fluctuations cause noticeable attenuation when coupling into the single mode fiber of the EDFA. Such a tuning limitation is enforced in the feedback loop via an op-amp voltage shifter placed after the loop filter.

The AOFS can also be operated in a double pass configuration to minimize driving frequency dependent diffraction angle effects. This tends to reduce variations in beam pointing with driving frequency, at the expense of additional optical complexity [98]. However, a double-pass configuration is not necessary because more than ±5 MHz tuning range is not needed to lock the f_{CEO} of this laser for an extended length of time.

The power loss due to AOFS driving frequency can be compensated for electronically over a bandwidth of, for example, 10—25 MHz. The author believes that this simple, passive, electronic approach is more practical than the additional complexity of the double-pass AOFS scheme. By exploiting the tuned RF circuit in the AOFS, which has a limited matching bandwidth, fiber coupling loss can be compensated by AOFS decreasing reflected RF power. The AOFS RF port contains a tuned circuit which matches the acoustic transducer to 50 Ohms. By intentionally inducing a "bad match", either by tuning the matching circuit, or constructing an external impedance mismatch network, the variation of reflected power verses RF drive frequency can compensate the walk off angle into the single mode fiber. The AOFS should be driven at a center frequency corresponding to maximum reflected RF power. Frequency variations above and below the drive frequency reduce the reflected power and compensate for the walk off into the fiber collimator. This scheme was successfully tested, but is not strictly necessary for a modest tuning range of 10 MHz—especially since the EDFA is already saturated.

The AOFS operates by propagating a sound wave through a glass or crystal, forming a compression wave that causes a periodic index variation in the material. The transversely propagating optical beam diffracts from the traveling acoustic Bragg grating. Since the

grating is in motion, the optical beam undergoes a Doppler shift. Said differently, the photons are scattered by propagating phonons, conserving momentum. As a result, the diffracted beam is frequency shifted by exactly the frequency of the acoustic wave. Thus, the AOFS gives one a method for precisely shifting the f_{CEO} of the optical frequency comb by the frequency of the driving acoustic wave. Also, since phase is simply the time integral of frequency, the phase of the entire frequency comb can be controlled very precisely by changing the AOFS driving frequnecy. Fortunately, the AOFS can be a very fast device, depending on materials and geometry. Typical response times are on the order of 1—10 MHz. More importantly, the AOFS induces no observed timing shift and little intensity modulation.

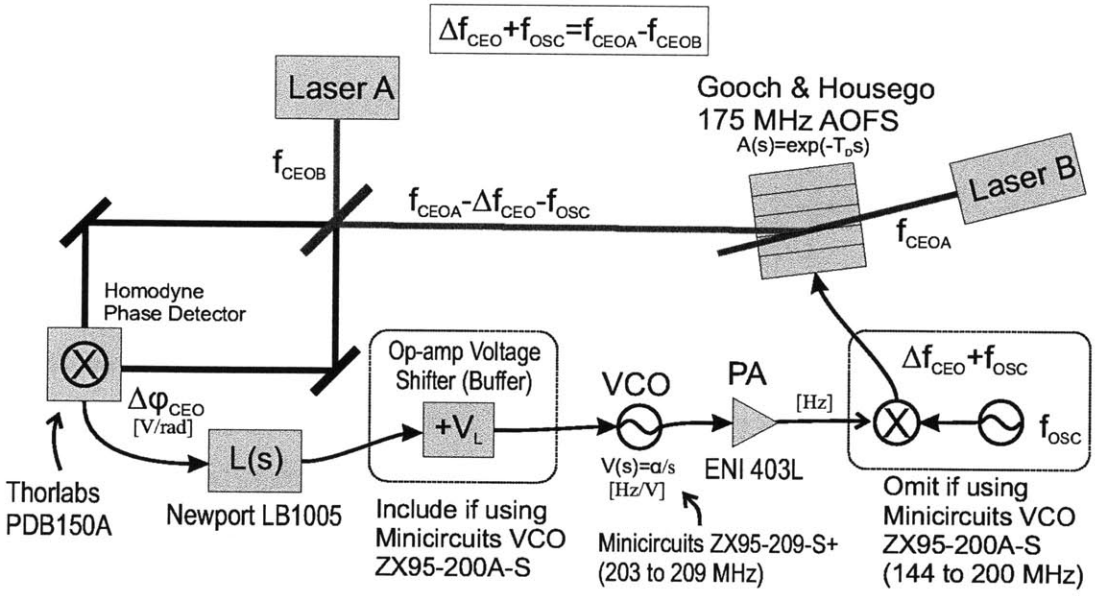

FIG. 60. Schematic of f_{CEO} locking system. The f_{CEO} difference frequency is detected by the balanced homodyne detector, processed by the loop filter, L(s), and sent to the VCO. It is then mixed with an RF oscillator that only serves to drive the AOM (or AOFS) at its center frequency. The AOM is then driven with the mixed signal, which subtracts from the f_{CEO} of Laser B.

The AOFS f_{CEO} locking system works by rapidly modulating the frequency, not the amplitude, of the acoustic wave driving the AOFS. For instance, if the balanced homodyne

detector detects a phase increase, the phase of the signal driving the AOFS is decreased to counteract this change, as described by FIG. 60. This frequency shift is written directly onto the optical frequency comb. Depending on the direction of diffraction, relative to the propagation direction of the acoustic wave, either a red or blue Doppler shift is experienced by the optical beam. This negative or positive shift is equivalent to negative or positive feedback, and makes it possible to invert the feedback loop simply by changing the angle of the AOFS relative to the incident optical beam.

In particular, the phase error between the lasers, which is detected by the homodyne phase detector, is fed to a loop filter, L(s). In turn, the loop filter adjusts the frequency of a voltage controlled oscillator (VCO) to change the driving frequency of the AOFS, and hence, the f_{CEO} of the laser. In the diagram, a mixer is incorporated to mix the VCO frequency down to the center frequency of the AOFS with a stable microwave source at fOSC. If a VCO with a center frequency the same as for the AOFS is available, this mixer stage can be omitted. Both methods have been tested with similar results, except that a lower noise VCO that does not have a center frequency suitable for the AOFS is available. The AOFS used has a center frequency of 175 MHz and is made with TeO_2 material.

Due to the limited frequency shifting range of the AOFS (±5 MHz), the fCEO of the fiber laser must be coursely tuned via the intracavity BK7 glass wedge. By changing the insertion of the glass wedge inside the fiber laser cavity, the amount of phase slip per round trip can be tuned over a 2π range. In other words, the AOFS is only a limited range, high-speed actuator.

The locking bandwidth of the AOFS feedback technique can be estimated by determining the sources of delay in the feedback loop. The principle source of delay for the AOFS is the propagation time of the acoustic wave. Time delay in a feedback loop directly limits closed loop bandwidth. A negative feedback loop must have less than 2π total phase shift around the loop to avoid oscillation. In reality, a phase margin of $\pi/4$ is necessary to avoid ringing. A π phase shift is automatically present in a negative feedback loop due to the

inverter in the loop. Also, the loop filter, which is an integrator, contributes another $\pi/2$ phase shift. Since $2\pi - \pi - \pi/2 - \pi/4 = \pi/4$, the AOFS can add at most $\pi/4$ additional loop phase before the loop begins to oscillate.

For a closed loop bandwidth of 500 kHz, we therefore require a loop time delay of no more than 250 ns. Since the fiber laser has a beam diameter of 1.3 mm, the acoustic wave must propagate about 2 mm at 4,300 m/s in TeO_2 to span the beam. Thus, there is a delay of 470 ns. Therefore, the beam size must be reduced to achieve a 500 kHz lock. The solution is to focus the beam through the center of the AOFS and collimate with an identical lens. This is implemented with a pair of f = 100 mm achromatic lenses. The beam waist in the AOFS is correspondingly reduced to 150 μm, for which we expect an acoustic propagation delay of 35 ns. This should allow for a closed loop bandwidth of 3.6 MHz. In practice, there are additional sources of time delay in the loop, including the loop filter, the cables and the op-amp voltage limiter. In addition, it is not possible to focus the beam exactly on the edge of the AOFS transducer. A buffer zone of at least 250 μm is necessary to avoid beam clipping.

The AOFS used in this work is a TeO_2 device designed for a 200 μm beam, with a driving frequency of 175 MHz. Since it is intended as a fiber coupled frequency shifter, the transducer has broad bandwidth and is designed for a small beam aperture. The beam is focused through the AOFS with a pair of f = 100 mm achromatic lenses. The diffracted beam is coupled into a PM fiber, and connected to the waveguide phase shifter.

When the AOM phase lock is achieved, the residual phase noise is only 200 milliradians, as shown in FIG. 61. The loop bandwidth is about 450 kHz, which can likely be improved with faster electronics. The bulk of the residual noise is beyond 400 kHz. Of course, 200 milliradians is only $1/30^{th}$ of an optical cycle, and is more than satisfactory for phase locking. Below 100 kHz, there is virtually no phase noise remaining.

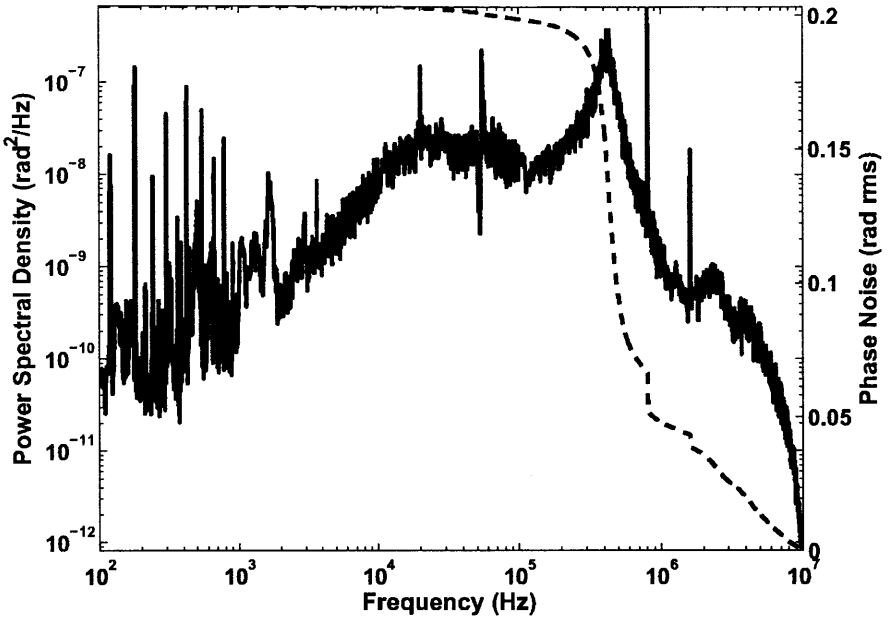

FIG. 61. Phase noise spectral density measured from balanced homodyne detector when AOM f_{CEO} lock is enabled. Note, the closed loop bandwidth is approximately 400 kHz, as compared to the 70 kHz typically achieved through pump-power modulation. Also, the f_{CEO} is locked to zero frequency and phase, such that there is no offset in the frequency combs of the lasers.

5.8 Pulse Measurement

After coherently synthesizing a frequency comb spanning 1400 nm to 650 nm, our attention can turn to measurement of the synthesized pulse. Pulse characterization techniques, such as frequency resolved optical gating (FROG) and two-dimensional spectral shearing interferometry (2DSI) serve as a diagnostic tool for optimizing the synchronization system.

Locking the pulse timing with the BOC does not guarantee perfect temporal overlap—only that timing between pulses is fixed. It is critical that the group delay between both pulses be minimized to achieve the shortest synthesized pulse. Many factors influence the precise group delay between the two pulses, at the system output, when the timing is locked. For instance, any imbalance in the type or amount of glass on either side of the

combining beam splitter (after the pulses are combined) will lead to a temporal offset. Glass placed in the beam path of each individual laser, before they are combined on the beam splitter, does not affect the temporal locking offset. In theory, it is possible to precisely calculate and account for all group delay elements, such as the beam splitters, mirrors, BOC group delay element and even the LBO crystal in the BOC. In fact, these calculations are summarized in Chapter 2 and in FIG. 54. In practice, since there is uncertainty and variation in the center wavelengths of the pulses and the glass optics, it is necessary to measure the combined output and optimize the temporal overlap. After all, five femtoseconds of group delay between pulses corresponds to only 250 μm of fused silica. For this reason, a 2.5 mm BK7 glass plate at Brewster's angle is placed at the combined output in FIG. 51. This glass plate adjusts the group delay offset of the two pulses such that they are overlapped at the output.

5.8.1 Frequency Resolved Optical Gating (FROG)

Measurement of the combined pulse is performed with both frequency resolved optical gating (FROG) [92], [93] and two-dimensional spectral shearing interferometry (2DSI). However, FROG is useful for characterizing the effectiveness of the f_{CEO} lock since it is sensitive to the coherence of the pulses. Measurements of the combined output were conducted with a FROG containing a 10 μm thick, Type-I BBO crystal with a phase matching angle of 29 degrees. In theory, such a thin piece of BBO could frequency double a few-cycle pulse centered at 950 nm. In practice, even if such phase matching bandwidth is possible, coupling this broad bandwidth efficiently into the spectrometer is a challenge. Nonetheless, FROG is an effective diagnostic tool.

FROG spectrograms of the combined output, recorded for locked and unlocked states, are shown in FIG. 62. When both timing and phase locks are disabled, the optical SHG bandwidth is limited. When the timing and phase locks are enabled, the SHG pulse

bandwidth increases dramatically and the pulse duration narrows. The combination of increased bandwidth and narrower pulse duration is a consequence of constructive interference, demonstrating the effectiveness of the synchronization system. FROG retrieval is not presented since the spectral filtering from the phase matching and spectrometer produces an unreliable retrieval. Instead, the autocorrelation can provide an estimate of the pulse duration. FIG. 63 shows the autocorrelation as computed from the FROG spectrograms for different locking states. The measured pulse duration decreases to the resolution limit of the FROG as the timing lock and phase lock are enabled. As the frequency combs are locked, the pulse duration shrinks from 8 fs (assuming sech^2 shape) to 5 fs.

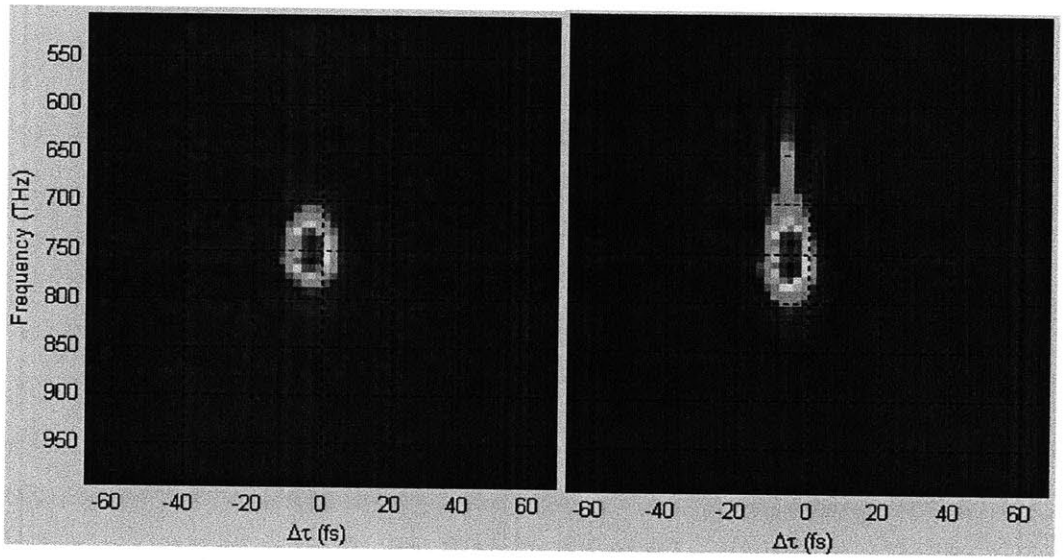

FIG. 62. Frequency resolved optical gating (FROG) spectrograms for combined pulse output. On the left is the FROG spectrogram when the timing and phase locks are disabled. On the right is the spectrogram when both locks are enabled. The broader bandwidth and shorter duration prove phase and timing coherence.

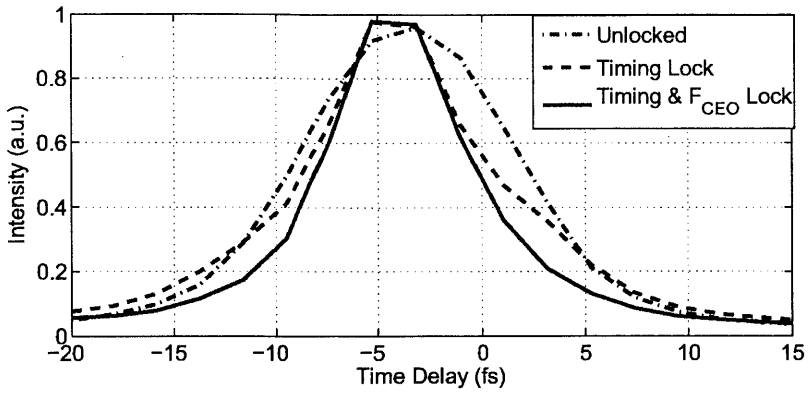

FIG. 63. Autocorrelation computed from FROG spectrogram of combined system output for three locking states. With all loops unlocked, an 8 fs pulse is measured (assuming $sech^2$ shape). Enabling the timing lock decreases the measured pulse duration. Further enabling the f_{CEO} lock decreases the pulse duration to the limit of the FROG resolution of 5 fs. The resolution limit is due to the 2 fs step size of the delay motor and the frequency response of the BBO crystal and spectrometer.

5.8.2 Two-dimensional Spectral Shearing Interferometry

For a more precise measurement of spectral group delay, two-dimensional spectral shearing interferometry (2DSI) is used [99]. 2DSI has the advantage over FROG that it is a direct measurement of spectral group delay. In other words, no iterative deconvolution algorithm is needed to extract the pulse shape. Most importantly, however, 2DSI is insensitive to phase matching bandwidth and spectral filtering. The spectral information is encoded in the delay of the fringes, and not in the amplitude. These advantages make 2DSI an attractive technique for measuring pulses down to single cycle duration [99].

The 2DSI implemented for this work is of the standard design, using a 30 μm Type-II BBO crystal with a phase matching angle of 42.4 degrees. The phase matching bandwidth of this crystal extends from 600 nm to beyond 1600 nm, although coupling the entire bandwidth into the spectrometer remains challenging. By carefully focusing the sum-frequency light from the BBO crystal into the spectrometer slit with an f = 100 mm curved mirror, the combined spectrum can be fully captured.

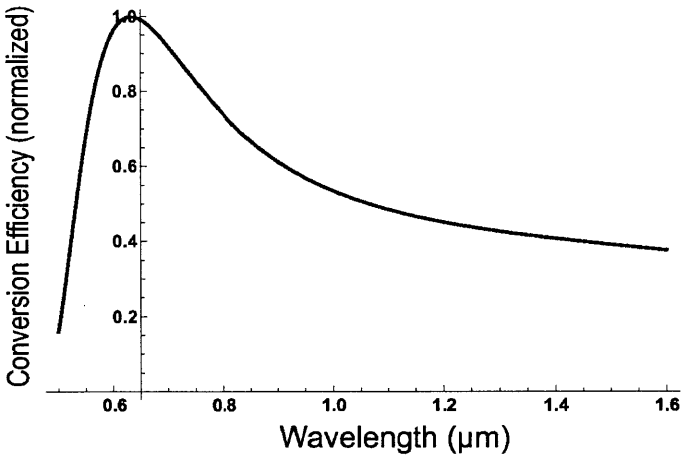

FIG. 64. Conversion efficiency of 30 μm Type-II BBO crystal with a phase matching angle of 42.4 degrees, for an 850 nm CW ordinary wave. The phase matching bandwidth of this crystal extends from 600 nm to beyond 1600 nm.

The measured 2DSI spectrogram and combined spectrum is shown in FIG. 65, as recorded with a 5 THz shear frequency. The supercontinuum spectrum above 1200 nm is filtered with a knife edge in the prism compressor. This is done because the F2 prism compressor has too much third order dispersion beyond 1200 nm to effectively compress the portion beyond 1200 nm. With 2DSI, the non-linear generation in the BBO is between a highly chirped, quasi-CW pulse around 800 nm and a few percent of the transform limit pulse power. Therefore, the signal strength is very poor since the combined output is only 35 mW at 78.4 MHz. To improve signal to noise ratio of the 2DSI spectrogram, the 2DSI spectrogram is recorded without attenuating the Ti:Sapphire beam. Otherwise, the Ti:Sapphire pulse energy is equalized to the supercontinuum pulse energy by inserting a 67% reflective Inconel alloy filter at the Ti:Sapphire ouput. The sensitivity of the balanced homodyne phase detector and balanced optical cross-correlator is great enough that attenuation of the Ti:Sapphire does not impact synchronization performance. It can be seen from visual inspection of the 2DSI spectrogram that the group delay is flat across the entire bandwidth.

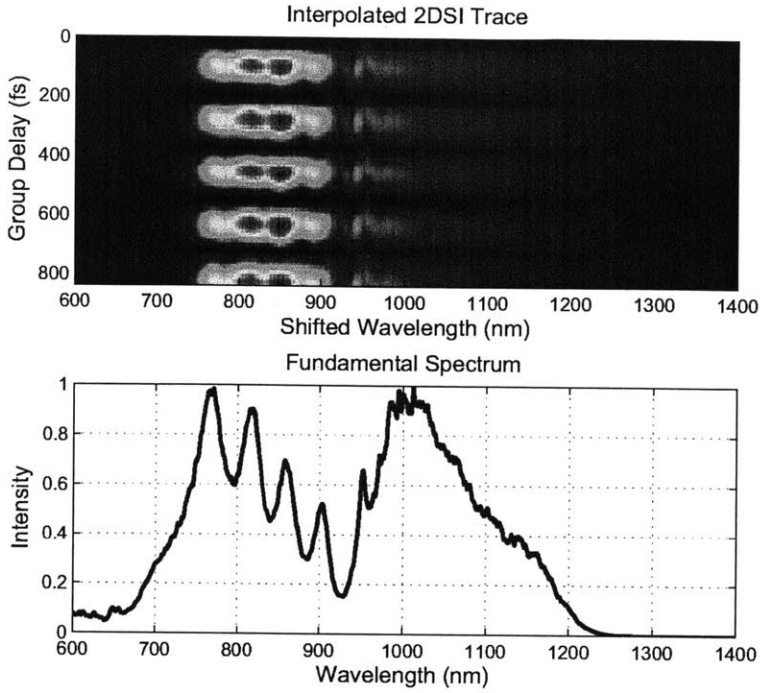

FIG. 65. Upper plot shows the measured 2DSI spectrogram for combined system output. The group delay appears flat across the entire bandwidth. The lower plot shows the measured optical spectrum of the combined output from 600 to 1400 nm. The Ti:Sapphire output is not attenuated while recording the 2DSI spectrogram to improve signal to noise ratio and reduce spectrometer integration time.

After extracting the spectral group delay, the retrieved pulse shape can be determined. The retrieved pulse and the ideal transform limited pulse are plotted in FIG. 66. The measured pulse duration is 4.7 fs FWHM, while the transform limited duration would be 4.2 fs with perfect dispersion compensation. The residual spectral phase is shown in the lower portion of the plot. It can be seen that the phase varies by about one radian over the optical spectrum.

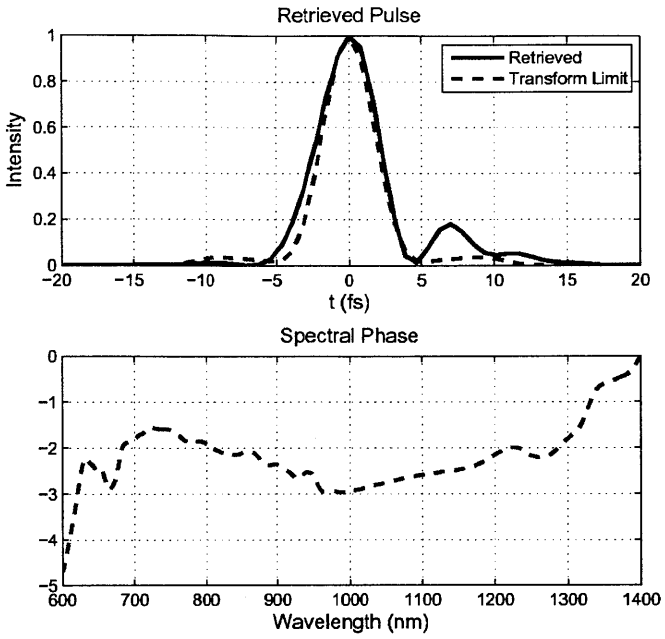

FIG. 66. Upper plot shows the retrieved and transform limited pulse shapes with 2DSI. The lower plot shows the retrieved spectral phase. The pulse duration is 4.7 fs, while the transform limit is 4.2 fs.

6 Conclusions and Future Work

This dissertation presents a set of techniques for sub-femtosecond control of ultrafast optical pulse timing and carrier wave phase. These techniques are useful for timing distribution, low noise signal generation and coherent synthesis of pulsed optical sources.

6.1 Timing Distribution and Synchronization

The need for femtosecond precision timing synchronization of X-ray free electron lasers (X-FELs) has motivated research toward distributing ultrafast pulse trains over fiber links without introducing additional timing jitter or slow drift. X-FELs coming online range in length from 300 to 3000 meters. Over the entire length of the facility, from the photoinjector laser to the scientific users (located at opposite ends) femtosecond timing synchronization is required for conducting ultrafast temporal investigations for physics, biology and chemistry. These large scale devices promise to usher in the era of the ultrafast X-ray movie for femtosecond, time resolved, three-dimensional diffraction imaging of chemical and biological processes [9].

Timing distribution and synchronization over optical fiber with ultrafast pulses has many advantages over other techniques. First, since the pulse timing itself is directly detected and corrected with the balanced optical cross-correlator, there is no ambiguity introduced by stabilizing the phase delay instead. Interferometric schemes based on CW lasers correct for the phase velocity, but transmit information over the link with the group velocity. Uncertainty between group and phase velocity can be significant at the femtosecond level, as the index of the fiber drifts. Secondly, since the entire femtosecond

pulse is transmitted, and not simply a single frequency, the entire frequency comb is available at the output. The frequency comb may be directly used for synchronizing other ultrafast lasers or for microwave extraction of the thousands of harmonics with RF mode spacing. Finally, from a practical stand point, since an ultrafast pulse train at 200 MHz has a spatial pulse separation of one meter, it is always possible to restore a broken timing lock to the original position. In contrast, interferometric locks are periodic with the wavelength of light. Thus, if the lock is to break, it cannot be uniquely restored to exactly the same fringe.

For X-FEL sychronization, timing distribution and synchronization across 340 meters of single mode optical fiber has been demonstrated [9]. With a highly stable and sensitive balanced optical-cross correlator, attosecond resolution measurement of pulse timing has been shown over short and long time scales. By directly measuring the time of flight (or group delay) of ultrafast pulses circulating in a SMF link with the BOC, and making group delay corrections at kilohertz rates through piezoelectric and motorized feedback, sub-femtosecond timing distribution is achieved. At one second time scales, timing jitter is less than 500 attoseconds rms, and remains below 1.5 femtoseconds rms at up to 10,000 second time scales. Over an entire week of continuous, unaided operation, a drift of 5 fs rms is achieved. Furthermore, timing transfer from master oscillator to remote laser has been demonstrated over 5 hours with 3.7 fs rms drift using the long crystal BOC device.

Analytical analysis of both long and short crystal balanced optical cross-correlators has revealed both the fundamental limits to performance and provided a framework for engineering and development of such devices for other wavelengths and pulse durations. It is found that for parameters typical for fiber timing distribution links, 13 as rms precision resolution (limited by thermal noise of the photodetector) is achievable. Furthermore, numerical simulations of timing links suggest that sub-femtosecond precision is possible with careful attention to avoiding non-linear effects and polarization mode dispersion (differential group delay) in the fiber. Also, the analysis concludes that the timing sensitivity of the long crystal BOC is independent of pulse duration, to first order. This suggests that

the BOC technique is a versatile method for synchronization of both femtosecond and picoseconds lasers alike.

6.2 Future Work Toward Attosecond Timing Distribution

Going forward, long term timing synchronization at kilometer length scales with sub-femtosecond drift will be required for X-FELs. Already, X-FEL pulse duration has exceeded expectations, and further refinement toward the attosecond regime is anticipated. The techniques and studies presented in this dissertation lay a foundation for reaching attosecond precision timing distribution for many days.

Significant development toward fully waveguide based timing detection and synchronization is likely needed to achieve attosecond timing distribution [30]. Since a waveguide can confine an optical mode with a very small effective area over a long distance without diffraction, great timing sensitivity can be achieved. Currently, conversion efficiency with bulk PPKTP is typically less than 1%. Improvement by one order of magnitude is possible with an integrated, waveguide cross-correlator. This permits not only higher resolution, but also allows the pulse energy in the fiber link to be decreased, further preventing detrimental non-linear effects. Also, from a practical standpoint, waveguide devices eliminate drifts from thermal alignment issues that degrade the performance of bulk systems.

Secondly, but most immediately, the problem of fiber polarization mode dispersion (differential group delay) must be overcome. State-of-the-art single mode fiber has many tens of femtosecond of DGD over just a few hundred meters of fiber. Slow, thermal variations in fiber stress lead to time varying birefringence that causes drift. This effect is immediately obvious since out of loop drift can be caused by simply touching or pressing on the fiber link. The ideal solution is to develop a timing link based on polarization maintaining fiber. The backward traveling pulses from the end of the fiber link should travel along the

same polarization state, and be separated at the beginning of the link with a circulator. In this way, PMD is eliminated since there is only one polarization state in the fiber.

The central challenge toward implementation of a PM fiber link is simply the dispersion compensation of the fiber. The optical telecommunications industry has devoted significant resources toward the production of dispersion compensating fiber for standard single mode fiber at telecommunications wavelengths. For fiber timing links, one desires an equivalent dispersion compensation scheme based on either PM DCF or PM fiber chirped Bragg gratings. Either method requires compensation for both dispersion and dispersion slope. A fiber Bragg grating may be ideal since the pulse is rapidly chirped and recompressed in a few centimeters of fiber grating, reducing non-linear effects. Also, the Bragg grating can be based on standard mode area PM fiber, and not small-core DCF. This will reduce effective non-linearity over DCF. Investigation of the temperature sensitivity of fiber Bragg gratings will be required to see if the stability of the dispersion compensation can be maintained. Otherwise, time fluctuating pulse chirp is expected to couple to timing drift through non-linear effects in the fiber and distorted pulse shape corrupting the BOC.

6.3 Ultrafast Laser Timing Jitter

Ultrafast timing distribution for X-FELs depends on the expectation that ultrafast lasers have low timing jitter. Some X-FEL implementations may require tight synchronization between a microwave master oscillator and the optical master oscillator. Some components of the X-FEL may be synchronized directly to the microwave oscillator, while other remote components may be synchronized through the timing link.

In theory, the inherently low noise timing jitter properties of ultrafast lasers make them an ideal candidate for microwave signal generation. With femtosecond pulse duration, ultrafast lasers have can have low timing jitter when implemented properly. In contrast, the low frequency of microwave oscillators presents a fundamental limitation

toward sub-femtosecond signal generation. For instance, the effective resolution for analog-to-digital conversion can be limited by the aperture jitter of the sampling clock. For this reason, photonic based analog-to-digital conversion has been investigated for achieving high resolution sampling rates of tens of gigahertz.

However, it is certainly not automatic that ultrafast lasers provide ultra-low timing jitter. While studied to some extent through analytical and numerical techniques, the experimental evidence has not been entirely convincing. Experimental investigations have repeatedly reported significantly greater timing jitter than theory [29], [35], [39], [100]. Furthermore, the limited measurement resolution of traditional techniques has made it impossible to faithfully measure the high-frequency timing jitter. The timing jitter performance at fast time scales is especially important because robust microwave oscillators already provide very stable performance at longer time scales. For instance, atomic clocks, Masers and sapphire loaded or cryogenic cavity oscillators provide good timing stability for the long term—albeit at significant cost.

Because the timing jitter of the passively mode-locked laser is infinite (at timescales approaching infinity), the mode-locked laser is not the total solution for low-noise microwave generation. Instead, the strengths of microwave techniques must be combined with ultrafast lasers. The timing jitter density of ultrafast lasers theoretically declines at a $1/f^2$ rate, reaching attosecond (or less) levels at the Nyquist frequency. Therefore, a passively modelocked laser can be tightly synchronized to a long-term stable microwave reference to achieve low-noise signal generation from short to long time scales.

However, the actual, quantum origin timing jitter of passively mode-locked ultrafast lasers must be experimentally characterized all the way out to the Nyquist frequency. Only in this way, can the low-noise properties be conclusively demonstrated.

To this end, the quantum-origin timing jitter for ultrafast, passively mode-locked, erbium fiber lasers has been thoroughly studied out to the Nyquist frequency for the first time. This feat is accomplished using the long crystal, PPKTP balanced optical cross-

correlator for attosecond resolution timing jitter measurement. For two identical, 80 MHz stretched-pulse fiber lasers, the timing jitter is measured as 2.6 fs rms [10 kHz, 40 MHz], for one laser. However, when the intracavity waveplates of this additive pulse mode-locked laser are improperly adjusted, an additional 5.5 fs rms of jitter is present in a spurious signal at the Nyquist frequency. Also, small, broadband noise bumps near 20 MHz and 10 MHz are unexpectedly found, and contribute about 200 as of timing jitter [29].

Similar measurements performed on a pair of 200 MHz soliton erbium-doped fiber lasers allow estimation of the time constant for the decay of center frequency fluctuations at 17 ns. Also, by comparison with the well-established soliton timing jitter theory, the excess noise of the amplifier can be estimated. It is found that the excess noise must be approximately ten to account for the timing jitter of the soliton lasers. The origin of this excess noise is assumed to be from the fiber amplifier.

Finally, by synchronizing the 80 MHz stretched pulse erbium fiber laser with a Ti:Sapphire laser, which has been shown to have negligible timing jitter, the first absolute timing jitter measurements of such lasers have been conducted. From 10 kHz to 700 kHz, the integrated timing jitter is 2.2 fs rms, which is in good agreement with the heterodyne measurement between two identical fiber lasers.

6.4 Future Work toward Robust, Low-noise Ultrafast Lasers

As commercially and scientifically viable sources for low noise signal generation in analog-to-digital conversion and X-ray free electron lasers, ultrafast lasers must be robust, reliable and low-noise. The aforementioned measurements indicate that the excess noise of at least 10 is present in the laser amplifier. This excess noise should be systematically studied and reduced. It is believed that incomplete gain medium inversion leads to significant pulse re-absorption. Since spontaneous absorption is analogous to spontaneous emission, it

contributes noise in a similar way. Therefore, amplifier design is critical to achieving low noise performance.

Furthermore, the measurements clearly demonstrate that jitter performance depends on the mode-locking state in an unpredictable way. Robust, self-starting waveguide lasers incorporating a saturable absorber to initiate mode-locking must be pursued. SBR or SESAM mode-locked lasers can have a single, predictable mode-locking state for a given pump power.

Ultimately, for photonic analog-to-digital conversion, an integrated, waveguide-based, self-starting ultrafast laser is needed. Such lasers have typically been based on soliton mode-locking, which adds considerable cavity group velocity dispersion. This dispersion increases the timing jitter through the Haus-Gordon effect. Low-dispersion lasers integrated lasers should be investigated [100].

In addition, high-repetition rate integrated lasers with small waveguide mode field areas tend to have low pulse energy and long pulse durations. Both factors significantly degrade timing jitter performance. Also, as the repetition rate is increased, the pulse passes through the noisy amplifier more frequently. Thus, noise accumulates at a faster rate. Consider an integrated gigahertz laser with $1/10^{th}$ the pulse energy of a typical 100 MHz erbium fiber laser, 500 fs pulses (10 times longer), and 10 times the repetition rate. One expects a timing jitter 100 times worse than for the 50 fs, 100 MHz fiber laser. In comparison with the stretched pulse laser measurements, one can expect a timing jitter on the order of 200 fs rms. This analysis does not yet even account for the additional jitter due to the Gordon-Haus effect.

Very significant future work will be required to develop a low-noise, integrated ultrafast laser. Methods for increasing the pulse energy and decreasing the pulse duration will be necessary. Soliton theory provides a way forward. Soliton Area Theorem demands that there be a fixed relationship between the pulse energy and pulse duration (6.1). Pulse energy, E_p, can be increased if pulse duration, τ, is decreased, holding the waveguide

properties fixed. However, τ cannot be decreased forever, since pulse duration is ultimately limited by gain bandwidth to around 100 fs in erbium doped fiber. Further increases in pulse energy will require reduction of the effective non-linearity, γ. Increasing the dispersion, β_2 is not an attractive option since doing so only increases Gordon-Haus jitter. Thus, to reduce waveguide non-linearity, large mode area or air-core structures should be considered. Examples of such waveguides include large mode area phonic crystal fiber and air-core PCF.

$$E_p = \frac{2|\beta_2|}{|\gamma|\tau} \tag{6.1}$$

Achieving high repetition rates in integrated ultrafast lasers is not entirely straightforward, either. As the repetition rate is increased, the cavity length must shrink. However, erbium doped fiber gain is limited due to clustering effects inhibiting high doping concentrations [101]. Erbium-Ytterbium co-doping has allowed waveguide gain to be dramatically increased. However, pushing toward the desired repetition rates of 10 GHz to 100 GHz is still challenging, as a linear cavity must be only 10 cm to 1 cm long. Pulse interleaving as a means for increasing repetition rate should be investigated along with high-gain ytterbium-erbium co-doped fibers [102].

6.5 Coherent Pulse Synthesis

Coherent beam combining of independent ultrafast lasers has been pursued for the generation of short ultrafast pulses [5], [12], [13], [23]. Since the gain bandwidth of a single laser is always limited by the properties of the gain medium, a lower limit on the pulse duration exists.

Phase sensitive non-linear optics seeks a single-cycle optical pulse for experimental investigation of quantum and strong field atomic effects. To progress toward this goal, the synchronization of independent, ultrafast sources covering different portions of the near-

infrared band is demonstrated. A 7 fs pulse from a Ti:Sapphire laser (650 to 950 nm) is combined with an 8 fs pulse from a fiber supercontinuum (950 to 1200 nm) to generate a 4.7 fs pulse. The transform limit of the synthesized pulse is 4.2 fs.

The timing synchronization between the Ti:Sapphire laser and the fiber laser supercontinuum is achieved through active feedback. Pulse timing error is measured with a balanced cross-correlator with attosecond resolution, and fed back to two different actuators. First, a piezo mounted mirror inside the fiber laser cavity corrects for large timing fluctuations within a bandwidth of 18 kHz. A residual timing jitter of 2.2 fs rms remains [100 Hz, 700 kHz]. Secondly, the residual timing jitter is reduced to 280 as rms via a high speed, waveguide phase modulator placed outside of the laser cavity. The phase modulator adds negligible phase noise, which is readily removed by the fast acousto-optic phase lock, regardless.

Carrier envelope phase synchronization between laser oscillators is measured optically with a balanced homodyne detector. Having a range of only $\pm\pi/2$ at a center frequency of 316 THz (950 nm), the locking bandwidth must be extremely high to suppress the phase fluctuations to within this range. Previous methods lack either the bandwidth or orthogonal control between timing and phase to synchronize the lasers with sub-cycle precision [5], [23].

A carrier envelope phase locking scheme incorporating an acousto-optic frequency shifter in feedback configuration is proposed and implemented to successfully lock the fiber supercontinuum to the Ti:Sapphire with sub-cycle precision. The AOFS is placed outside the fiber laser cavity, but before the amplifier and supercontinuum generation. Carrier enevelope phase fluctuations measured at the balanced homodyne detector are processed by a standard PID loop filter to command the frequency of a voltage controlled oscillator. Next, the VCO signal is amplified before driving the AOFS. The AOFS in turn shifts the center frequency of the entire optical spectrum directly out of the fiber laser, which has an optical

bandwidth of 60 nm. This method provides phase stabilization to 200 mrad rms [100 Hz, 5 MHz] with a closed loop feedback bandwidth of 450 kHz.

The synthesized pulse is characterized with both Frequency Resolved Optical Gating (FROG) and Two-dimensional Spectral Shearing Interferometry (2DSI) [92], [99]. FROG measurements verify the temporal and spectral coherence by showing a reduction in pulse duration when timing and phase locks are enabled. Pulse duration is confirmed to reduce from 8 fs to 5 fs, while the FROG spectrogram confirms the broadening of the second harmonic bandwidth.

However, the FROG technique cannot readily retrieve single-cycle pulses [99]. For this reason, we turn to 2DSI for temporal characterization, since it is immune to spectral filtering from the non-linear optics and spectrometer. 2DSI is also a direct measurement of optical group delay, and does not depend on the reliability and convergence of iterative decovolution algorithms. 2DSI measurements of the combined output yield a pulse duration of 4.7 fs, with a transform limit of 4.2 fs [650 to 1200 nm]. The transform limit of the entire compressible spectrum, from 650 to 1400 nm would be 3.5 fs—nearly single cycle.

6.6 Future Work toward Single-Cycle Synthesis

The duration of a single period of an electromagnetic wave with a wavelength of 1000 nm is 3.33 fs in vacuum. With further refinement of the dispersion compensation of the fiber supercontinuum, the synthesized pulse can be compressed to the transform limit of 3.5 fs. In this work, the portion of the supercontinuum from 950 nm to 1200 nm is compressed with an F2 glass prism compressor. However, the third order dispersion of such a compressor becomes extremely high beyond 1200 nm, limiting the realized pulse duration. Alternatively, an SF10 glass prism compressor achieves better compression over most of the bandwidth, but still fails to compress the spectrum below 1050 nm.

Ultimately, a better technique for pulse compression is required to get closer to single-cycle duration. More sophisticated devices, such as a deformable mirror, should be added to the prism compressor to eliminate the remaining higher order dispersion. For instance, a deformable mirror could replace the end mirror of the prism compressor to provide fine adjustment of the spectral group delay with minimal loss.

7 Appendix A: Ultrafast Frequency Combs

The derivation of the frequency comb of the ultrafast laser is summarized here from the literature [27], [88]. By analyzing the frequency comb with soliton perturbation theory upon the H.A. Haus Master Equation governing the soliton mode-locked laser, we shall gain an understanding of how to control the comb.

First, consider the H.A. Haus Master Equation governing the soliton laser, which is a form of the Non-linear Schrödinger equation (7.1) [103].

$$T_R \frac{\partial A(T,t)}{\partial T} = \left[(g-l) + D_g \frac{\partial^2}{\partial t^2} + \delta |A|^2 + jD_2 \frac{\partial^2}{\partial t^2} - j\gamma |A|^2 \right] A(T,t) + L_{pert} \tag{7.1}$$

For the Master Equation (ME), the change in pulse amplitude envelope, A(t), per round-trip, T, is determined by linear and non-linear operators applied to the pulse every round-trip period, T_R. Also, we include a perturbation term, L_{pert}, which includes all perturbations in pulse amplitude and phase. Linear operators include the cavity gain, g, and loss, l, plus the net group velocity dispersion, D_2. Also, gain filtering, which captures the limited gain bandwidth of the amplifier, is set by D_g. The curvature of the gain spectrum is set by the average gain g over the gain bandwidth, Ω_g (7.2) [104].

$$D_g = \frac{g}{\Omega_g^2} \tag{7.2}$$

In addition, non-linear operators, which is to say the response depends on the intensity of the pulse itself, are self-phase modulation coefficient Υ and slow saturable absorber

coefficient, δ. Finally, we simplify the expression by consolidating all irreversible operators in D_{irrev}.

The saturable absorption provides an intensity dependent loss for which more intense pulses experience less loss. In this way, the ME supports a short pulse, stead-state solution which minimizes round-trip losses. However, it is not enough to have only saturable absorption to achieve an ultrafast pulse solution. This is because SPM and dispersion act to distort the pulse, and their effects must be somehow controlled. One possibility is to find a solution for which the intensity dependent phase of SPM can exactly cancel the linear dispersive effects.

7.1 The Ideal Frequency Comb

It has been known for some time that there exists a stable solution, known as the soliton, which may propagate in a dispersive medium without temporal distortion. This was first observed in 1884 for water waves by J.S. Russell [105]. A similar effect in dielectric optical fibers was later observed in 1973 for picoseconds pulse propagation [106].

These solitary pulses require an anomalous dispersion medium, which is to say that group velocity *increases* with increasing frequency. Therefore, blue waves propagates faster than red waves under anomalous dispersion. This means that a pulse disperses such that the high frequency components run ahead of the low frequency components, giving rise to chirp. A positive Kerr non-linearity can exactly compensate for anomalous dispersion, provided the pulse shape is correct. Under this circumstance, and without perturbation, the ME supports a sech steady-state solution, which is the fundamental soliton (7.3).

$$a_s(t,T) = A_0 \operatorname{sech}\left(\frac{t}{\tau}\right) e^{-j\phi_0 \frac{T}{T_R}} \tag{7.3}$$

The fundamental soliton has a field envelope amplitude A_0 and a pulse-width τ. In addition, the soliton has a non-linear phase ϕ_0 (7.5). It is also important to note that the "area" of the

soliton is fixed by the dispersion and non-linearity. This is known as the soliton area theorem, (7.4).

$$\int_{-\infty}^{\infty} |A(z,t)|dt = (A_0\tau)^2 = \frac{2|D_2|}{\gamma} \tag{7.4}$$

$$\phi_0 = \frac{1}{2}\gamma A_0^2 \tag{7.5}$$

Of course, since the pulse travels through the laser at repetition period T_R, the resulting ultrafast pulse train is finally given by (7.6).

$$A(t) = \sum_{m=-\infty}^{\infty} a(t, T = mT_R)\exp\left(j\left(\omega_c[t - mT_R] + m\Delta\phi_{CEO}\right)\right) \tag{7.6}$$

$$\Delta\phi_{CEO} = 2L\omega_c\left(1/v_g - 1/v_p\right) - \phi_0 \tag{7.7}$$

As for the ultrafast pulse train, each pulse is modulated by the carrier frequency ω_c and the phase slip. The phase slip comes about by the difference in group and phase velocity. One can imagine that if the carrier wave moves at a different rate than the propagation of the pulse, the phase underneath the pulse envelope will be different for every cavity round-trip. This net phase slip per round-trip, known as the carrier envelope offset (CEO), is proportional to the difference in inverse group and phase velocity (7.7).

From the Fourier transform property (2.3), we know that a temporal phase ramp exp(jϕt) leads to a frequency shift of the entire optical spectrum. We also know from (7.8) that a series of periodic complex exponentials in the time domain forms a frequency comb in the optical spectrum. Therefore, the Fourier transform of the unperturbed pulse train is given by (7.9).

$$\sum_{m=-\infty}^{\infty} \exp(j2\pi m\beta) = \sum_{n=-\infty}^{\infty} \delta(\beta - 2\pi n) \tag{7.8}$$

$$A(\omega) = a(\omega - \omega_c)\omega_R \sum_{m=-\infty}^{\infty} \delta\left(\omega - \left(\frac{\Delta\phi_{CEO}}{T_R} + n\omega_R\right)\right) \tag{7.9}$$

For the frequency comb, $\omega_R = 2\pi/T_R$ is the comb spacing. Note that the frequency comb consists of a set of pure harmonic signals separated by the comb spacing—all of which are equally shifted by an offset from zero frequency, known as the f_{CEO}. Therefore, the f_{CEO}, which is the frequency shift of the entire comb, is given by (7.10).

$$f_{CEO} = \frac{\Delta\phi_{CEO}}{2\pi T_R} = f_c\left(1 - \frac{v_g}{v_p}\right) - \frac{\gamma A_0^2}{4\pi} f_R \tag{7.10}$$

Note, that the frequency comb has only two degrees of freedom, the comb spacing, given by ω_R, and the comb offset from DC, f_{CEO}. In principle, by independently controlling these two parameters, we may have complete control over all frequencies in the frequency comb. In practice, the paramount challenge is to achieve truly independent and orthogonal control of both parameters.

7.1.1 Control of Frequency Combs

Typically, control of the f_{CEO} has been achieved through pump power modulation. By changing the pump power, and therefore the laser gain, the steady-state pulse energy can be varied. This phenomenon can be understood by considering the interaction of pulse energy upon soliton phase and group velocity.

Recall that the soliton energy w is given by (7.11), which we can substitute into (7.10).

$$w_0 = \int_{-\infty}^{\infty} \left|A(z,t)\right|^2 dt = 2A_0^2\tau \tag{7.11}$$

Therefore, a fractional change in pulse energy leads to a corresponding fractional change in the soliton phase slip, and thus the f_{CEO}.

$$\Delta f_{CEO}\big|_{\Delta v_g = 0} = \frac{\Delta\phi_0}{2\pi} f_R = \frac{\gamma \Delta w_0}{8\pi\tau} f_R = \frac{\gamma A_0^2}{4\pi}\frac{\Delta w}{w_0} f_R \tag{7.12}$$

And so we can see that by changing the pulse energy, we can vary the soliton phase per round-trip, ϕ_0, in order to shift the f_{CEO}. While this is indeed the case, one must also consider that self-steepening leads leads to a change in group velocity with a change in pulse energy. This change in group velocity manifests as a change in repetition rate. Although self-steeping is not included in the Master Equation, the effect on the pulse timing can be incorporated by way of soliton perturbation theory—which we will not cover in this context. Instead, it has been shown that the timing shift per round-trip from self-steeping is (7.13).

$$\Delta t(T) = \frac{\gamma A_0^2}{2\pi f_c} \tag{7.13}$$

Which yields a change in repetition rate of (7.14).

$$\Delta f_R = -f_R^2 \Delta t(T) = -\frac{\gamma A_0^2}{2\pi f_c} f_R^2 \tag{7.14}$$

Therefore, due to the action of self-steeping, it is impossible to control only the phase slip without altering the pulse timing, or repetition rate. This phenomenon is of great concern for the active synchronization of independent ultrafast lasers, because orthogonal control of pulse phase and timing is required.

8 Appendix B: Stretched Pulse Fiber Laser Schematic

A schematic for the 80 MHz stretched pulse, additive pulse mode-locked, erbium-doped fiber laser is shown in this appendix, FIG. 67. This laser is found to have quite exceptional performance for an erbium fiber laser, in terms of timing jitter, optical bandwidth and stability of mode-locking. As a stretched pulse laser, the cavity should have about zero net group velocity dispersion. This places a requirement on the ratio of the lengths of SM fiber and normal dispersion small core gain fiber in the cavity. Additionally, the WDM has a few tens of centimeters of 6 μm core fiber, with less anomalous dispersion than Corning SMF-28e. The intracavity isolator is a double stage, polarization insensitive model with low PMD. If a low PMD fiber coupled isolator is not available, it is better to use a polarization sensitive free space isolator with no PMD.

This laser incorporates the standard additive pulse mode-locking (APM) design for passively mode-locked fiber lasers, consisting of a set of wave plates and a polarizing beam splitter / output coupler. Typical output average power is 25 mW to 35 mW, depending on the pump current. Typical output bandwidth from the rejection port of the PBS is 60 nm to 80 nm. The pump diode is a fiber Bragg grating stabilized, 976 nm, 660 mW JDS Uniphase low-noise pump diode. Typicall diode current is 700 mA to 1000 mA, as multiple pulsing tends to occur for pump currents exceeding 1000 mA.

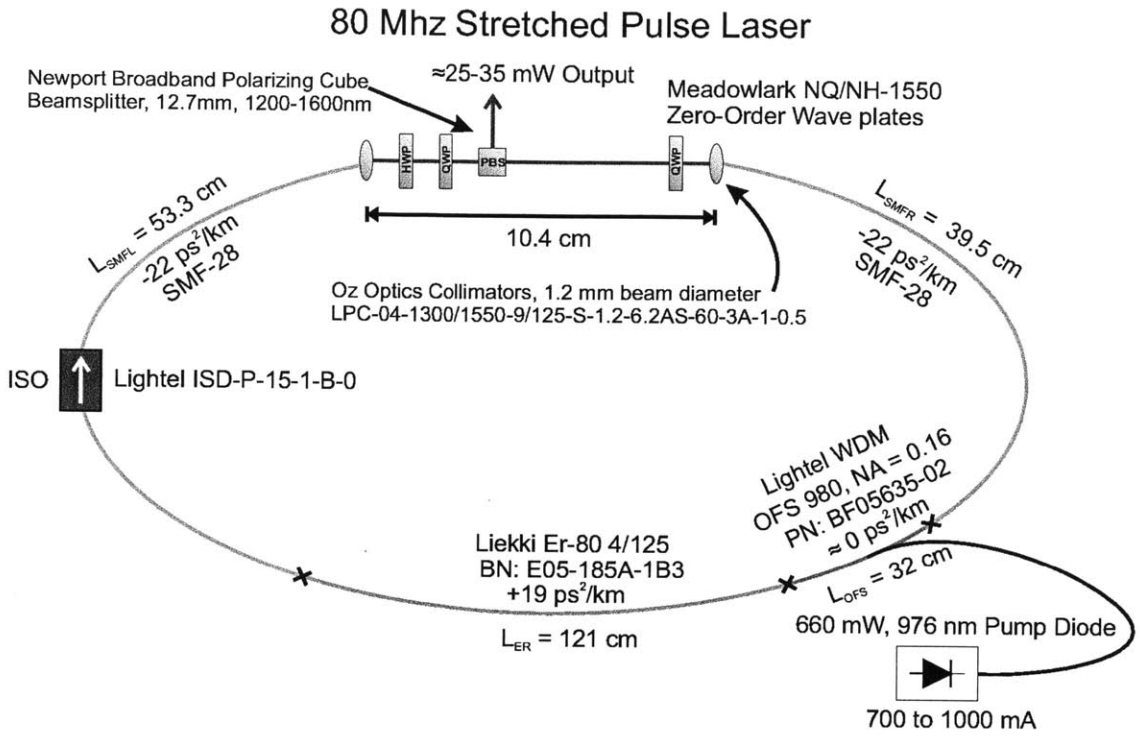

FIG. 67. Schematic of 80 MHz erbium-doped stretched pulse fiber laser.

9 Appendix C: High-performance, High-voltage Piezo or Waveguide EOM Op-amp Driver

The following circuit in FIG. 68 was implemented for driving small, fast piezoelectric stacks and later modified to drive the waveguide Lithium Niobate EOM / phase shifter. This circuit is based on a high-current (200 mA), high-speed Apex Microtechnology PA98 op-amp. The high voltage power supply is an Ultravolt supply. Although only single-rail operation is needed, a -28 V linear supply was included to simplify the op-amp circuit and improve performance near zero volts. Adequate heat sinking and ventilation should be provided for the op-amp. Also, the proper diode and tranzorb protection circuitry should not be omitted, since the PA98 is a fragile and expensive IC.

This circuit is based on the standard designs explained in the Apex Microtechnology application notes for driving capacitive loads. The component values shown are chosen for driving small, fast piezos with low capacitance. For instance, the PI PICMA 3x3x2 mm ceramic piezo stack with 50 nF capacitance.

Piezo (PI PICMA 3x3x2 mm) or 50Ω EOM Driver

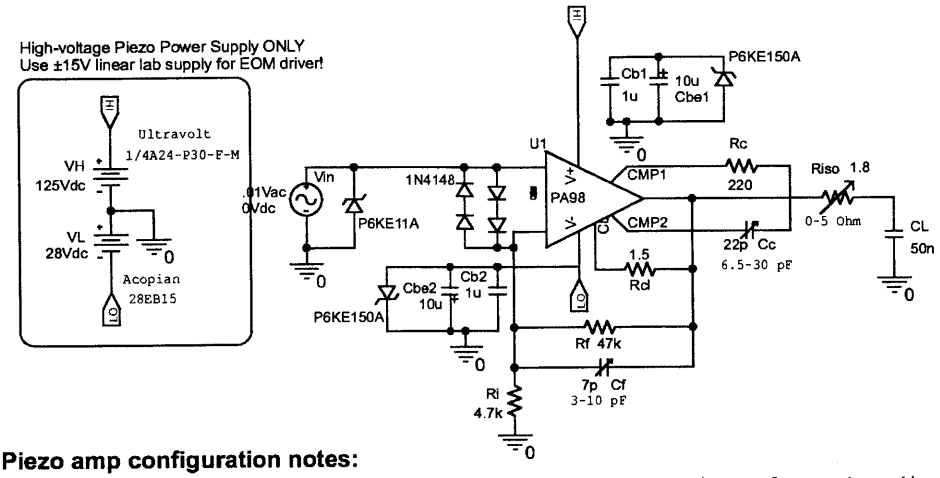

Piezo amp configuration notes:

Note: Riso, compensation capacitor Cc and feedback capacitor Cf must be adjusted for a particular piezo. To adjust, observe the step response with a square wave input. Start with Riso similar to 1-2 Ohms. Increase Cc until op amp is stable, then increase Cf to dampen overshoot and oscillations. Adjustments are not completely orthogonal.

Note 2: Recommended power supply is the Ultravolt 1/8A24-P30-F-M with 240 mA output, however the 1/4A20 was used with a potentiometer to adjust the output voltage to 125 V. Do not attempt to use two positive polarity Ultravolts to obtain a dual supply voltage. If a large negative rail is desired, use only a negative -N30- Ultravolt.

Modifications for driving 50Ω waveguide Lithium Niobate EOM:

Several components must be modified or omitted for driving a EOM with 50 Ohm load, instead of a capacitive piezo load. Eliminate following components: Riso, Cf. Change gain of amplifier from ~10x to 1x by eliminating Ri and setting Rf to zero. Also, do not use a high voltage supply!

FIG. 68. Schematic of high-performance, high-voltage piezo or low-voltage EOM phase shifter driver.

10 Appendix D: Ultrafast Pulse Propagation Simulation in Long Fiber Links

The MATLAB code for ultrafast pulse propagation simulation in optical fiber is provided here for reference. The simulation implements the split-step method with adaptive spatial step-size algorithm. Adaptive step size is critical for simulating long fiber links, where significant non-linear effects occur at the beginning and end of the fiber link. Also, fourth order Runge-Kutta method is implemented for the non-linear operators, self-phase modulation, self-steepening, and Raman scattering. This code was tested with MATLAB versions 2007 through 2011. The accuracy of the results was verified against *Nonlinear Fiber Optics* by Agarwal [54].

The core routines consist of the following .m files: **dAdZ.m, fdiff.m, nlsim_script.m, nlsim.m, gen_pulse.m**. Additionally, the **pulse_EFL.m** and **fiber_smf28.m** scripts contain the input pulse parameters and specifications for Corning SMF-28, respectively. In particular, pulse_EFL.m sets the initial pulse which is propagated down the fiber link. Note, the progressbar.m routine is non-essential, and only implements a progress bar with expected wait time.

The simulation begins execution at **nlsim_scrip.m**, which loads the initial pulse and fiber parameters from **pulse_EFL.m** and **fiber_smf28.m**. Next, the simulation calls **gen_pulse.m** to construct the initial pulse from the requested parameters.

After all setup procedures are conducted, the main simulation loop begins. In this case, the simulation computes various parameters for different input pulse energies.

Regardless, **nlsim_scrip.m** calls **nlsim.m**, which implements the actual split-step pulse propagation routine. The split-step routine in **nlsim.m** calls **dAdZ.m**, which contains the nonlinear operators to be solved. Differentiation is done in the frequency domain using **fdiff.m**, since this has been found to be the fastest method in MATLAB.

10.1 dAdz.m: Nonlinear operators

```
% dAdz.m: Non-linear portion of differential equation. This is solved by
% the numerical integration. For example, Runga-Kutta O(h^4)
function f = dAdz(u, gamma, Tr, omega0,omega)
    U = abs(u).^2;
    Uu = U.*u;

    %       SPM              S.S.                  Raman
    f =  -i*gamma*Uu + gamma/omega0*fdiff(Uu,omega)
i*gamma*Tr*fdiff(U,omega).*u;
end
```

10.2 fdiff.m: Frequency domain derivative

```
function div = fdiff(f, omega)
    div = ifft(-i*omega.*fft(f));
end
```

10.3 pulse_EFL.m: Initial pulse input to simulation

```
% The FWHM of the initial input pulse to fiber
t0_FWHM = 1*.167;
% Laser repetition rate in Hz -> THz
frep = 200e6*1e-12;
% Average, or CW power in Watts
Pcw = 30e-3;
% The shape of the pulse (gaussian of hyperbolic secant)
shape = SECH_PULSE;
```

10.4 fiber_smf28.m: Parameters for Corning SMF-28

```
% SMF-28e Parameters
% SMF-28 from Corning spec sheet and various journal sources:

% Center wavelength for SMF-28 dispersion calculations
```

```
lambda0_ZD = 1.312; % um
% dispersion slope about the zero dispersion point.
So = .092; % ps/(nm^2*km)
% ps/(nm*km) -> ps/(um*um)
D = So/4*(lambda0*1e3 - (lambda0_ZD*1e3)^4/(lambda0*1e3)^3)*1e-6;
%ps/(um*um)
beta2 = -lambda0^2/(2*pi*c)*D; % ps^2/um
% ps/(km*nm^2)->ps/(um*um^2) (from Hakimi paper)
D2 = .076*1e-3;
beta3 = (lambda0^3/(2*pi^2*c^2))*(D + (lambda0/2)*D2);
% (from Serkland and Kumar paper) Non-linear coefficient of fiber (1/W/m)
gamma = 1.5e-9; % 1/(W*um)
% Raman time
% 3 fs for silica fiber from Agarwal pg. 180 3rd edition
Tr = 3e-3;
% Fiber length
l = 100e6; % 1 m
```

10.5 nlsim_script.m: Master script from which program execution begins

```
% Non-linear pulse propagation master script for NLSE.
% Units: ps, um, Watts (J/s)

% Janitorial and administrative tasks
close all
clear all

% Flags and switches
% Enable additional debugging plots and tests
debug = 1;
% Plot the results?
doplot = 0;
% Monitor function calls for performance enhancement?
prof = 0;

% Constants
global SECH_PULSE;
SECH_PULSE = 1;
global GAUS_PULSE;
GAUS_PULSE = 2;

% Speed of light in vacuum
global c;
c = 3e8*1e-6; % um/ps

% Load the initial pulse
run('pulses/pulse_EFL.m')
% Load fiber parameters
run('fiber/smf28/fiber_smf28.m')

% Numerical Parameters
```

```
% number of points for frequency and time domain
n = 2^11;
% Number of sptial, propagation steps, intitial guess
steps = 2^7;
% How large should the time window be as a multiple of the FWHM?
tau_mult = 1000;

display('-->NLSEsim 1.2, By Jonathan A. Cox. Copyright 2011. All rights
reserved<--');
%%%%%%%%%%%%%%%%%%%%%%%%%% SIMULATION
%%%%%%%%%%%%%%%%%%%%%%%%%%%%%%%%%%%%
if prof == 1
    profile on
end

% Loop parameters
prechirp = 0*(125)^2*1e-6; % fs^2 --> ps^2
k = 20;
Pcw = 1e-3*linspace(.01,40,k);
doBoc = 0;
Mc = zeros(1,k);
tau_x = zeros(1,k);
stopped = 0; % Did the user terminate the simulation early??
for j=1:k
    stopBar = progressbar(j/k,0);
    if (stopBar)
        stopped = 1;
        break;
    end

    % Generate initial pulse
    [ui t f omega omega0] = gen_pulse(prechirp, t0_FWHM, shape, frep,
Pcw(j), tau_mult,lambda0, n);

    % Run the actual NLSE simulation for SMF-28e
    [uf_smf1 u_ev_smf1 z_smf1 err] = nlsim(beta2, beta3, gamma, Tr,
1,steps, doplot,ui,t,f,omega,omega0, debug);
    [uf_dcf1 u_ev_dcf1 z_dcf1 err] = nlsim(-7*beta2, -7*beta3, 5.6e-9, Tr,
1/7,steps, doplot,uf_smf1,t,f,omega,omega0, debug);

    % Compute timing error from single-pass through link
    [Mc1(j), tau_x1(j), P1, P2] = bxcorr(t, sqrt(abs(ui).^2),
sqrt(abs(uf_dcf1).^2), doplot, doBoc);

    [uf_dcf2 u_ev_dcf2 z_dcf2 err] = nlsim(-7*beta2, -7*beta3, 5.6e-9, Tr,
1/7,steps, doplot,uf_dcf1,t,f,omega,omega0, debug);
    [uf_smf2 u_ev_smf2 z_smf2 err] = nlsim(beta2, beta3, gamma, Tr,
1,steps, doplot,uf_dcf2,t,f,omega,omega0, debug);

    % Compute timing error from round-trip through link
    [Mc2(j), tau_x2(j), P1, P2] = bxcorr(t, sqrt(abs(ui).^2),
sqrt(abs(uf_smf2).^2), doplot, doBoc);
end
```

```
if prof == 1
    profreport('nlsim');
    profile clear
end

if ~stopped
    % Plotting and analysis routines may be placed here
end
```

10.6 nlsim.m: Adaptive step size, Runge-Kutta, pulse propagation routine

```
function [u u_ev z err] = nlsim(beta2, beta3, gamma, Tr, l,steps,
doplot,ui,t,f,omega,omega0, debug)

% Threshold above which fractional power error is considered too great.
kErrorWarn = 1e-5;

if debug == 1
    tic
end

% Set error flag to false
err = 0;
Perror_max = 1e-6;
Perror_min = 1e-8;
kErr_hits = 3;

% Constants
SECH_PULSE = 1;
GAUS_PULSE = 2;

%%%%%%%%%%%%%%%%%%%%%%%%% PARAMETERS
%%%%%%%%%%%%%%%%%%%%%%%%%%%%%%%%%%%%
% Numerical Parameters
dz = l/steps;       % propagation step size (m)
n_deci = 1;
n = length(t);
dt = t(2)-t(1);

% Array for storing snap-shots of pulse every recording interval
u_ev = zeros(n, 2);
% Store the initial pulse to the snap-shot
u_ev = ui.';

% Set the initial pulse
u = ui;
u_prev = ui; % Preload previous iteration's pulse with the intial pulse

% Shift the frequency domain to match MATLAB's shifted domain
```

```
omega = fftshift(omega);

% Split-Step Method: Propagate through the fiber
done = 0;
k = 1;
z = [0]; % Stores a list of pulse positions for the evolution plot
z_cur = 0; % Set the current value of z to one step
err_hits = 0;
while z_cur ~= 1
    % Check if dz should be shortened so last iter does not over step
    if (z_cur+dz) > 1
        dz = 1-z_cur;
        done = 1;
    end

    % SYMMETRIZED SPLIT-STEP METHOD
    % Dispersion (1st half)
    D_half = exp((-i/2*beta2*omega.^2 - i/6*beta3*omega.^3)*dz/2);
    u = ifft(D_half.*fft(u));

    % Non-linear step using Runga-Kutta 4th order
    k1 = dAdz(u, gamma, Tr, omega0,omega);
    u_half2 = u + k1*dz/2;
    k2 = dAdz(u_half2, gamma, Tr, omega0,omega);
    u_half3 = u + k2*dz/2;
    k3 = dAdz(u_half3, gamma, Tr, omega0,omega);
    u_full = u + k3*dz;
    k4 = dAdz(u_full, gamma, Tr, omega0,omega);
    u = u + dz/6*(k1 + 2*k2 + 2*k3 + k4);

    % Dispersion (2nd half)
    u = ifft(D_half.*fft(u));

    % Compute error of this iteration
    E0 = trapz(abs(u_prev).^2)*dt;
    Ef = trapz(abs(u).^2)*dt;
    Perror = abs(Ef-E0)./E0;

    % Decide if step size should be reduced, increased, or if it is OK.
    if Perror > Perror_max
        err_hits = 0;
        dz = dz/2; % Cut step size in half
        u = u_prev; % re-do the last propagation step
        fprintf('-');
    elseif (Perror < Perror_min) && (done == 0) && (err_hits == kErr_hits)
        % Only increase step size if we have run three low-error steps in
a row
        dz = 2*dz;
        u = u_prev;
        fprintf('+');
    else % A successful propagation step
        % But if error is very low, increase hit counter
        if Perror < Perror_min
```

```
            err_hits = err_hits + 1;
        end
        % Store the last pulse
        u_prev = u;
        z_cur = z_cur + dz;
        k = k+1;
        %fprintf('=');
        if doplot == 1
            % Save a snap-shot of the pulse
            if (mod(k,n_deci) == 0)
               z = [z z_cur];
               u_ev = [u_ev u.'];
            end
        end
    end
end

% Save a snapshot of the final pulse, if it was not already done
if (doplot == 1) && (z(end) ~= z_cur)
    z = [z z_cur];
    u_ev = [u_ev u.'];
end

% Shift the frequency domain back to normal
omega = ifftshift(omega);

if debug == 1
    fprintf('\n');
    disp(['Iterations: ' num2str(k)]);

    % Compute energy loss as an estimation of error
    E0 = trapz(abs(ui).^2)*dt;
    Ef = trapz(abs(u).^2)*dt;
    % This is a check to make sure the 1/fs/n conversion factor is correct
    Efreq = trapz(abs(fftshift(fft(ui))).^2)*dt/n;
    Perror = abs(Ef-E0)./E0;
    display(['Pulse energy = ' num2str(E0, 2), ' pJ, ' 'Power error = '
num2str(Perror, 2)]);
    if Perror > kErrorWarn
        display('***Warning: excessive numerical error!');
    end
    TBPi = fwhm(abs(ui).^2,t)*fwhm(abs(fftshift(fft(ui))).^2,f);
    TBPf = fwhm(abs(u).^2,t)*fwhm(abs(fftshift(fft(u))).^2,f);
    display(['TBPi = ' num2str(TBPi, 3), ', TBPf = ' num2str(TBPf, 3)]);

    toc
end

end
```

10.7 gen_pulse.m: Generate a gaussian or sech pulse

```
function [ui t f omega omega0] = gen_pulse(prechirp, t0_FWHM, shape, frep,
Pcw, tau_mult, lambda0, n)
global SECH_PULSE;
global GAUS_PULSE;

% Speed of light in vacuum
c = 3e8*1e-6; % um/ps

% Pulse Parameters
if shape == SECH_PULSE
    fwhm_ratio = 2*log(1+sqrt(2)); % fwhm_ratio = tau_fwhm/tau
elseif shape == GAUS_PULSE
    fwhm_ratio = 2*sqrt(log(2)); % The ratio of FWHM:sigma
else
    display('Error 1: Invalid pulse shape.\n');
    return;
end

tau = t0_FWHM/fwhm_ratio;

% Frequency and time grid
t_range = .5*tau_mult*t0_FWHM;          % Time domain range
t = linspace(-t_range, t_range, n);     % Time axis
dt = t(2)-t(1);                          % Time step
fs = 1/dt;                               % Sampling frequency
% Frequency grid (linspace has a chirp!)
domega = 2*pi/n*fs;
omega = [-2*pi*fs + (((n/2):(n-1))*domega), (0:(n/2-1))*domega];
% Compute the wavelength vector for plotting purposes
f = omega/2/pi;
omega0 = 2*pi*c/lambda0;

% Calculate the pulse
if shape == SECH_PULSE
    ui = sech(t/tau);
elseif shape == GAUS_PULSE
    %Raman test
    ui = exp(-t.^2/(2*tau^2));
end

% Scale pulse so that the pulse energy is correct
Ef = Pcw/(frep*1e12);   % Requested pulse energy
Ei = trapz(abs(ui).^2)*dt*1e-12; % initial pulse energy before scaling
ui = ui.*sqrt(Ef/Ei); % Scale amplitude such that pulse energy is correct

% Prechirp pulse
D = exp(-i/2*prechirp*fftshift(omega).^2);
```

```
ui = ifft(D.*fft(ui));

end
```

11 References

[1] "The impact of frequency combs," *Nature Photonics*, vol. 5, pp. 193-193, Apr. 2011.

[2] Jun Ye, H. Schnatz, and L. W. Hollberg, "Optical frequency combs: From frequency metrology to optical phase control," *IEEE Journal of Selected Topics in Quantum Electronics*, vol. 9, pp. 1041-1058, Jul. 2003.

[3] D. J. Jones, "Carrier-Envelope Phase Control of Femtosecond Mode-Locked Lasers and Direct Optical Frequency Synthesis," *Science*, vol. 288, no. 5466, pp. 635-639, Apr. 2000.

[4] T. M. Fortier et al., "Generation of ultrastable microwaves via optical frequency division," *Nature Photonics*, vol. 5, pp. 425-429, Jun. 2011.

[5] J. Kim, "Toward single-cycle optical pulses," Massachusetts Institute of Technology, Cambridge, MA, 2004.

[6] J. Kim, M. J. Park, M. H. Perrott, and F. X. Kärtner, "Photonic subsampling analog-to-digital conversion of microwave signals at 40-GHz with higher than 7-ENOB resolution," *Optics Express*, vol. 16, no. 21, p. 16509, Oct. 2008.

[7] V. S. Reinhardt, "A review of time jitter and digital systems," pp. 38-45.

[8] R. Paschotta, "Noise of mode-locked lasers (Part I): numerical model," *Applied Physics B*, vol. 79, no. 2, May 2004.

[9] J. Kim, J. A. Cox, J. Chen, and F. X. Kartner, "Drift-free femtosecond timing synchronization of remote optical and microwave sources," *Nat Photon*, vol. 2, no. 12, pp. 733-736, Dec. 2008.

[10] J. Kim, "LARGE-SCALE TIMING DISTRIBUTION AND RF-SYNCHRONIZATION FOR FEL FACILITIES," presented at the FEL, 2004, pp. 339-342.

[11] L. Qin et al., "Compact temperature-compensating package for long-period fiber gratings," *Optical Materials*, vol. 14, pp. 239-242, Jul. 2000.

[12] G. Krauss et al., "Synthesis of a single cycle of light with compact erbium-doped fibre technology," *Nature Photonics*, vol. 4, no. 1, pp. 33-36, Dec. 2009.

[13] T. R. Schibli et al., "Toward single-cycle laser systems," *IEEE Journal of Selected Topics in Quantum Electronics*, vol. 9, no. 4, pp. 990-1001, Jul. 2003.

[14] E. Goulielmakis et al., "Single-Cycle Nonlinear Optics," *Science*, vol. 320, pp. 1614-1617, Jun. 2008.

[15] Y. Wu and X. Yang, "Carrier-envelope phase-dependent atomic coherence and quantum beats," *Physical Review A*, vol. 76, Jul. 2007.

[16] C. Zhang, X. Song, W. Yang, and Z. Xu, "Carrier-envelope phase control of carrier-waveRabi flopping in asymmetric semiparabolicquantum well," *Optics Express*, vol. 16, p. 1487, 2008.

[17] I. Christov, M. Murnane, and H. Kapteyn, "High-Harmonic Generation of Attosecond Pulses in the 'Single-Cycle' Regime," *Physical Review Letters*, vol. 78, pp. 1251-1254, Feb. 1997.

[18] A. Sell, G. Krauss, R. Scheu, R. Huber, and A. Leitenstorfer, "8-fs pulses from a compact Er:fiber system: quantitative modeling and experimental implementation," *Optics Express*, vol. 17, no. 2, p. 1070, Jan. 2009.

[19] S.-W. Huang et al., "High-energy pulse synthesis with sub-cycle waveform control for strong-field physics," *Nature Photonics*, vol. 5, pp. 475-479, Jul. 2011.

[20] J. Sun and D. T. Reid, "Coherent ultrafast pulse synthesis between an optical parametric oscillator and a laser," *Optics Letters*, vol. 34, p. 854, Mar. 2009.

[21] J. H. Sun, B. J. S. Gale, and D. T. Reid, "Composite frequency comb spanning 0.4-2.4μm from a phase-controlled femtosecond Ti:sapphire laser and synchronously pumped optical parametric oscillator," *Optics Letters*, vol. 32, p. 1414, 2007.

[22] T. I. Ferreiro, J. Sun, and D. T. Reid, "Locking the carrier-envelope-offset frequency of an optical parametric oscillator without f–2f self-referencing," *Optics Letters*, vol. 35, p. 1668, May 2010.

[23] R. K. Shelton, "Phase-Coherent Optical Pulse Synthesis from Separate Femtosecond Lasers," *Science*, vol. 293, no. 5533, pp. 1286-1289, Aug. 2001.

[24] S. Koke, C. Grebing, H. Frei, A. Anderson, A. Assion, and G. Steinmeyer, "Direct frequency comb synthesis with arbitrary offset and shot-noise-limited phase noise," *Nature Photonics*, vol. 4, no. 7, pp. 462-465, May 2010.

[25] M. Y. Sander, E. P. Ippen, and F. X. Kärtner, "Carrier-envelope phase dynamics of octave-spanning dispersion-managed Ti: sapphire lasers," *Optics Express*, vol. 18, p. 4948, Feb. 2010.

[26] L. Matos, "Octave-spanning lasers for optical metrology applications," MIT, 2006.

[27] L. Matos, O. D. Mücke, J. Chen, and F. X. Kärtner, "Carrier-envelope phase dynamics and noise analysis in octave-spanning Ti:sapphire lasers," *Optics Express*, vol. 14, no. 6, p. 2497, 2006.

[28] T. Wilken, "Low Phase Noise 250 MHz Repetition Rate Fiber fs Laser for Frequency Comb Applications," presented at the CLEO, Baltimore, Maryland, 2007.

[29] J. A. Cox, A. H. Nejadmalayeri, J. Kim, and F. X. Kärtner, "Complete characterization of quantum-limited timing jitter in passively mode-locked fiber lasers," *Optics Letters*, vol. 35, no. 20, p. 3522, Oct. 2010.

[30] A. H. Nejadmalayeri, F. N. C. Wong, T. D. Roberts, P. Battle, and F. X. Kärtner, "Guided wave optics in periodically poled KTP: quadratic nonlinearity and prospects for attosecond jitter characterization," *Optics Letters*, vol. 34, no. 16, p. 2522, Aug. 2009.

[31] U. Keller, K. D. Li, M. J. W. Rodwell, and D. M. Bloom, "Noise characterization of femtosecond fiber Raman soliton lasers," *IEEE Journal of Quantum Electronics*, vol. 25, no. 3, pp. 280-288, Mar. 1989.

[32] T. R. Schibli et al., "Attosecond active synchronization of passively mode-locked lasers by balanced cross correlation," *Optics Letters*, vol. 28, no. 11, p. 947, Jun. 2003.

[33] E. N. Ivanov, L. Hollberg, and S. A. Diddams, "Analysis of noise mechanisms limiting frequency stability of microwave signals generated with a femtosecond laser," in *Proceedings of the 2002 IEEE International Frequency Control Symposium and PDA Exhibition (Cat. No.02CH37234)*, New Orleans, LA, USA, pp. 435-441.

[34] A. Leitenstorfer, C. Fürst, and A. Laubereau, "Widely tunable two-color mode-locked Ti:sapphire laser with pulse jitter of less than 2 fs," *Optics Letters*, vol. 20, no. 8, p. 916, Apr. 1995.

[35] J. Kim, J. Chen, J. Cox, and F. X. Kärtner, "Attosecond-resolution timing jitter characterization of free-running mode-locked lasers," *Optics Letters*, vol. 32, no. 24, p. 3519, 2007.

[36] J. Kim et al., "Long-term femtosecond timing link stabilization using a single-crystal balanced cross correlator," *Optics Letters*, vol. 32, no. 9, p. 1044, 2007.

[37] I. Coddington et al., "Coherent optical link over hundreds of metres and hundreds of terahertz with subfemtosecond timing jitter," *Nature Photonics*, vol. 1, no. 5, pp. 283-287, May 2007.

[38] A. Oppenheim, *Signals and systems*, 2nd ed. Upper Saddle River N.J.: Prentice Hall, 1996.

[39] H. Byun, D. Pudo, J. Chen, E. P. Ippen, and F. X. Kärtner, "High-repetition-rate, 491 MHz, femtosecond fiber laser with low timing jitter," *Optics Letters*, vol. 33, no. 19, p. 2221, Sep. 2008.

[40] A. Bartels, S. A. Diddams, T. M. Ramond, and L. Hollberg, "Mode-locked laser pulse trains with subfemtosecond timing jitter synchronized to an optical reference oscillator," *Optics Letters*, vol. 28, no. 8, p. 663, Apr. 2003.

[41] L. A. Jiang, M. E. Grein, E. P. Ippen, C. McNeilage, J. Searls, and H. Yokoyama, "Quantum-limited noise performance of a mode-locked laser diode," *Optics Letters*, vol. 27, no. 1, p. 49, Jan. 2002.

[42] D. Hou, P. Li, C. Liu, J. Zhao, and Z. Zhang, "Long-term stable frequency transfer over an urban fiber link using microwave phase stabilization," *Optics Express*, vol. 19, no. 2, p. 506, Jan. 2011.

[43] R. K. Shelton et al., "Subfemtosecond timing jitter between two independent, actively synchronized, mode-locked lasers," *Optics Letters*, vol. 27, no. 5, p. 312, Mar. 2002.

[44] F. König and F. N. C. Wong, "Extended phase matching of second-harmonic generation in periodically poled KTiOPO[sub 4] with zero group-velocity mismatch," *Applied Physics Letters*, vol. 84, no. 10, p. 1644, 2004.

[45] R. Boyd, *Nonlinear optics*, 2nd ed. San Diego CA: Academic Press, 2003.

[46] J.-C. Diels and ScienceDirect (Online service), *Ultrashort laser pulse phenomena fundamentals, techniques, and applications on a femtosecond time scale*. Burlington, MA :: Academic Press,, 2006.

[47] F. N. C. Wong, J. H. Shapiro, and T. Kim, "Efficient generation of polarization-entangled photons in a nonlinear crystal," *Laser Physics*, vol. 16, no. 11, pp. 1517-1524, Nov. 2006.

[48] X. Ma, L. Liu, and J. Tang, "Timing jitter measurement of transmitted laser pulse relative to the reference using type II second harmonic generation in two nonlinear crystals," *Optics Express*, vol. 17, no. 21, p. 19102, Oct. 2009.

[49] K. Fradkin, A. Arie, A. Skliar, and G. Rosenman, "Tunable midinfrared source by difference frequency generation in bulk periodically poled KTiOPO[sub 4]," *Applied Physics Letters*, vol. 74, no. 7, p. 914, 1999.

[50] J. Lee, Y.-J. Kim, K. Lee, S. Lee, and S.-W. Kim, "Time-of-flight measurement with femtosecond light pulses," *Nature Photonics*, vol. 4, no. 10, pp. 716-720, Aug. 2010.

[51] G. Marra et al., "High-resolution microwave frequency transfer over an 86-km-long optical fiber network using a mode-locked laser," *Optics Letters*, vol. 36, no. 4, p. 511, Feb. 2011.

[52] S. M. Foreman, K. W. Holman, D. D. Hudson, D. J. Jones, and J. Ye, "Remote transfer of ultrastable frequency references via fiber networks," *Review of Scientific Instruments*, vol. 78, no. 2, p. 021101, 2007.

[53] E. P. Ippen, H. A. Haus, and L. Y. Liu, "Additive pulse mode locking," *Journal of the Optical Society of America B*, vol. 6, no. 9, p. 1736, Sep. 1989.

[54] G. Agrawal, *Nonlinear fiber optics*, 3rd ed. San Diego: Academic Press, 2001.

[55] *Optical Fiber Fusion Splicing*, vol. 103. Berlin/Heidelberg: Springer-Verlag, 2005.

[56] A. Galtarossa, *Polarization Mode Dispersion*. New York, NY: Springer Science Business Media, Inc., 2005.

[57] S. Yamashita, K. Hotate, and M. Ito, "Polarization properties of a reflective fiber amplifier employing a circulator and a Faraday rotator mirror," *Journal of Lightwave Technology*, vol. 14, no. 3, pp. 385-390, Mar. 1996.

[58] D. K. Serkland and P. Kumar, "Tunable fiber-optic parametric oscillator," *Optics Letters*, vol. 24, no. 2, p. 92, Jan. 1999.

[59] W. Ng, R. Stephens, D. Persechini, and K. V. Reddy, "Ultra-low jitter mode-locking of Er-fiber laser at 10 GHz and its application in photonic analog-to-digital conversion," in *International Topical Meeting on Microwave Photonics MWP 2000 (Cat. No.00EX430)*, Oxford, UK, pp. 251-254.

[60] H. A. Haus and A. Mecozzi, "Noise of mode-locked lasers," *IEEE Journal of Quantum Electronics*, vol. 29, no. 3, pp. 983-996, Mar. 1993.

[61] R. Paschotta, "Noise of mode-locked lasers (Part II): timing jitter and other fluctuations," *Applied Physics B*, vol. 79, no. 2, May 2004.

[62] A. Yariv, *Quantum electronics*, 3rd ed. New York: Wiley, 1989.

[63] P. Becker, *Erbium-doped fiber amplifiers : fundamentals and technology*. San Diego: Academic Press, 1999.

[64] D. Bertsekas, *Introduction to probability*, 2nd ed. Belmont Mass.: Athena Scientific, 2008.

[65] F. Rana et al., "Characterization of the noise and correlations in harmonically mode-locked lasers," *Journal of the Optical Society of America B*, vol. 19, no. 11, p. 2609, Nov. 2002.

[66] S. Namiki and H. A. Haus, "Noise of the stretched pulse fiber laser. I. Theory," *IEEE Journal of Quantum Electronics*, vol. 33, no. 5, pp. 649-659, May 1997.

[67] O. Prochnow et al., "Quantum-limited noise performance of a femtosecond all-fiber ytterbium laser," *Optics Express*, vol. 17, no. 18, p. 15525, Aug. 2009.

[68] M. E. Grein et al., "Observation of quantum-limited timing jitter in an active, harmonically mode-locked fiber laser," *Optics Letters*, vol. 27, no. 11, p. 957, Jun. 2002.

[69] T. Yilmaz, C. M. DePriest, P. J. Delfyett, Jr., A. Braun, and J. Abeles, "Measurement of residual phase noise and longitudinal-mode linewidth in a hybridly mode-locked external linear cavity semiconductor laser," *Optics Letters*, vol. 27, no. 10, p. 872, May 2002.

[70] J. Chen, J. W. Sickler, E. P. Ippen, and F. X. Kärtner, "High repetition rate, low jitter, low intensity noise, fundamentally mode-locked 167 fs soliton Er-fiber laser," *Optics Letters*, vol. 32, no. 11, p. 1566, 2007.

[71] A. Schlatter et al., "Nearly quantum-noise-limited timing jitter from miniature Er:Yb:glass lasers," *Optics Letters*, vol. 30, no. 12, p. 1536, 2005.

[72] J. B. Schlager, B. E. Callicoatt, R. P. Mirin, N. A. Sanford, D. J. Jones, and J. Ye, "Passively mode-locked glass waveguide laser with 14-fs timing jitter," *Optics Letters*, vol. 28, no. 23, p. 2411, Dec. 2003.

[73] Y.-F. Chen, J. Jiang, and D. J. Jones, "Remote distribution of a mode-locked pulse train with sub 40-as jitter," *Optics Express*, vol. 14, no. 25, p. 12134, 2006.

[74] H. A. Haus, K. Tamura, L. E. Nelson, and E. P. Ippen, "Stretched-pulse additive pulse mode-locking in fiber ring lasers: theory and experiment," *IEEE Journal of Quantum Electronics*, vol. 31, no. 3, pp. 591-598, Mar. 1995.

[75] C. X. Yu, S. Namiki, and H. A. Haus, "Noise of the stretched pulse fiber laser. II. Experiments," *IEEE Journal of Quantum Electronics*, vol. 33, no. 5, pp. 660-668, May 1997.

[76] R. Paschotta, "Timing jitter and phase noiseof mode-locked fiber lasers," *Optics Express*, vol. 18, no. 5, p. 5041, Feb. 2010.

[77] Y. Song, K. Jung, and J. Kim, "Impact of pulse dynamics on timing jitter in mode-locked fiber lasers," *Optics Letters*, vol. 36, no. 10, p. 1761, May 2011.

[78] H. Haus, *Electromagnetic Noise and Quantum Optical Measurements*. Berlin ;;London: Springer, 2011.

[79] S. J. Augst, T. Y. Fan, and A. Sanchez, "Coherent beam combining and phase noise measurements of ytterbium fiber amplifiers," *Optics Letters*, vol. 29, p. 474, 2004.

[80] U. Morgner et al., "Sub-two-cycle pulses from a Kerr-lens mode-locked Ti:sapphire laser," *Optics Letters*, vol. 24, p. 411, Mar. 1999.

[81] U. Morgner et al., "Nonlinear Optics with Phase-Controlled Pulses in the Sub-Two-Cycle Regime," *Physical Review Letters*, vol. 86, pp. 5462-5465, Jun. 2001.

[82] L.-J. Chen, "The Role of Plasma Formation in Mode-locking of Few-cycle Ti:sapphire Lasers: A Spatiotemporal Model," presented at the CLEO, Baltimore, MD, 2011.

[83] L.-J. Chen, M. Y. Sander, and F. X. Kärtner, "Kerr-lens mode locking with minimum nonlinearity using gain-matched output couplers," *Optics Letters*, vol. 35, no. 17, p. 2916, Aug. 2010.

[84] D. Yoshitomi, Y. Kobayashi, H. Takada, M. Kakehata, and K. Torizuka, "100-attosecond timing jitter between two-color mode-locked lasers by active-passive hybrid synchronization," *Optics Letters*, vol. 30, p. 1408, Jun. 2005.

[85] Y. Kobayashi, D. Yoshitomi, M. Kakehata, H. Takada, and K. Torizuka, "Long-term optical phase locking between femtosecond Ti:sapphire and Cr:forsterite lasers," *Optics Letters*, vol. 30, p. 2496, 2005.

[86] A. Bartels, N. R. Newbury, I. Thomann, L. Hollberg, and S. A. Diddams, "Broadband phase-coherent optical frequency synthesis with actively linked Ti:sapphire and Cr:forsterite femtosecond lasers," *Optics Letters*, vol. 29, p. 403, 2004.

[87] J. Reichert, "Measuring the frequency of light with mode-locked lasers," *Optics Communications*, vol. 172, no. 1-6, pp. 59-68, Dec. 1999.

[88] J. Kim, "High-precision optical and microwave signal synthesis and distribution," Massachusetts Institute of Technology, Cambridge, MA, 2007.

[89] F. X. Kärtner et al., "Ultrabroadband double-chirped mirror pairs for generation of octave spectra," *Journal of the Optical Society of America B*, vol. 18, no. 6, p. 882, 2001.

[90] L.-J. Chen, M. Y. Sander, and F. X. Kärtner, "Kerr-lens mode locking with minimum nonlinearity using gain-matched output couplers," *Optics Letters*, vol. 35, no. 17, p. 2916, Aug. 2010.

[91] K. Tamura, E. P. Ippen, H. A. Haus, and L. E. Nelson, "77-fs pulse generation from a stretched-pulse mode-locked all-fiber ring laser," *Optics Letters*, vol. 18, no. 13, p. 1080, Jul. 1993.

[92] R. Trebino and D. J. Kane, "Using phase retrieval to measure the intensity and phase of ultrashort pulses: frequency-resolved optical gating," *Journal of the Optical Society of America A*, vol. 10, no. 5, p. 1101, May 1993.

[93] R. Trebino, *Frequency-resolved optical gating : the measurement of ultrashort laser pulses*. Boston: Kluwer Academic, 2000.

[94] G. Chang, L.-J. Chen, and F. X. Kärtner, "Fiber-optic Cherenkov radiation in the few-cycle regime," *Optics Express*, vol. 19, p. 6635, Mar. 2011.

[95] B. Saleh, *Fundamentals of photonics*, 2nd ed. Hoboken N.J.: Wiley-Interscience, 2007.

[96] D. D. Hudson, K. W. Holman, R. J. Jones, S. T. Cundiff, J. Ye, and D. J. Jones, "Mode-locked fiber laser frequency-controlled with an intracavity electro-optic modulator," *Optics Letters*, vol. 30, no. 21, p. 2948, 2005.

[97] R. Jones and J.-C. Diels, "Stabilization of Femtosecond Lasers for Optical Frequency Metrology and Direct Optical to Radio Frequency Synthesis," *Physical Review Letters*, vol. 86, pp. 3288-3291, Apr. 2001.

[98] E. A. Donley, T. P. Heavner, F. Levi, M. O. Tataw, and S. R. Jefferts, "Double-pass acousto-optic modulator system," *Review of Scientific Instruments*, vol. 76, p. 063112, 2005.

[99] J. R. Birge, R. Ell, and F. X. Kärtner, "Two-dimensional spectral shearing interferometry for few-cycle pulse characterization," *Optics Letters*, vol. 31, no. 13, p. 2063, 2006.

[100] Hyunil Byun et al., "Integrated Low-Jitter 400-MHz Femtosecond Waveguide Laser," *IEEE Photonics Technology Letters*, vol. 21, pp. 763-765, Jun. 2009.

[101] P. Myslinski, D. Nguyen, and J. Chrostowski, "Effects of concentration on the performance of erbium-doped fiber amplifiers," *Journal of Lightwave Technology*, vol. 15, pp. 112-120, Jan. 1997.

[102] Sander, M., "10GHz Waveguide Interleaved Femtosecond Pulse Train," presented at the CLEO, Baltimore, MD, 2011.

[103] H. A. Haus, "Mode-locking of lasers," *IEEE Journal of Selected Topics in Quantum Electronics*, vol. 6, no. 6, pp. 1173-1185, Dec. 2000.

[104] F. X. Kaertner, "Ultrafast Optics," Spring-2008.

[105] J. S. Russell, "Report on waves," presented at the Report of the 14th meeting of the British Association for the Advancement of Science, 1884.

[106] A. Hasegawa, "Transmission of stationary nonlinear optical pulses in dispersive dielectric fibers. I. Anomalous dispersion," *Applied Physics Letters*, vol. 23, no. 3, p. 142, 1973.